Synthesis and characterisation of doped silicon nanoparticles by hot wire thermal catalytic and spark pyrolysis

A thesis presented for the degree of

DOCTOR OF PHILOSOPHY

in the Department of Physics

Faculty of Science

UNIVERSITY OF CAPE TOWN

Manfred Rudolf Scriba

February 2010

Supervised by:

Prof M. Härting and Prof D.T. Britton

ABSTRACT

Doped silicon nanoparticles with clean surfaces and which are suitable for electronic applications, have successfully been produced. The doped silicon nanoparticles produced in this work will find application in the emerging field of flexible electronics. Two bottom-up production processes were utilised: hot wire thermal catalytic pyrolysis and spark pyrolysis. The latter is a new process, developed as part of this research for silicon nanoparticle synthesis. In each method silicon nanoparticles were synthesised using mixtures of silane and phosphine or diborane, to achieve n and p-type doping respectively. Silicon nanopowders were also synthesised with silane only, to produce intrinsic particles for comparison. All particles produced at high pressure are predominantly monocrystalline and have average diameters between 20 and 40 nm. Particles are spherical when produced by spark pyrolysis and faceted when synthesised by hot wire thermal catalytic pyrolysis.

To determine doping activity in the silicon nanoparticles, the resistivity of the nanopowders was measured by a technique, and apparatus, developed as part of this work. Particles produced with diborane exhibit decreasing resistivity with increasing diborane concentrations, indicating successful doping. However the resistivity of particles produced with phosphine increases at higher phosphine concentration. While the surfaces of particles produced by either process are clean when produced with diborane, the surfaces of particles synthesised with phosphine are covered by an oxide layer whose thickness increases with higher phosphine concentrations. All nanoparticles produced by HWTCP at low pressure with either dopant gas were successfully doped, but had an average diameter of 10 nm.

ACKNOWLEDGEMENTS

From the start, as co-founder and first chair of the South African Nanotechnology Initiative (SANI), for 3 years, and throughout the completion of my MSc and PhD, many people have played a vital role in the development of my nanotechnology career. I would like to acknowledge:

My supervisors, Prof Margit Härting and Prof David Britton, University of Cape Town, for offering me this life changing opportunity as well as for their guidance, support and encouragement;

My wife Gisela for her understanding, patience and support;
My children Andrea and Christian for cheering me up;

Dr Hoffman Maree for putting me on this interesting career path;
Dr Neil Trollip for believing in the possibilities and project financial support;
Dr Suprakas Sinha Ray for his encouragement and for supporting the project;
CSIR for a fulfilling career and the opportunity to do this interesting work towards acquiring a PhD;

The Department of Science and Technology for their insight and support in developing and funding nanoscience and nanotechnology activities in South Africa;
My colleagues, at the DST/CSIR National Centre for Nano-Structured Materials for the many technical discussions and advice.

Furthermore, I thank my parents Fritz and Carmen for their love and support, and for the opportunity to grow up in the blessed family they created. Their encouragement and love, and that of my parents-in-law Prof Rolf and Waldtraut Oellermann, helped me a lot during the completion of my MSc and PhD.

CONTENTS

1. INTRODUCTION

Silicon can be considered the semiconductor with the most useful properties for the manufacture of electronic devices such as individual transistors, integrated circuits and solar cells. However, due to the nature of the devices and their manufacturing processes, applications are generally limited to rigid mounting without the option of flexibility. In the last two decades there has thus been a drive to develop new technologies that allow the production of flexible electronics. Recently, printed electronics, based on silicon nanoparticle inks [1], has emerged as a new route. The technology currently allows the printing of silicon based devices on flexible media such as paper and polymers [2]. In these applications the printed nanoparticle network must be able to act as an extrinsic semiconductor, thus requiring the silicon nanoparticles to be doped.

Historically research into silicon nanoparticles has focussed mainly on their luminescent [3-7] and optical properties for applications such as bio-markers [8], solid state lighting [9, 10], and sensors [8]. While an oxide layer on the silicon nanoparticles is essential for photoluminescence [10], it also acts as an insulator hindering the transfer of charge, which is vital for electronic applications. To date no silicon particles produced by bottom-up synthesis have been reported which have a clean unobstructed surface. However some successes have been reported for top-down milling of silicon nanoparticles [11]. As a consequence, for the production of silicon nanoparticles for electronic applications it is of utmost importance to utilize production processes that avoid oxidisation and allow the incorporation of dopant atoms in the silicon structure. The first requirement can be achieved by synthesis processes in the absence of air or other oxidising environments. Suitable bottom-up production processes include chemical vapour synthesis by laser or plasma pyrolysis [12-14] and laser ablation [15, 16] at very low base pressure (high vacuum). Recently, hot wire thermal catalytic pyrolysis (HWTCP) [17] has been added as a route to synthesize intrinsic silicon nanoparticles of varying degrees of crystallinity and size [18].

Even though silicon thin films have been produced by chemical vapour deposition with a mixture of silane and dopant gases such as diborane or phosphine [19-21], the same approach has not been successful in producing doped silicon nanoparticles for electronic applications. While boron is more likely than phosphorus to be incorporated in the silicon nanoparticles [12], the formation of a silicon oxide layer [7, 9, 10, 22, 23] on the particles inhibits conduction.

As will be shown in this work the fulfilment of both requirements, producing doped silicon nanoparticles with clean surfaces, presented a challenging task. This was achieved as follows. Due to its simplicity, HWTCP was selected as a means of bottom-up synthesis of the nanoparticles, using mono-silane as well as a mixture of mono-silane and phosphine or diborane as precursor gas to provide the silicon base material. Building on this, spark pyrolysis (SP) was conceived and developed in this thesis, as a new method for silicon nanoparticle synthesis. For this purpose a production system was constructed and used to synthesise sets of intrinsic and doped silicon nanoparticles using both methods. In both cases the effect of process parameters on particle quality and yield was thoroughly investigated. The particles produced were then characterised, using a suite of micro-structural, spectroscopic and electrical techniques to determine their suitability for electronic applications and to understand the influence of the synthesis conditions.

Starting in chapter 2, an overview of the properties of silicon as a semiconductor will show the importance of doping for the functioning of silicon devices. In chapter 3, the research will be put in context by looking at current nanoparticle production methods and their applicability to silicon nanoparticle production. A detailed discussion of chemical vapour synthesis processes will form the link to the HWTCP and SP processes. Chapter 4 is dedicated to the description of the production system and the production processes. After an overview of the characterisation techniques in chapter 5, the results of the micro-structural, spectroscopic and electrical characterisation will be presented in chapter 6, followed by a discussion in chapter 7 and concluding remarks in chapter 8.

2. SILICON AS A SEMICONDUCTOR

The dependence of electrical conduction on certain properties of silicon, including its crystal structure, band structure, Fermi level and doping concentration will be discussed in this chapter. The change of these properties due to the reduction in size, such as in silicon nanoparticles, as well as the effect of the surface properties, will also be considered.

2.1 Conductivity

Electrical conductivity σ is a measure of the ability of a material to conduct an electric current when placed in an electric field. It is defined as the ratio of the current density J to the applied electric field strength $\mathcal{E}$ given by Ohm's law

$$J = \sigma\mathcal{E} . \qquad (2.1)$$

The current density can also be described in terms of the number of charge carriers n, their drift velocity v and charge q [24] by

$$J = nvq , \qquad (2.2)$$

leading to an expression for the conductivity in terms of the carrier motion and applied field

$$\sigma = \frac{nvq}{\mathcal{E}} . \qquad (2.3)$$

The mobility μ is the quantity relating the drift velocity of the charge carriers to the applied field across the semiconductor according to

$$v = \mu\mathcal{E} . \qquad (2.4)$$

Furthermore, mobility is a function of the average relaxation time τ and the effective mass m^* of the charge carriers as

$$\mu = \frac{q\tau}{m^*}. \qquad (2.5)$$

Although normally treated as a scalar quantity, the effective mass is a tensor that describes the inertia of free charge carriers in a crystal, which behave like free particles with a mass depending upon their direction of travel in the crystal [25]. Defined by Newton's second law, the effective mass m^* can be calculated from the dispersion relation of the carrier energy

$$\left(\frac{1}{m^*}\right)_{ij} = \frac{1}{\hbar^2}\frac{d^2E}{dk_i dk_j}, \quad (2.6)$$

where E is the energy, h is Plank's constant and k is the wave number. The equation for the conductivity of a semiconductor (2.3) can thus be rewritten as:

$$\sigma = \frac{nq^2\tau}{m^*}. \qquad (2.7)$$

From equation 2.7 it is clear that the conductivity is mainly dependant upon the carrier density n, and the relaxation time τ.

2.2 Carrier density

In a semiconductor charge can be carried by an electron moving in the normally empty states of the conduction band or by holes moving in the normally filled states of the valence band. The hole can be seen as the absence of an electron or as a particle which is a positive charge carrier [26]. Electrons and holes will thus move in opposite directions during conduction. Furthermore the ability to conduct a charge is directly linked to the density of charge carriers, which in silicon is mainly

affected by its band structure, density of states and doping concentration. These aspects will now be discussed.

2.2.1 Silicon crystal structure

Silicon crystallises in the diamond structure with a face centred cubic (fcc) Bravais lattice and a lattice constant of 0.543 nm [27], as shown in the ball and stick model given in figure 2.1(a). The highlighted links indicate how each silicon atom is covalently bonded to its four nearest neighbours at an angle of 109.5° and a distance of 0.235 nm, to form a tetrahedron [28].

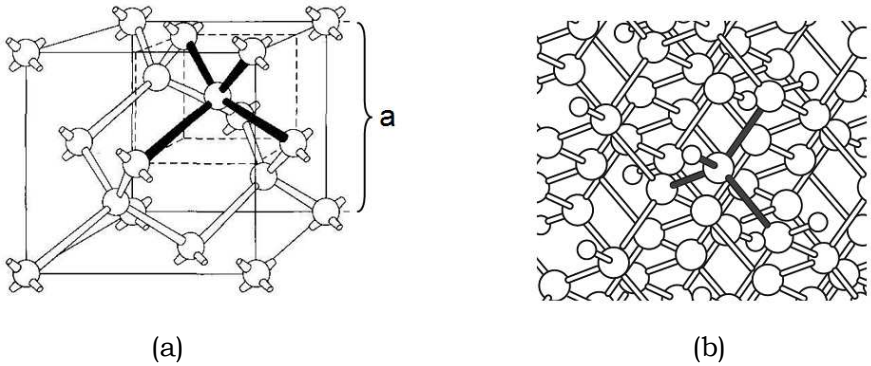

Figure 2.1 Ball and stick model of the structure of (a) crystalline [26] and (b) amorphous [29] silicon, with the tetrahedral bonds highlighted.

This tetrahedral arrangement is maintained within the disorder of the amorphous silicon structure shown in Figure 2.1(b), and also in atomic clusters and nanoparticles [30]. A consequence of the bonding is that the valence electrons are influenced by a number of adjacent ion cores and the sharply defined levels of the electron energies of the individual atoms become energy bands.

2.2.2 Band structure

Many physical, electrical and optical properties of solids can be explained using energy band theory [28, 31]. Energy bands originate from interactions between electrons in neighbouring atoms. In isolated atoms electrons exist in distinctive energy orbits, differentiated by orbital and intrinsic angular momentum. If atoms are now arranged in a solid, where they share electrons in bonds, the number of

levels is proportional to the number of atoms. This is in accordance with the Pauli exclusion principle which states that two electrons may not occupy the same state. Due to the extremely small differences in energy and momentum between the states, these from a quasi-continuous dispersion curve, called an energy band.

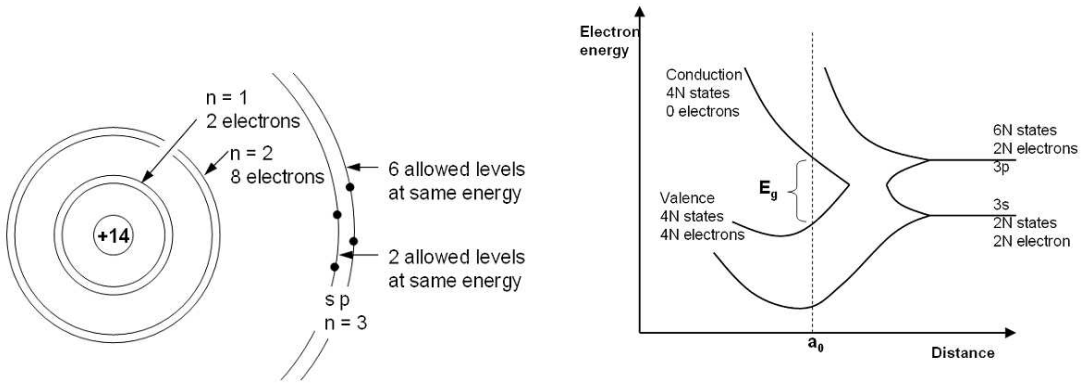

(a) (b)

Figure 2.2 A graphical presentation of (a) the electron orbits in a silicon atom and (b) the sp^3 hybridisation, to form a band structure in the silicon crystal (redrawn after [26]).

As can be seen in figure 2.2(a), in the free silicon atom, the four valence electrons occupy the 3s and 3p orbitals. In the crystal these orbits hybridise to form a band structure with 4N electrons in the valence band and none in the conduction band, at absolute zero. This state is shown in figure 2.2(b) by the vertical line marked a_0. The band gap E_g, which is 1.12 eV for silicon, is also indicated in the diagram.

In order for a semiconductor to conduct a current, charge carriers must be able to move into an empty quantum state in the same band. Thus, materials with full valence and empty conduction bands do not conduct. However a semiconductor which has a partially filled conduction band, or holes in the valence band will conduct an electric charge. This is shown in the simplified band structures of figure 2.3, for an (a) insulator, (b) semiconductor and (c) conductor.

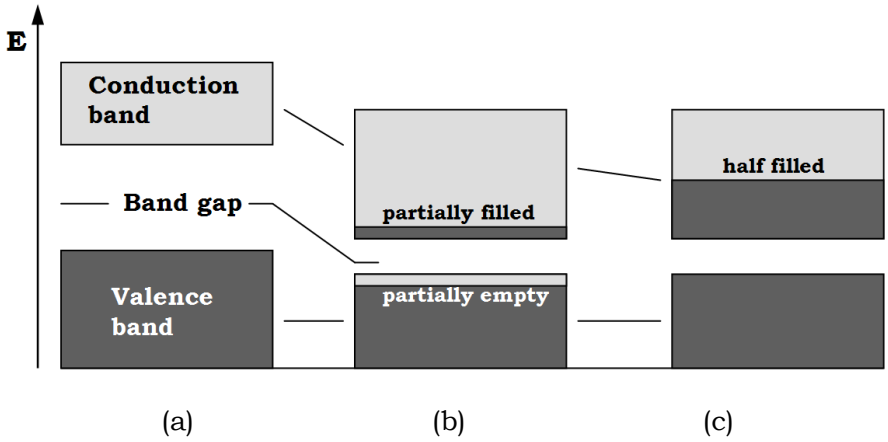

Figure 2.3 Possible energy band diagrams of an (a) insulator, (b) semiconductor and (c) conductor. (modified after [32])

For an insulator (figure 2.3 (a)) the valence and conduction bands are separated by a wide band gap. Electrons do not have enough energy to leave the filled valence band to reach and partially fill the conduction band. In an un-doped (intrinsic) semiconductor (figure 2.3 (b)) the band gap is narrow. At room temperature electrons at the top of the valence band can be excited into the conduction band. The partially filled bands can now facilitate conduction. In metals the conduction band is half filled as shown in figure 2.3 (c), making them conductors even at low temperatures.

From this simplified discussion the importance of the availability of charge carriers is emphasised. The number or concentration of charge carriers in a particular energy band is dependant upon the density of states available in the energy band as well as the probability of finding the charge carriers in that energy band.

2.2.3 Carrier density

The statistical distribution of the energy of charge carriers in thermal equilibrium at an absolute temperature T may be described by the Fermi-Dirac distribution function,

$$f_F(E) = \frac{1}{1 + e^{[(E-E_F)/k_B T]}} \ , \qquad (2.8)$$

where E is the carrier energy, E_F is the Fermi energy and k_B is the Boltzmann constant. The Fermi distribution $f_F(E)$, shown in figure 2.4 will change with temperature and is important in determining the electrical and thermal properties of a semiconductor.

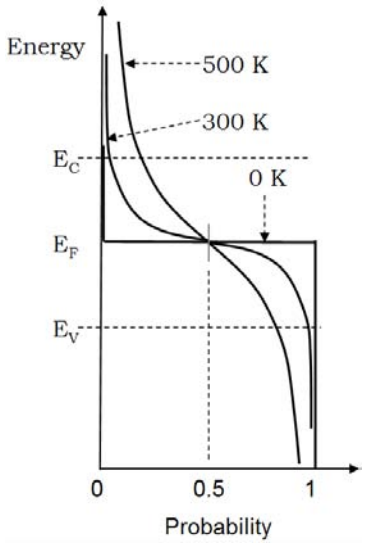

Figure 2.4 The Fermi-Dirac distribution, superimposed on a schematic band structure showing the position of the conduction band (E_C), valence band (E_V) and Fermi level (E_F). (redrawn after [25])

As can be seen from the step function in figure 2.4, in the ground state corresponding to absolute zero of temperature, levels with lower energy than the Fermi level E_F are fully occupied with electrons, whereas higher energy levels are unoccupied. At absolute zero an intrinsic semiconductor is thus an insulator. In an intrinsic semiconductor, E_F is at mid-gap [27], halfway between the valence and conduction band edges E_V and E_C. As the temperature increases (300 – 500 K), the step function smoothes out and the distribution extends into the conduction band and valence band. The probability of an electron state being occupied in the conduction band, and being empty in the valence band therefore increases, thus increasing the conductivity of the intrinsic semiconductor. However to determine how many charge carriers can be found in these bands it is important to determine the density of states.

2.2.4 Density of states

The density of states of a semiconductor refers to the number of available energy or quantum states in the valence and conduction bands per unit volume that can be occupied by charge carriers. To a first approximation the density of states of the conduction band N_C is given by [25]

$$N_C(E) = \frac{4\pi(2m_n)^{3/2}}{h^2}(E - E_C)^{1/2} \quad , \qquad (2.9)$$

where m_n is the effective electron mass with energy E, and h is Plank's constant. Similarly the density of states for holes in the valence band can be calculated using the effective mass of the hole and the energy below the valence band edge.

2.1.4 Doping

In intrinsic semiconductors, at finite temperatures, a small number of electrons are thermally excited from the valence band into the conduction band, leaving behind an equal number of holes. As illustrated in the band diagrams of figure 2.5 the number of charge carriers in a band is a function of the density of states as well as the probability $f_F(E)$ of finding carriers in that band. In the intrinsic semiconductor (figure 2.5 (a)) the number of holes p in the valence band equals the number of the electrons n in the conduction band and each equals the number of intrinsic carriers n_i. Furthermore the intrinsic carrier concentration relates to the density of states in the conduction band N_C as well as the energy of the Fermi level E_F and conduction band edge E_C by [33]

$$n_i = N_C \exp\left[\frac{E_F - E_C}{kT}\right]. \qquad (2.10)$$

It will now be shown that the addition of impurities into the semiconductor, also known as doping, introduces free charge carriers into the semiconductor, which greatly increase its conductivity at room temperature. Doping makes the semiconductor extrinsic. Boron and phosphorus are often used to dope silicon by diffusion into the solid or by the incorporation of dopant gases in the production

process. Boron which has one electron less than silicon in its valence shell will leave an excess hole when substituting silicon atoms in the structure. Boron is said to be an acceptor (of electrons) and the resulting extrinsic semiconductor is p-type with holes as the majority carriers. Similarly, phosphorus with five valence electrons is a donor of an electron. Phosphorus doped material is n-type and therefore has electrons as majority carriers. Doping causes the Fermi level E_F to shift from the intrinsic Fermi level E_i towards the energy band that corresponds to the majority carriers as shown in figure 2.5. Under thermal equilibrium conditions the law of mass action, described by the equation $np = n_i^2$ is valid for both intrinsic and extrinsic semiconductors.

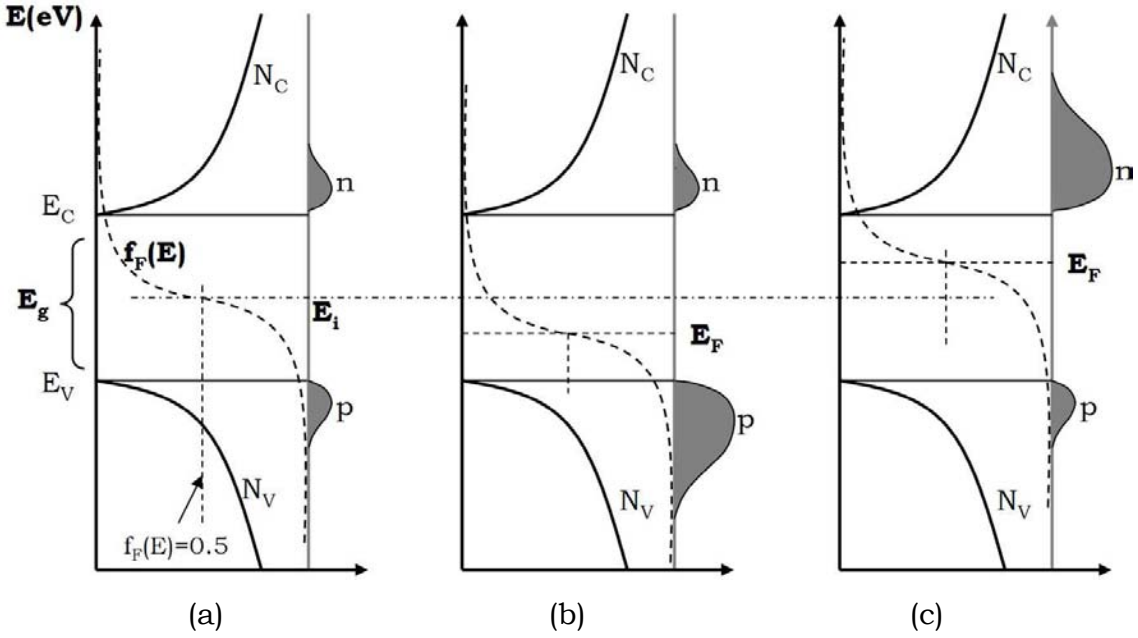

Figure 2.5 Band diagram with overlaid density of states, Fermi distribution and carrier concentration of (a) intrinsic, (b) p-doped, and (c) n-doped silicon. (modified after [26, 34]).

In figure 2.5 (b) the shift of E_F towards the top of the valence band E_V, due to the introduction of the donor atoms is clear. The Fermi energy E_F, can be obtained in terms of the intrinsic carrier densities and the concentration of acceptors N_A [25, 33]

$$E_F - E_V = kT \ln\left(\frac{n_i}{N_A}\right), \qquad (2.11)$$

under the assumption that $N_A \approx n$, the free electron concentration. The higher the acceptor concentration the smaller the energy difference (E_F - E_V) and the closer the Fermi level moves to the top of the valence band, increasing the hole concentration. As indicated by the grey areas in figure 2.5 (b), in a p-doped semiconductor the positive charge carriers p in the valence band outnumber the electrons n in the conduction band, making this semiconductor p-type. The hole concentration in the valence band is

$$p = n_i \exp\left[\frac{E_i - E_F}{kT}\right], \qquad (2.12)$$

where E_i is the Fermi level of the intrinsic semiconductor. Similarly the band diagram of an n-doped semiconductor (figure 2.5 (c)) shows how E_F shifts to the bottom of the conduction band when donor atoms N_D are introduced into the semiconductor. E_F can be obtained in terms of the donor concentration N_D [25, 33]

$$E_C - E_F = kT \ln\left(\frac{n_i}{N_D}\right). \qquad (2.13)$$

The effect is that the electron concentration n, in the conduction band outnumbers the hole concentration p, in the valence band, as indicated by the grey areas in figure 2.5 (c). The electron concentration in this n-type semiconductor is

$$n = n_i \exp\left[\frac{E_F - E_i}{kT}\right]. \qquad (2.14)$$

In both n-doped and p-doped materials the availability of additional charge carriers in the conduction and valence bands respectively increases the conductivity of the semiconductor.

2.3 Properties of silicon nanoparticles

Because the focus of this thesis is the production of silicon nanoparticles which can be used in electronic applications, it is important to look at differences in properties between bulk silicon and silicon nanoparticles. The discussion here will mainly focus on electrical properties and will be limited to effects of increased surface to volume ratio and to quantum confinement if the particle is small enough.

The properties of a nanoparticle are dominated by its surface [35]. The surface can be defined as the outermost two to three atomic layers which may be reconstructed. In a reconstructed surface, dangling bonds of neighbouring atoms combine, resulting in a rearrangement of the atoms at the surface [28]. The dangling bonds may also be terminated by adsorbates such as hydrogen [36] or organic molecules such as methoxy or butyl groups [4] thus passivating the surface against further chemical reaction. If nanoparticles are however produced in oxidising conditions, insulating oxide layers may form [7, 9, 10, 22]. The conductivity of the nanoparticles will now be reduced in relation to the layer thickness of this oxide, as discussed later in this thesis.

In bulk crystalline silicon the electronic structure provides a band-gap with the lowest point of the conduction band and the highest point of the valence band occurring at different coordinates in reciprocal space [37]. Due to this indirect band gap, bulk silicon requires the involvement of a momentum balancing phonon for the emission of a photon. As these transitions have a low probability [15] bulk silicon has relatively poor optical emission properties [13]. However, the situation changes if silicon is nanostructured, as was first observed in the photoluminescence of porous silicon at room temperature [38]. As shown in figure 2.6, bulk crystalline silicon has near continuous conduction and valence energy bands, separated by a characteristic energy gap E_g.

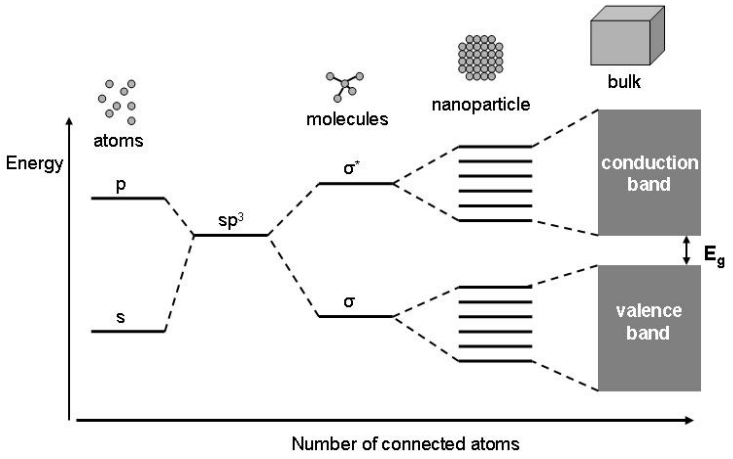

Figure 2.6 Complete sp^3 hybridisation cycle including the quantised states present in nanoparticles (modified after [39]).

In silicon nanoparticles smaller than about 10 nm, the continuum of energy levels in the bands becomes discrete, effectively increasing the band gap. The band gap of the silicon nanoparticles is thus size dependent [3, 6, 37, 40] and can be altered to produce a range of energies. The excited electron/hole pairs (excitons) are confined in all three dimensions, resulting in properties between those of a bulk semiconductor and single molecules. The formation of localised excitonic states is also known as quantum confinement and these small nanoparticles are often called quantum dots.

The estimated band gap of a spherical nanoparticle E_N is inversely proportional to the square of its radius R [41], by

$$E_N \approx E_g + \frac{\hbar^2 \pi^2}{2 m_q R^2}, \qquad (2.15)$$

where E_g is the band gap of the bulk material and m_q is the reduced mass which is the product of the effective mass of the electrons m_e and holes m_h divided by their sum. From equation 2.15, quantum confinement effects in silicon nanoparticles become significant when R is smaller than approximately 10 nm [41, 42]. As the particle diameter or crystallite size decreases, the band gap increases, resulting in a blue shift in the luminescent spectrum [43]. Furthermore, it has been observed that

the oxide shell plays a vital part in the optical properties of silicon nanoparticles [7] including photoluminescence [6]. Photoluminescence is not observed when the silicon nanoparticles do not have an oxide shell [44] and its intensity increases with oxidisation of the particles [10, 43]. It has also been shown that photoluminescence is weakened with the growth of silicon nanoparticle clusters, the clusters are responsible for the de-confinement of the excited carriers and thus for the quenching of the photoluminescence. Efficient photoluminescence and efficient charge transport are thus mutually exclusive [45]. These findings and a further observation that photoluminescence occurs in particles larger than 10 nm [46, 47] where quantum confinement is not a factor, implies that the surface layer plays a vital role in visible light emission of silicon nanoparticles. Oxidisation also leads to the passivation of dangling bonds that otherwise may lead to non-radiative recombination centres [48] and reduced photoluminescence [13]. Furthermore, the excitons localized at the Si/SiO_2 interface in oxidized nanoparticles [49, 50] cause broad photoluminescence spectrum in the visible region [51]. Since the electronic states at the surface thus dominate the luminescence, the relative amounts of oxygen and hydrogen impurities on the surface have a large influence [52].

3. CHEMICAL VAPOUR SYNTHESIS

As the silicon nanoparticles produced in this research are intended for application in printed electronic devices, the production process must deliver non-oxidised particles of high purity. Hot wire thermal catalytic pyrolysis (HWTCP) and spark pyrolysis (SP), developed as part of this work, are the two chemical vapour synthesis processes that were used for the production of doped silicon nanoparticles. To place chemical vapour synthesis in context, this chapter will start with a general overview of nanoparticle synthesis processes which are based on top-down and bottom-up approaches.

3.1 Overview of top-down silicon nanoparticle production

Of the top-down processes for nanoparticle production, mechanical attrition is the simplest. It requires relatively inexpensive equipment, is easy to scale up and is applicable to many hard materials. Furthermore, mechanical attrition has extensively been used to produce silicon nanoparticles in the 10 to 100 nm size range [11, 53, 54]. However, the challenge to achieve mono-dispersion and prevent contamination remains. Alternative top-down methods which offer better process control include laser ablation [5, 15], spark ablation [55] and sputtering [56]. In all of these processes particles are formed by the evaporation of material and the subsequent homogeneous nucleation from the supersaturated vapour. The process may be operated in the presence of a reactive gas such as hydrogen or quenching gasses including argon and helium. In laser ablation, a short burst of laser energy heats and evaporates a small volume of material [16]. Using this process, silicon nanoparticles in the 5-60 nm size range have been produced in small quantities [57-59]. Silicon nanoparticles can also be produced by a high-current arc between two sacrificial silicon electrodes [15] which vaporises them [15, 23]. In sputtering [47], an inert gas is ionised by a high voltage potential, resulting in the ions being accelerated towards a precursor target to release the material on impact. This technique has been used to produce silicon nanopowders in hydrogen-rich plasma

[60]. Finally, silicon nanoparticles may also be produced by electrochemical processes. A silicon wafer is inserted into a hydrogen fluoride solution in the presence of an external current originating from a platinum cathode. Highly uniform silicon nanoparticles, in the 1 to 5 nm range [61], as well as porous silicon, can be produced by this electrochemical etching of the bulk silicon [49, 62]. The advantage of this process is that particles can be produced with a narrow size distribution [37, 63] and, furthermore, the process allows the nanoparticle surfaces to be capped with active molecules.

3.2 Chemical vapour reactions

All production techniques based on chemical vapour reactions are bottom-up processes. These processes are characterised by energy induced chemical reactions in the gas phase, which, depending on conditions like pressure, temperature, the abundance of precursor and the substrate temperature, either lead to gas phase nucleation of particles or the deposition of thin films on cooler substrates [64]. Chemical vapour deposition (CVD) is for instance extensively used for the deposition of microcrystalline [19, 65], polycrystalline [66-68] and amorphous [65, 69] thin films of silicon [67, 70], synthetic diamond, carbon, silicon carbide, silicon nitride and a number of polymers [71, 72]. When the CVD process is used for the production of nanoparticles and nanostructures it is referred to as chemical vapour synthesis (CVS) or pyrolysis. While pyrolysis refers to the cracking of molecules into radicals such as atoms and complex ions, synthesis describes the building of larger units such as particles from these atoms and radicals. CVS is useful for the bottom-up production of nanoparticles, nanowires [73] and nanotubes [74] of various elemental compositions including silicon. The CVS processes suitable for silicon nanoparticle production are usually defined by the energy source that initiates the chemical reaction in the vapour phase such as: furnace, laser, and plasma and flame pyrolysis. Under favourable pressure and temperature conditions, the gas-phase decomposition of the reactants in all these processes will lead to supersaturation, homogeneous nucleation and nanoparticle formation. Each of these processes will be discussed briefly.

Furnace pyrolysis

A furnace reactor is characterised by a high temperature zone, normally produced inside a quartz tube under vacuum, into which the precursor is introduced [75]. The vapour dissociates in the high temperature region, and particles form by subsequent cooling through rapid expansion or by the introduction of an inert cooling gas. Nanoparticles are usually collected down stream from the high temperature zone, before they can enter the vacuum pump.

Laser pyrolysis

In laser pyrolysis the precursor is pyrolysed in a reaction chamber, by an infrared (CO_2) laser beam. The laser may be pulsed to produce rapid localized heating and rapid cooling of the gas. Due to its versatility and controllability, laser pyrolysis has been used extensively for the production of silicon nanoparticles from silane [15, 16, 48, 50, 76, 77]. The process allows good control of the composition, shape and size distribution of the particles [78] and dependant upon the process parameters is suitable for the production of silicon crystallites of high purity with a diameter between 2 and 60 nm [7, 79]. Amorphous silicon nanoparticles with a similar size distribution have also been produced [80].

Plasma pyrolysis

This process is based on the dissociation of precursor molecules by the plasma, which is created in a reaction chamber by microwaves or radio frequency (RF) energy. Gas phase reactions of the precursor and intermediates, are activated by energetic electrons in the plasma, leading to particle formation at elevated pressures [74]. Plasma pyrolysis is suitable for the production of crystalline silicon nanoparticles from silane gas [81] with a particle size range between 2 to 200 nm [22, 82, 83] depending upon the process parameters. As plasma synthesis is relatively simple and scalable [83] it is used to produce nanopowders of many different materials on an industrial scale [84], including SiO_2 nanopowder [85].

Flame pyrolysis

In flame pyrolysis, the precursor, which may be a powder, liquid or vapour, is mixed with a combustible carrier which is injected into the flame. Due to the high energy density in the flame, the precursor is pyrolysed by temperatures as high as 2400 °C. The coupling of the particle production to the flame chemistry, makes flame pyrolysis a complex process that is difficult to control [15] and usually leads to agglomerated and oxidised particles [15]. While flame pyrolysis is extensively used for the production of oxide particles with diameters ranging from 10 to 100 nm [86], it is not generally useful for the synthesis of elemental nanoparticles.

Basic chemical reaction process

A graphical representation of the basic chemical reaction processes leading to the chemical vapour deposition of thin films and the chemical vapour synthesis of nanoparticles is shown in figure 3.1. For silicon film synthesis, the precursor gas is most often mono-silane with the possible addition of dopant gases such as diborane or phosphine, as well as carrier gases including He, H_2 [87, 88], Ar and N_2 [83].

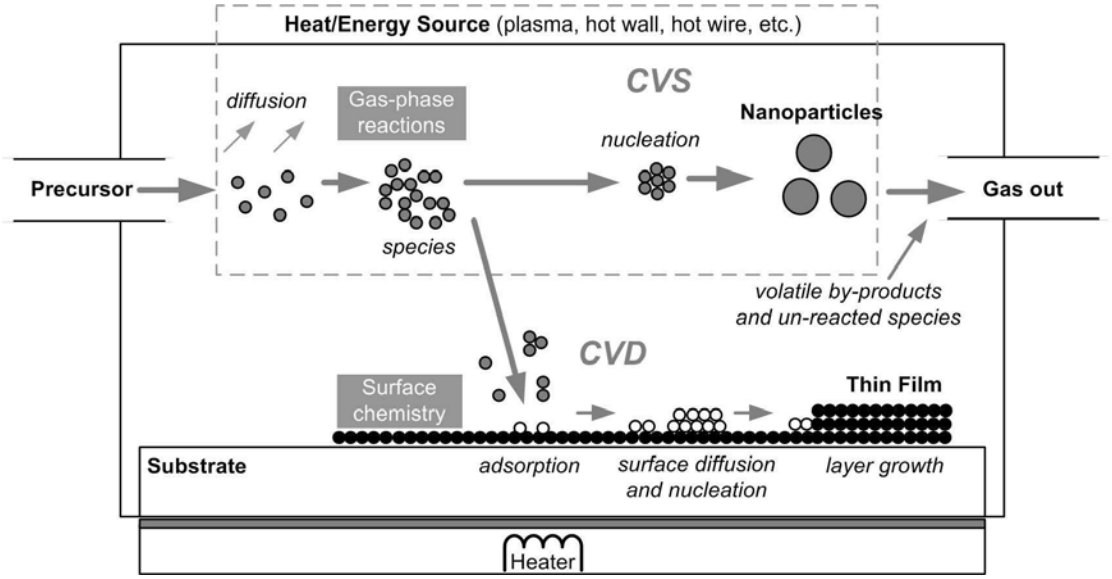

Figure 3.1 Graphic representation of the basic chemical reaction processes and physical steps in CVD of thin films and CVS of nanoparticles. (modified after [89, 90])

Starting on the left of the diagram in figure 3.1; upon injection of the precursor gas or vapour into the reactor, homogeneous gas phase reactions take place, initiated by a heat source. These chemical reactions include bond breaking or dissociation of the precursor molecules, to produce reactive intermediates including atomic ions and complex radicals which are the species for particle and film growth. Furthermore, as shown in figure 3.1, depending on the conditions in the reactor such as pressure, temperature and precursor concentration the process will either favour layer growth or powder formation. When the vapour pressure exceeds the condensation pressure, at the prevailing temperature, the process is in supersaturation. Gas phase reactions of species now lead to homogeneous nucleation and coagulation in the vapour phase, resulting mainly in powder synthesis [15]. In contrast, the film growth process is operated at much lower pressures. Species are adsorbed on the substrate surface, which is often hot, resulting primarily in layer growth by surface diffusion and nucleation. Volatile by-products such as hydrogen, as well as un-reacted species produced by the processes, are removed by the exhaust system.

The nucleation and particle growth may further be linked to the probability of collisions between particles of the species in the reactor, which depends on their mean free path. The Knudsen equation gives the molecular flux per unit area J for a stable gas or vapour [91]

$$J = \frac{N_A P}{\sqrt{2\pi MRT}}, \qquad (3.1)$$

where N_A is Avogadro's number, M is the molar mass of the gas, R is the ideal gas constant and T is the temperature. From equation 3.1 it is clear that higher pressures and lower temperatures will increase the probability of collision and thus growth rate of particles in the vapour [90]. However these conditions may also lead to agglomeration and coagulation [22, 85] which can be avoided by rigorous control of nucleation-condensation conditions such as diffusion and turbulence, as well as by the effective collection of nanoparticles [84]. Furthermore, the size, shape and crystallinity of the particle are mainly dependant on the synthesis pressure, the time spent in the high temperature zone and the cool down profile. In general an increase in synthesis time and pressure will result in larger particles [46, 83, 92].

Inert quenching gases may, however, be used to limit particle growth [15] and aggregation [15]. While the exact mechanism under which amorphous or crystalline particles will form is still not fully understood [93], higher power density [22] as well as higher temperature and pressure generally lead to crystalline nanoparticles [13, 22, 83] whereas lower pressures results in amorphous particles [22, 85, 94-96].

Doping

In gas phase reactions the dopant is simply included in the precursor gas mix during synthesis [97]. For instance diborane (B_2H_6) and phosphine (PH_3) have been used as dopant gases, mixed with silane (SiH_4) [98], for the chemical vapour deposition of silicon thin films [19-21] and in one case the synthesis of silicon nano-crystallites using plasma enhanced chemical vapour deposition [12]. During the deposition process the dopant and precursor gases are both dissociated and take part in the production of the films, to be incorporated in the silicon structures. In general an increase in dopant concentration in the synthesised silicon structure is expected with an increase in dopant gas concentration [99].

3.3 Silicon nanoparticle production by hot wire thermal catalytic pyrolysis

The hot wire thermal catalytic pyrolysis (HWTCP) process is based on the well known hot wire chemical vapour deposition (HWCVD) process, operated at higher pressures, where gas phase nucleation dominates. From its beginning in 1979 [100] and through extensive study and development of the technique [101-105], HWCVD is now suitable for large scale deposition of protective Teflon coatings [72], thin film transistors [106] and high-efficiency solar cells based on amorphous and microcrystalline silicon [68]. For silicon films the precursor is most often mono-silane which may be diluted by H_2 [21] or He [67]. Due to the catalytic decomposition reaction of the silane on the filament, composed of tungsten, tantalum or molybdenum [107, 108], the hot wire is very efficient at dissociating the silane molecules, producing a large flux of radicals, which are the growth species responsible for the high rate of layer growth [109]. The type and abundance of species will depend on the pressure, filament temperature and precursor composition as shown by some of the chemical reactions on the filament [110]:

$$SiH_4 \rightarrow Si + 4H$$
$$SiH_4 \rightarrow SiH_2 + H_2$$
$$2SiH_4 \rightarrow 2SiH_3 + H_2.$$

Further reactions in the gas phase typically include [101, 108, 110, 111]:

$$H + SiH_4 \rightarrow SiH_3 + H_2$$
$$H + SiH_3 \rightarrow SiH_2 + H_2$$
$$SiH_3 + SiH_3 \rightarrow SiH_4 + SiH_2$$
$$Si + SiH_4 \rightarrow Si_2H_2 + H_2$$
$$Si_2H_2 + SiH_2 \rightarrow Si_3H_2 + H_2$$

Through both, experimental studies and numerical modelling, more than 30 vapour phase reactions and at least 10 surface reactions have been suggested [110-112]. The properties of materials produced will mainly be affected by temperature gradients in the reaction chamber caused by differences in flow due to geometry [67], filament temperature [113] hydrogen concentration [114] [115] and substrate temperature [116]. Furthermore, in hot wire reactors the decomposition rate of silane depends upon the process pressure, which determines the mean free path of radicals and temperature of the catalytic filament which, above 1700°C, decomposes almost all of the silane [70].

3.4 Spark pyrolysis as a new route to silicon nanoparticle production

For the first time, as part of this research, spark pyrolysis (SP) of silane was investigated for the production of silicon nanoparticles. Although electrically excited, the process has most similarities with pulsed laser pyrolysis [79], which has short heating and rapid cooling cycles [85]. While the synthesis of silicon nanoparticles by the spark pyrolysis of silane is novel, similar techniques have been used to research the possibility that organic compounds were formed by lightning in the atmosphere of the young earth [117, 118]. Other reports of spark research focus on the processes in the internal combustion engine [119] and the ignition of combustible gases and vapours as part of industrial safety experiments [120].

The spark can be defined as a sudden breakdown or ionisation of an insulating gas or vapour, due to a high electric field between two electrodes. Free electrons and to a lesser extent ions, form the current of charge carriers in the plasma of the spark [55] resulting in a near instantaneous heat source [121]. The spark plasma may reach temperatures between 5000 °C [122] and 22000 °C [123] in a few micro seconds. This high temperature heat source is expected to rapidly dissociate the silane and dopant gases during the production of doped silicon nanoparticles by SP. The shock wave formed by the rapidly expanding plasma channel may also play a role in the particle formation [55]. Spark discharges, however, generally contain complex plasmas with an ill-defined temperature profile [124].

In the next chapter the synthesis system and experimental procedures, leading to silicon nanopowder production will be discussed.

4. SYNTHESIS OF SILICON NANOPARTICLES

Taking into account the general considerations of the previous chapter, a basic hot wire thermal catalytic pyrolysis (HWTCP) synthesis system was designed and constructed. In the course of developing and testing this system a new method for the production of silicon nanoparticles was devised. This emerging synthesis technique was called spark pyrolysis (SP). The system was thus modified to accommodate both HWTCP and SP. In this chapter, the two production methods as well as the general characteristics of the system will be discussed. Emphasis is also given to the description of the experimental procedures and the silicon nanopowder samples produced.

4.1 Principle and overview of the combined hot wire thermal catalytic and spark pyrolysis system

Starting at a high level, the synthesis system consists of four main functional units; the gas supply and control, the reaction chamber, the vacuum system (pumps) and the instrumentation. The basic synthesis system is shown in figure 4.1, with details of its components given in the caption. Starting with the gas supply system, all gases pass through mass flow controllers which supply them in a measured quantity to the reaction chamber where synthesis takes place. Vacuum pumps connected to the reaction chamber remove gaseous by-products to the exhaust processing unit. All controllers, meters and power supplies form part of the instrumentation. A complete system diagram is shown in Appendix A.

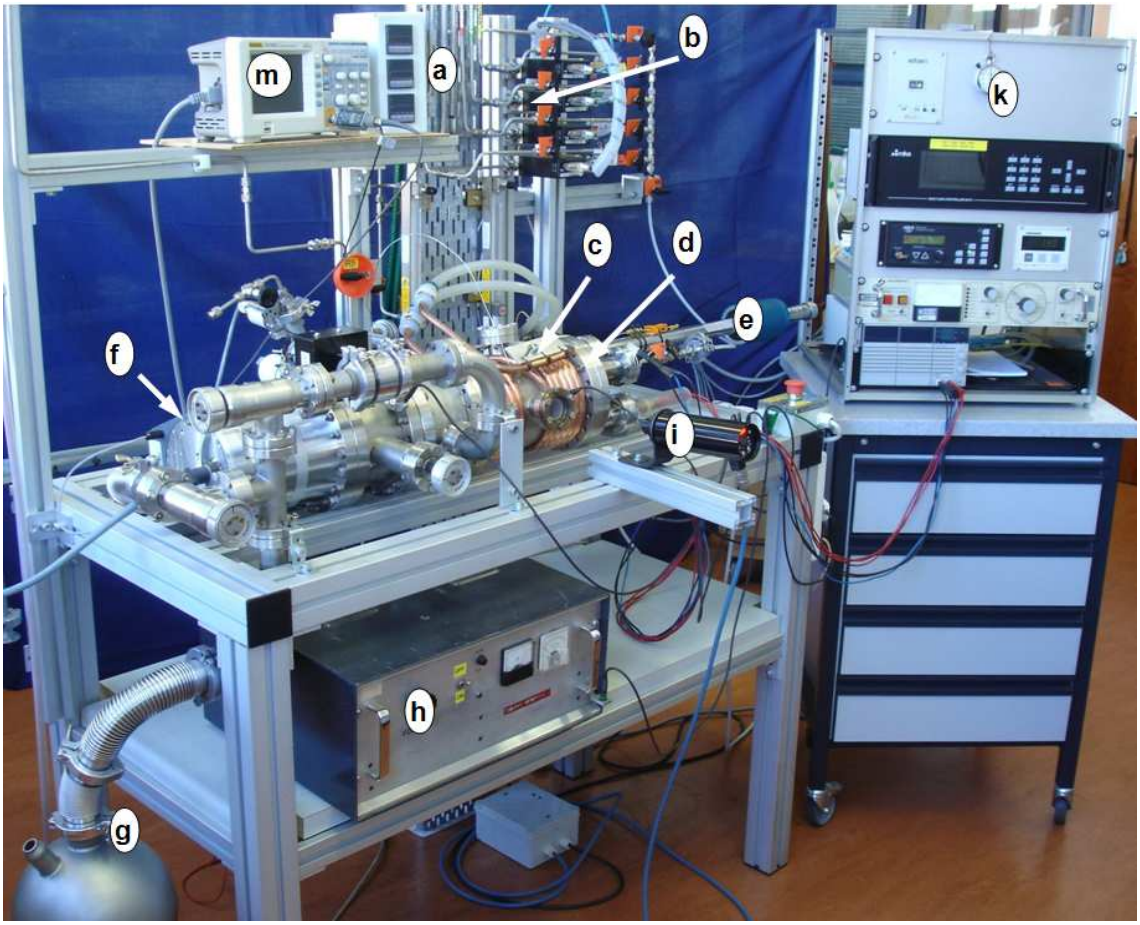

Figure 4.1 The nanoparticle synthesis system comprising (a) gas supply lines, (b) mass flow controllers, (c) reaction chamber, (d) supply flange, (e) magnetic feed-through rod (f) turbo pump, (g) cold trap on top of rotary pump, (h) high voltage power supply, (i) pyrometer, (k) instrumentation and (m) oscilloscope and thermocouple readout.

In general the chamber requires only minor changes to the internal configuration when alternating between HWTCP and SP as discussed below. Furthermore, the spark gap, production pressure, filament temperature and gas flow rates can be varied and maintained. The major sections of the system, including relevant instruments, will now be discussed in detail.

4.1.1 Gas supply

Three precursor gases were used in the production of doped silicon nanoparticles; silane (SiH_4), a mixture of 15% diborane (B_2H_6) in silane and a mixture of 15 %

phosphine (PH_3) in silane, all with a purity of ≥99.99% (H_2 < 50 ppm, N_2 ≤ 1 ppm, O_2 ≤ 1 ppm and H_2O ≤ 1 ppm). As these gases are pyrophoric, the 10 litre cylinders, containing 2 kg of gas, were housed in fire proof Düpperthal G90 cabinets. To flush the system, nitrogen with a purity of ≥99,8 % (H_2O ≤ 40 ppm and O_2 ≤ 100 ppm) was supplied to the laboratory from a gas bank outside the building. All gases are supplied through stainless steel tubing (figure 4.1(a)) to the mass flow controllers (figure 4.1(b)) and the reaction chamber (figure 4.1(c)) through safety shut-off valves. The mass flow controllers determine the ratio of each precursor gas supplied to the reaction chamber. A MKS 6476 unit was used to control two MKS 1779A mass flow controllers with a 0-10 sccm range for the diborane and phosphine, and a MKS 2179A with 0-100 sccm range for the silane.

4.1.2 Reaction chamber

The reaction chamber which has a volume of 6.58 litres can easily be removed for powder collection and consists of a 270 mm long stainless steel cylinder with a 250 mm inside diameter and a CF200 flange on each end. One of these flanges connects to the Adixen ATH 300 turbo pump and Edwards E2M8 two stage rotary pump. The other chamber opening is closed by the supply flange containing the gas supply and electrical feedthrough (figure 4.1(d)). A type K (chromel–alumel) thermocouple is mounted on a movable rod on the inside of the chamber, to allow the monitoring of temperature profiles, linearly through the chamber. Another type K thermocouple measures the temperature of the outside of the chamber wall which is cooled by a 12.5 mm diameter copper tube which is wound around the chamber and supplied with about 2 l/min of room temperature tap water. Quartz windows on the side of the chamber cylinder allow line of sight temperature measurements of the filament by a pyrometer, mounted outside the chamber. The pressure inside the reaction chamber is controlled by a MKS600/MKS722A controller and pressure gauge combination which adjusts a MKS 253B-20-40-1 motorised butterfly valve mounted at the exhaust output of the camber. An Alcatel ACS 1009 pressure gauge and ACS 1000 controller supply a constant readout of the pressure inside the chamber. The output of the rotary pump is vented to the scrubber.

4.1.3 Deposition system for hot wire thermal catalytic pyrolysis

The schematic in figure 4.2(a) shows the chamber configuration for HWTCP and figure 4.2(b) is an image of the inside of the supply flange. A low voltage high current power supply heats the HWTCP filament (1) through two insulated mounting rods (2). The filament is the heated catalyst for the pyrolysis of the precursor gases.

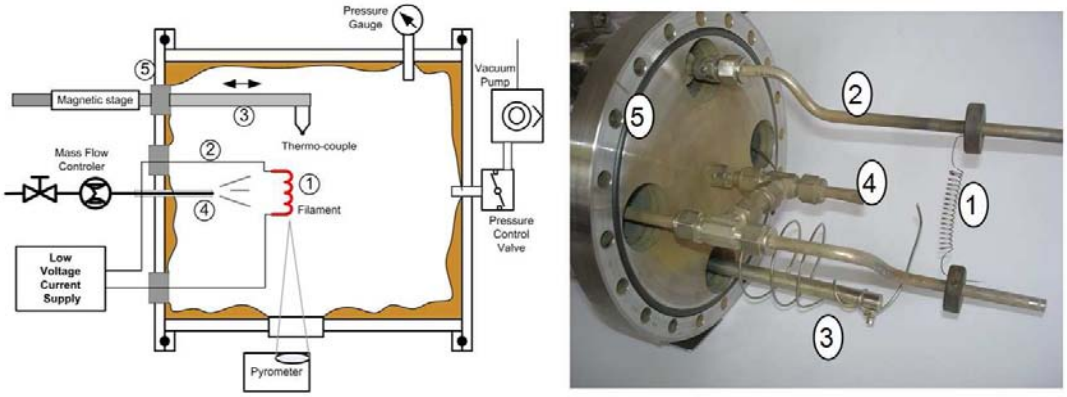

(a) (b)

Figure 4.2 (a) Schematic of the HWTCP configuration and (b) image of the main flange of the reactor.

Continuing with figure 4.2, a thermocouple mounted on a rod (3), can be moved linearly towards the filament, using the magnetic stage. It was used to measure the temperature of the inside of the chamber. The gas supply nozzle (4) and all other supplies to the reactor are fed though ports on the supply flange (5). The filament (1) consists of a 0.5 mm diameter tungsten wire coiled with an inside diameter of 6 mm and about 14 turns. The temperature of the filament is measured through a quartz window by a Raytek MR1S two colour IR pyrometer and controlled manually, by adjusting the Texico PS36-30 power supply with a maximum rating of 36 V and 30 A.

4.1.4 Deposition system for spark pyrolysis

As shown in figure 4.3 (a) and (b), the spark pyrolysis system uses the same vacuum configuration as the HWTCP system, with only a few changes to the internal components on the supply flange. The Dynamco 30kV high voltage power

supply connects to the tungsten spark filament (1) with adequate Teflon insulation (2) at the feed-through ports on the supply flange (3). The spark gap was formed by mounting two 0.5 mm diameter tungsten wires in the same mounts as the hot filament, such that the gap is roughly aligned with the gas supply nozzle.

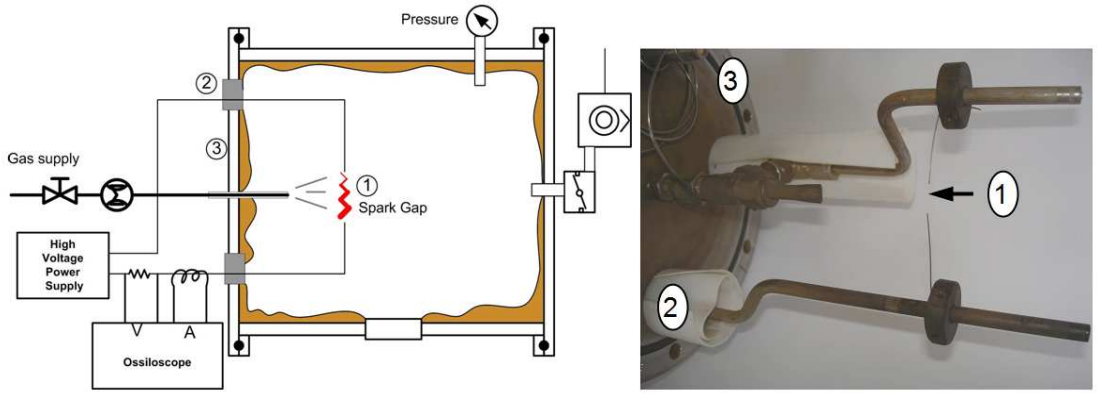

Figure 4.3 (a) SP configuration and (b) image of main flange supporting the conduction rods and spark electrodes.

The spark characteristics were measured with a current and voltage probe connected to the current line, as shown in figure 4.3(a), and recorded by a Rigol DS1302CA digital oscilloscope with a bandwidth of 300MHz and sample rate of $2x10^9$ per second. The high voltage power supply is shown in the simplified schematic in figure 4.4, and consists of a charging transformer with rectifier and a 100 nF output capacitor C. The inductance L originates from all wires inside and outside of the power supply.

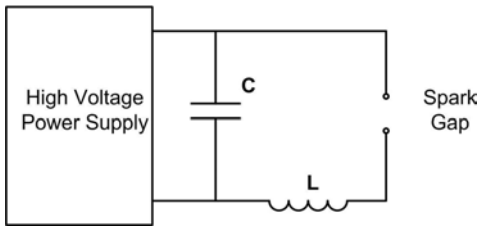

Figure 4.4 Simplified high voltage LC circuit of the spark gap and power supply.

4.2 Vacuum quality

Impurities in the vacuum system will mostly affect the nanoparticle composition and surface properties. These impurities can be attributed to virtual and real leaks as well as residual gases such as air and water vapour. The best base pressure achievable will depend on the leak rate, the pumping speed and the pumping duration [90]. Leaks were investigated by using the residual gas analyser (RGA) as a helium detector and introducing helium to the outside of flanges and joints. In general the lowest pressure achieved after 3 hours pumping was in the order of 1.0 x 10^{-7} mbar with the turbo pump and 5.0 x 10^{-3} mbar using the rotary pump. Two techniques are available to estimate the amount of residual gas in the system, or entering through leaks. The first, using the RGA and the second by measuring the pressure increase in a closed system. Both were tested on the system as part of the preparation for the synthesis of batch *HW10(P533)* with a production pressure of 10 mbar and pure silane only.

As a first test of vacuum quality, an Annevac 2 RGA was used to measure the residual gas of the system at a total pressure of 1.5 x 10^{-6} mbar. The analogue signals were recorded on a digital oscilloscope and plotted as shown in figure 4.5. The molecules and corresponding atomic mass unit of the four most intense peaks in the RGA spectra of figure 4.5 are presumed to arise from O (16), OH (17) and H_2O (18) and N_2 (28). Peaks corresponding to species heavier than 40 atomic mass units are often assigned to hydrocarbons [125] which may originate from oil vapours that back-stream from the roughing pump.

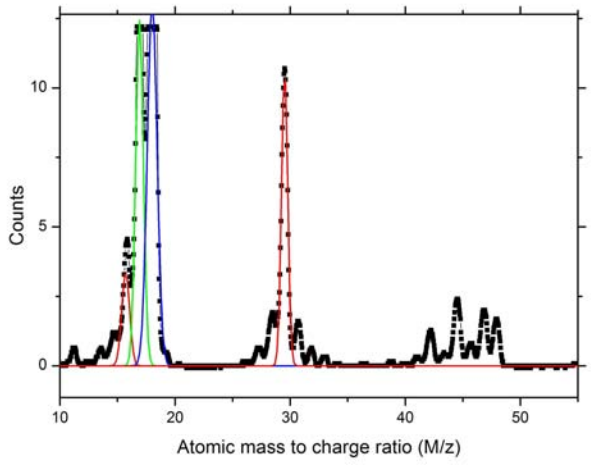

Figure 4.5 Atomic mass plotted against concentration of an evacuated chamber.

As an approximation it is assumed that the residual gas is made up of only these four species. The oxygen partial pressure in the reactor can now be calculated using the areas of the Gaussian fits of these four peaks. It is the product of the total pressure and the ratio of the sum of the oxygen containing peak intensities to that of the sum of all peak intensities [125] :

$$P_O = P_{Total}\left(\frac{A_{O(16)} + 0.5A_{OH(17)} + 0.33A_{H_2O(18)}}{A_{N(14)} + A_{O(16)} + A_{OH(17)} + A_{H_2O(18)} + A_{N_2(28)}}\right) , \qquad (4.1)$$

so that P_0, is estimated as $0.388P_{Total}$. The molar quantity of the oxygen in the residual gas can now be calculated using the Boltzmann equation:

$$n = \frac{P_0 V}{RT} , \qquad (4.2)$$

where P_0 is the oxygen partial pressure, V the volume, T the temperature and R is 8.314J/mol.K. The result is n = 1.55x10^{-10} mol. This quantity is clearly orders of magnitude lower than the typical 2.8 x 10^{-2} mol of elemental silicon produced in 8 minutes during a production run.

In a second approach the leak rate can be determined by measuring the rise in pressure of a closed system, in a fixed period of time [90]. After achieving a pressure in the order of 10^{-6} mbar, the isolation valve was closed and the rise in pressure over a time period recorded. The gas load of all leaks in the system G_L, is given by the equation:

$$G_L = \frac{n}{t} , \qquad (4.3)$$

where n is the number of moles, and t is the time period in which they leak into the system. In batch *HW10 (P533)*, on which the RGA test was performed at 24°C, the pressures increased from 1.4 x 10^{-5} mbar to 1.2 x 10^{-3} mbar in 24 seconds. The value of G_L can be calculated by rewriting equation 4.3 as

$$G_L = \frac{(P_{high} - P_{low})V}{RTt} . \qquad (4.4)$$

The resulting gas load is 1.4×10^{-8} mol.sec^{-1}. Assuming that the leak continues at the same rate during synthesis, the total molar contribution of leaks over the 8 min synthesis period is only 6.7×10^{-6} mol. As it is not possible to differentiate between the components in G_L it is assumed that all of it is oxygen. The percentage of oxygen in the nanoparticles attributable to the leak can thus be calculated as:

$$O_{np} = \frac{n_{OL}.100\%}{n_{OL} + n_{Si}} \quad , \qquad (4.5)$$

where n_{OL} and n_{Si} are moles of oxygen atoms in the leak gas and silicon atoms in the nanoparticles respectively. Using the quantity of silicon produced as 395 mg, the oxygen concentration should be 0.024%. Due to its simplicity and applicability to continuous production, the above method was used to determine the state of the vacuum before each synthesis run.

4.3 Filament characteristics in the hot wire thermal catalytic pyrolysis system

The temperature profile of the gas surrounding the 1800°C wire, during synthesis conditions of 40 mbar and a silane flow rate of 50 sccm, was determined using a thermocouple, mounted on a linear movable rod as shown in figure 4.2 marker (3). The temperature profile shown in figure 4.6 was recorded as a function of distance from the filament.

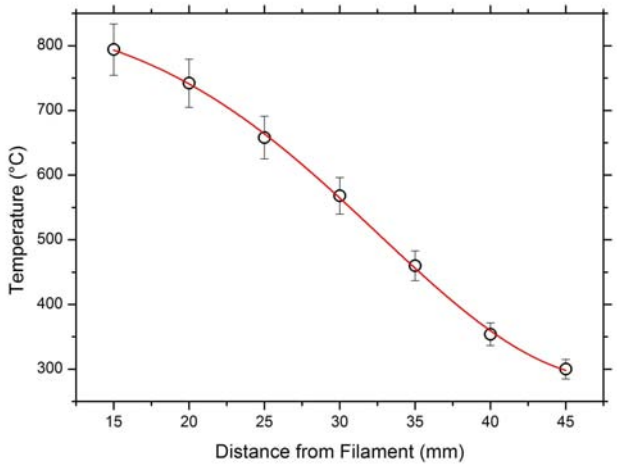

Figure 4.6 Temperature profile of volume around the filament, inside the chamber.

As expected the data of figure 4.6 shows a gradual decrease in temperature with an increasing distance from the filament. This rate of temperature decrease is expected to have an effect on the cooling rate and thus the characteristics of nanoparticles formed.

Another important aspect of hot wire chemical vapour synthesis is the condition of the filament. Compared to HWCVD, the HWTCP process operates at a much higher pressure. The effect is a visible deterioration of the filament over short operating times, as shown in figure 4.7, starting with cracking, deposits near the mounts and eventual breaking. Similar results have been reported in literature [126].

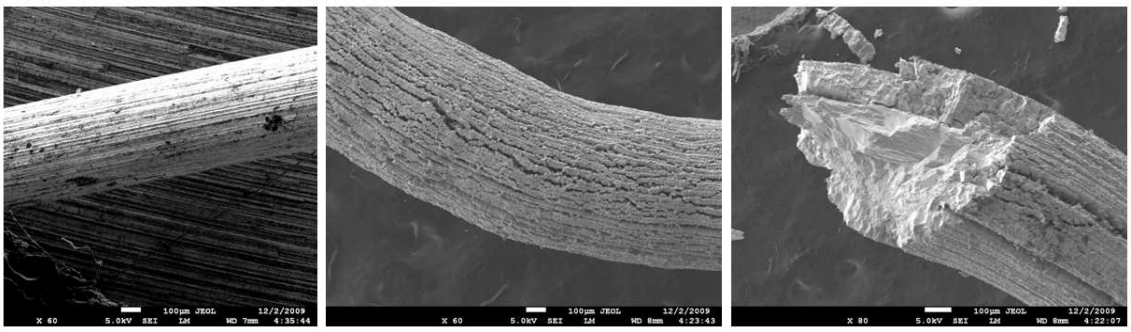

(a) (b) (c)

Figure 4.7 SEM micrographs at 80x magnification, of a typical tungsten filament (a) before synthesis and (b) after 8 min operation at 1800 °C in 5 mbar mono-silane. (c) Section of a broken filament.

The ageing of the filament is accompanied by an increase in the diameter, as illustrated by directly comparing the filament before synthesis (figure 4.7 (a)) to that after synthesis (b). In figure 4.7 (c), the deterioration and cracking of the outer layer of the filament is clearly visible. These images were taken on a JEOL JSM7500F analytical Field Emission SEM at a beam energy of 5 keV at 80x magnification. The filament ageing is partly attributable to the reaction of silicon which deposits on the filament and the tungsten of the filament itself [106]. It results in the formation of a tungsten silicide alloy [67, 127]. Studies on the lifetime improvement of filaments suggest filament temperatures higher than 1700°C for HWCVD [128, 129]. The filament in this research was thus maintained at 1800°C for all production runs.

4.4 Characteristics of the spark pyrolysis system

For the first time, a spark was used as the energy source for the pyrolysis of silane to produce silicon nanoparticles. The breakdown voltage in a gas, depends on the width of the spark gap and the pressure [55, 124]. To characterise the spark, the relationship between the gas pressure and breakdown voltage as well as the spark energy was determined. The breakdown voltage was measured over an 11 mm spark gap between 0.5 mm diameter tungsten wires, by filling the reactor with silane to a pressure of 150 mbar and then decreasing the pressure in 10 mbar steps by opening the valve to the roughing pump. At each pressure, starting from a low value, the voltage over the spark gap was increased until breakdown occurred. This breakdown voltage V_b, captured by a Fluke 73 voltage meter with a Fluke 80k-40 high voltage probe, and the pressure P_b, are plotted as a Paschen curve in figure 4.8.

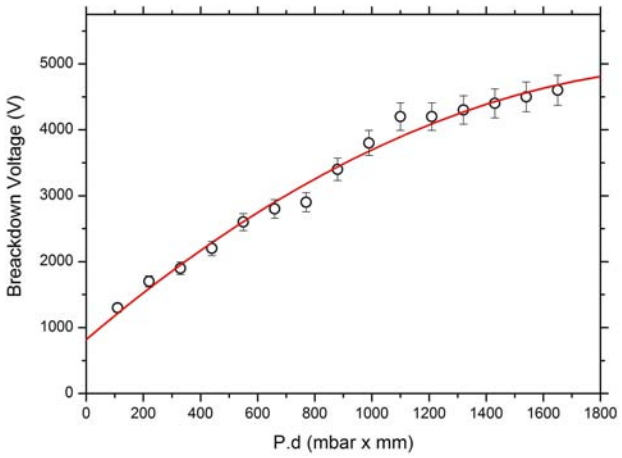

Figure 4.8 Paschen curve for silane, with a fixed spark gap of 11 mm.

A polynomial fit on the data of figure 4.8 gives a useful equation for the approximation of the breakdown voltage V_b for a specific spark gap in silane:

$$V_b = -8.26(P_b.d_b)^2 + 3.70(P_b.d_b) + 820.22 \ , \qquad (4.6)$$

where the pressure P_b and spark distance d_b is known. Generally at pressures below 20 mbar, glow discharge and accelerated growth of structures on the electrodes was observed.

Two methods were used to approximate the energy of the spark: firstly, by simply calculating the energy stored in the discharge capacitor of the high voltage power supply [122], and secondly by measuring the current and voltage characteristics of the spark [130]. A Rigol DS1302CA oscilloscope with a sampling rate of 2×10^9 s^{-1} and a bandwidth of 300MHz, was used for the spark discharge measurements. To minimise inductance effects the capacitor was directly connected to the spark gap with short leads. As is common in high voltage measurements [131], a 1:10000 resistive voltage divider was used with a 100:1 oscilloscope probe. As shown in figure 4.9, the spark circuit was left in free running mode, where the discharge capacitor is repeatedly charged until the breakdown voltage is reached. The average frequency and breakdown voltage, as shown in figure 4.9, is 9.5 Hz and 4602 V respectively.

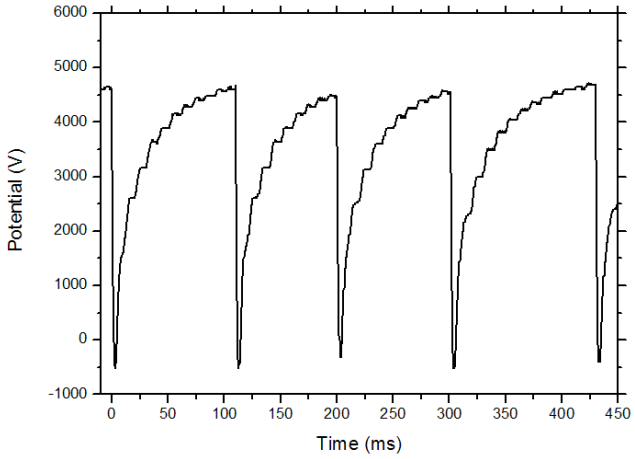

Figure 4.9 Free running, high voltage capacitor charge, breakdown and discharge cycle for a 12 mm spark gap in 160 mbar of silane.

In the first approximation the spark energy is assumed to be equal to the energy stored in the capacitor C of the high voltage power supply at the breakdown voltage V_b [122]. It may be calculated using the equation,

$$E = \frac{1}{2} C V_b^2 . \qquad (4.7)$$

Using equation 4.6, derived from the Paschen curve, the breakdown voltage for an 11 mm spark in 80 mbar of silane is 3.5 kV. Given that the capacitor of the high voltage power supply is 100 nF, the average energy of the spark is estimated to be

0.61 J. In the second approximation, the energy was calculated by measuring the change in current and voltage of the spark over the time. In figure 4.10 the current and voltage characteristics of a 12 mm spark in 80 mbar silane is presented.

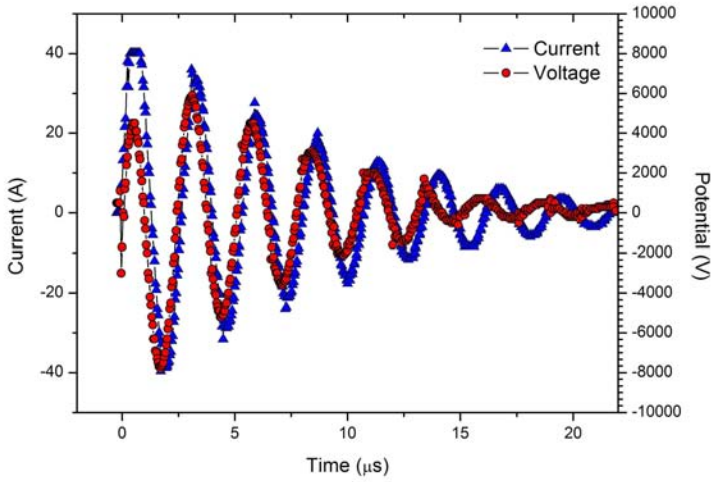

Figure 4.10 Current and voltage plot of a 12 mm spark in 80 mbar silane.

The oscillation or ringing in both current and voltage, visible in Figure 4.10, can be explained by stray inductance in the power supply and wires leading to the spark gap combined with the storage capacitor [55, 123]. The product of the current and voltage of the spark, or power, is shown in figure 4.11.

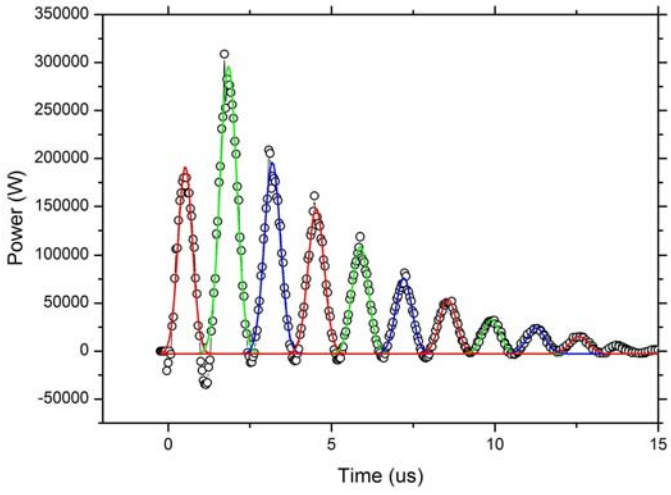

Figure 4.11 Plot of Power *(VI)* vs. time of the spark discharge.

The duration of the current flow in the spark plasma can be derived from figure 4.11. It is in the order of 100 ns. The spark energy can be approximated by the integral of the power over time, i.e. the area under the graph. As shown in figure 4.11, this was achieved by fitting Gauss curves to the first 10 peaks and adding the areas. Using the method above, and taking into consideration that losses due to radiation and power dissipation in the circuitry have not been considered, the approximate upper limit of the energy of this spark is 0.72 J.

A challenge in using a spark for silane pyrolysis is the control of the build-up of silicon on the spark electrodes, which may reduce the spark distance and affect the spark characteristics. As shown in figure 4.12 the tips of the tungsten spark electrodes which start as clean cut wires (inset), change shape during silicon nanoparticle production of 18 min, presumably due to the build-up of sputtered tungsten as well as deposited silicon. During the discharge, electrons will flow from the cathode figure 4.12 (right) to the anode (left). Furthermore, due to a change in conductivity of the deposit, the current may originate and strike at different locations on the spark electrodes.

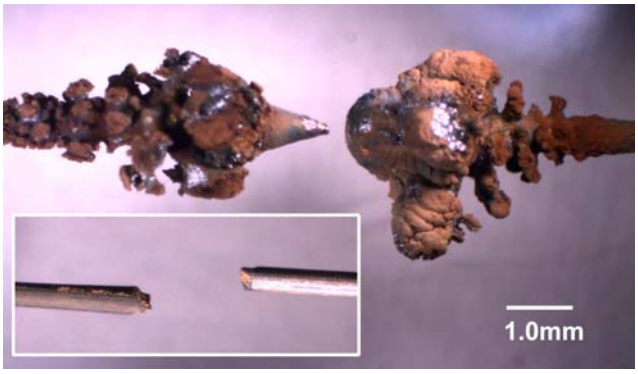

Figure 4.12 Spark electrodes at start of production (inset) and after 18 min of production (main image) at 80 mbar and 0.1 % diborane. (The distance between electrodes has been reduced for the image and the scale bar applies to both images)

4.5 Silicon nanoparticle production

The HWTCP/SP system was used within a predetermined parameter set presented in table 4.1 to systematically produce silicon nanoparticles. These parameters were generally based on the overview in chapter 3 as well as the experience gained in testing the system.

Parameter	**HWTCP**	**SP**
Pressure	5 to 40 mbar	40 to 400 mbar
Flow rate	25, 50 sccm	25, 50 sccm
Filament temp.	1800 °C	-
Spark energy	-	0.1-5 J
Gas doping ratio	1:100, 1:1000, 1:10000	1:100, 1:1000, 1:10000

Table 4.1 Parameter set for the production of silicon nanoparticles

The generic production procedure from the preparation of the system to the harvesting of powders is captured in the flow diagram presented in figure 4.13 below. The only difference between the two methods of production (light grey shapes), is the choice of which filament is mounted in the chamber, the power supply connected, and the production parameters in the “Start/Control” and “Record” steps.

Considering the self explanatory flow diagram in figure 4.13, only a few aspects in the production process will be discussed further. In the system preparation, the best base pressure, lower than 10^{-5} mbar, achievable after about 1 hour of pumping with a turbomolecular pump, was taken as sufficient. The outgas rate was now measured as described earlier in section 4.2. The reactor was filled with the precursor gases, to the desired control pressure. Before commencement of production the turbo pump was isolated and the roughing pump connected directly into the exhaust stream. Only then was the filament heated or spark started. During production the pressure and flow rates were automatically maintained, however, the filament temperature was controlled by constantly monitoring the pyrometer and manually adjusting the filament current.

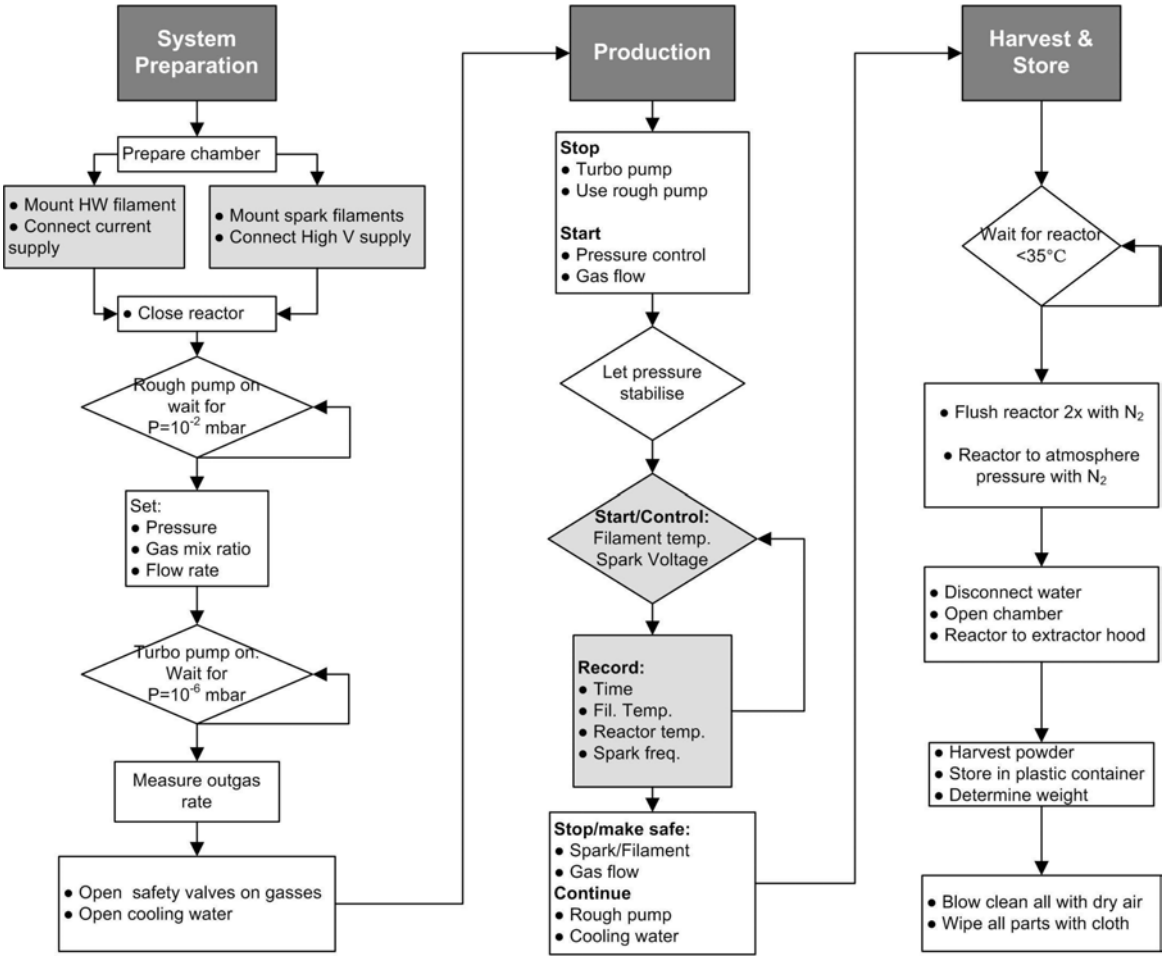

Figure 4.13 Flow diagram of the generic production procedure from the preparation of the system (top left) to the production and harvesting of powders.

During spark synthesis the high voltage power supply was set to a voltage sufficiently higher than the break-down potential, and left in free running mode. All powders where collected by first filling the chamber with nitrogen gas to atmospheric pressure and then opening the chamber to atmosphere. The powder was now scraped off the sides of the chamber with a plastic spatula. This harvested powder was then stored as a single batch in a plastic container. All parts were cleaned by blowing with high pressure dry air and by wiping with laboratory cleaning cloth. To prevent possible contamination, no organic solvents were used in the cleaning process. For safety reasons, and to prevent possible contamination, the system was kept under vacuum, when not used. Likewise, all unused gas supply lines were flushed with nitrogen and kept at 4 bar of nitrogen pressure.

The parameters and sample number of each production run for intrinsic powders is listed in table 4.2 and those for doped powders in table 4.3.

Synthesis Process	**Pressure (mbar)**	**Flow rate (sccm)**	**Silane**
HW TCP	5	50	*HW5 (P531)*
HW TCP	10	50	*HW10 (P533)*
HW TCP	20	50	*HW20 (P534)*
HW TCP	40	50	*HW40 (P535)*
SP	80	50	*SP80 (P731)*
Pyrophoric	670	200	*Silicon Oxide (P200)*

Table 4.2 List of batch numbers and production conditions of intrinsic powders.

As evident in the last columns of table 4.3, doping was achieved by adding phosphine and diborane to the precursor gas. The nominal doping concentrations are defined as the percentage of dopant gas to the total precursor gas. The actual concentration of dopant atoms in the particles produced may not necessarily be the same as this nominal doping concentration.

				Dopant gas ratio Φ_{dopant} / (Φ_{dopant}+ Φ_{silane})		
Process	**Dopant gas**	**P (mbar)**	**Φ (sccm)**	**1:10 000 (0.01%)**	**1:1 000 (0.1%)**	**1:100 (1%)**
HW TCP	Diborane	40	50	*HW40B0.01 (P881)*	*HW40B0.1 (P882)*	*HW40B1 (P883)*
HW TCP	Diborane	5	50	*HW5B0.01 (P891)*	*HW5B0.1 (P892)*	*HW5B1 (P893)*
HW TCP	Phosphine	40	25	*HW40P0.01 (P840)*	*HW40P0.1 (P810)*	*HW40P1 (P830)*
HW TCP	Phosphine	5	25	*HW5P0.01 (P851)*	*HW5P0.1 (P852)*	*HW5P1 (P854)*
SP	Diborane	80	50	*SP80B0.01 (P871)*	*SP80B0.1 (P872)*	*SP80B1 (P873)*
SP	Phosphine	80	25	*SP80P0.01 (P861)*	*SP80P0.1 (P862)*	*SP80P1 (P863)*

Table 4.3 List of batch numbers and production conditions of doped powders. All HWTCP runs lasted for about 12 min while those for SP lasted for about 18 min.

4.6 Powders produced

After the completion of each production run as listed in table 4.2 and 4.3, all the inside surfaces of the reaction chamber were covered with an easy to collect, low density layer of powder. It was observed that powder produced by SP (figure 4.14(a)) is generally more uniform in colour and thickness than powder produced by HWTCP (figure 4.14 (b)) where, for some production runs, different regions marked X, Y and Z in figure 4.14 (b), differed in colour. The colour pattern partially corresponds to the location of the filament and current supply rods in the chamber.

(a) (b)

Figure 4.14 Images revealing the inside of the reaction chamber, in the direction of the vacuum pump, after the production of intrinsic silicon nanoparticles by (a) SP at 80 mbar and (b) HWTCP at 20 mbar.

Due to the lack of distinct boundaries between areas containing different coloured powder (figure 4.14 (b), their selective collection was not attempted. All powders were collected as a single production batch, to be characterised as an average representation of that production run.

A further general observation in HWTCP is the change in colour of the powder depending upon the pressure during synthesis. While SP powders, which were produced at 80 mbar and higher, are always light ochre in colour, HWTCP powders gradually change from wine red at 5 mbar to a light ochre colour at 40 mbar. This colour change is shown in the images of powder deposited on the catchment plate at the vacuum pump exit in figure 4.15.

(a) (b) (c) (d)

Figure 4.15 Intrinsic nanopowder produced by HWCVD, depicting the colour change from (a) wine red produced at 5mbar, to (b) brown at 10 mbar, (c) light brown at 20 mbar and (d) ochre at 40 mbar.

For each production run, all powder in the chamber was collected and weighed as one sample. The yield was calculated as

$$Y = \frac{(n_{fill} + n_{synth})}{n_{powder}} \quad , \qquad (4.8)$$

where n_{fill} and n_{synth} are the molar amounts of precursor gas used to fill the chamber and injected into the process during production, respectively and n_{powder} is the molar amount of silicon in the powder collected, assuming it is pure silicon. Typically the SP process delivered 300-500 mg of powder in 18 minutes of production, while HWTCP produced 500-800 mg in 12 minutes. Taking into consideration a loss of 5-10% during harvesting the yield of SP is between 20 and 40% at 80 mbar and that of HWTCP between 60 and 80% at 40 mbar. The results indicate that HWTCP is generally twice as effective as SP in converting the silane to silicon nanoparticles. This trend can be expected, given the continuous heat source of the filament compared to the cyclical and short lived spark energy source.

In the next chapter the properties of the silicon nanopowders and nanoparticles will be investigated and discussed.

5. CHARACTERISATION TECHNIQUES

In this chapter the apparatus and techniques used for the characterisation of the nano-powders will be discussed. Included are structural, compositional, spectroscopic and electrical techniques.

5.1 Structural characterisation

5.1.1 Transmission electron microscopy

A JEOL 2100 transmission electron microscopy (TEM) with a 200kV acceleration voltage and LaB_6 filament was used in bright field mode, to determine the agglomeration, size, shape and crystallinity of the nanoparticles [7, 85]. The microscope has a point resolution of 0.2 nm and is equipped with a Gatan US1000, 2048 x 2048 pixel CCD camera.

Nanoparticles were prepared for TEM analysis by adding small quantities of powder to about 5 ml of methanol [96, 132] and facilitating the dispersion of the silicon nanoparticles with a 25 Watt probe sonicator for 5 seconds. A glass pipette was used to collect small amounts of this colloidal liquid from the centre of the dispersant volume. One drop of the solution was released onto the centre of an Agar Scientific 300 µm holey carbon film coated copper grid located on filter paper. The deposited solution was allowed to dry in air.

To determine the agglomeration, size and shape of the silicon nanoparticles the TEM was operated in the 20000x to 30000x magnification range. To enhance the contrast of the particles for easier and more accurate size determination, images were slightly under-focussed, resulting in a white line around the perimeter of the particles in the image. TEM images were taken of different clusters, which were chosen at random, from different positions on the TEM grids. Particle size was determined by measuring the Feret diameter, defined as the diameter of the

smallest circle which encloses the particle [133], of more than 500 particles, on TEM images of particle clusters, using ImageJ v.1.36b software.

For the investigation of the particle surfaces and internal structure, the TEM was operated at a high magnification between 300 000 and 1.5 million. Images were taken at different focus intervals, starting at an under-focus condition, moving through focus, and ending at an over-focus condition. The comparison of the atomic structure in the through focus images allowed for the identification of the image where the extended Scherzer defocus is at optimum [134]. Under such conditions the spherical aberrations of the TEM lenses are balanced by the shift in focal position so that maximum resolution is achieved.

5.1.2 X-ray powder diffraction

To determine the crystallinity of the powders, x-ray powder diffraction (XRD) was performed with a Panalytical PW3040/60 E'Pert Pro diffractometer, operated with CuKα radiation with a wavelength of 0.15406 nm, at 45 kV and 40 mA. The diffraction pattern was collected from 10° to 90° in 2θ at 0.02° steps. The diffractometer was equipped with a divergence slit of $^1/_8$°, an anti-scatter slit of ¼° and a detector mask of 7.5 mm. To achieve a high density and smooth surface for the XRD sample, the silicon nanopowders were compressed into 10 mm diameter tablets, directly onto double sided adhesive tape on a 12 mm square stainless steel plate (1mm thickness), with a pressure of 50 MPa. The same tablets were also used for Rutherford backscattering spectrometry, energy dispersive x-ray spectroscopy and Raman spectroscopy. Using a glass microscope slide, the powder tablets were positioned in the centre of the standard stainless steel XRD powder sample holder, using adhesive putty, in such a way that the top surface was level with the surface of the holder. No background subtraction was performed on any of the XRD patterns. From the XRD pattern the crystallite size t may be estimated by the Scherrer equation

$$t = \frac{K\lambda}{B\cos\theta_B}, \qquad (5.1)$$

where K is a constant dependant on the crystallite shape (taken as 0.9), λ is the x-ray wavelength and θ_B is the Bragg angle. B is the FWHM of the silicon nanoparticle

diffraction peak after corrections have been made for instrumental line broadening [135].

5.2 Compositional characterisation

5.2.1 Energy dispersive x-ray spectroscopy

Two systems were used for energy dispersive x-ray spectroscopy (EDX) to determine the bulk composition of the silicon nanopowders, both operated with an electron beam energy of 5 keV. A Leica S440 SEM and a Kevex 3600 EDX detector was used at a 200x magnification to collect spectra for 45 min, from a 400 x 400 µm area at a probe current of 1nA. A JEOL JSM7500F analytical Field Emission SEM and a Thermo Scientific UltraDry silicon drift detector were used to collect spectra at a 4000x magnification, for 120 seconds. The detector which has a ± 3 eV resolution achieved a count rate of more than 10000 counts per second during measurements, at a working distance of 8 mm. Using the Jeol system, phosphorus and boron concentrations were investigated using accelerating voltages of 15 keV and 2 keV respectively. In both cases the collection time was 600 seconds.

A typical EDX spectrum of a silicon nanopowder, in this case produced by SP at 80 mbar, with a 0.1% diborane concentration, is shown in figure 5.1.

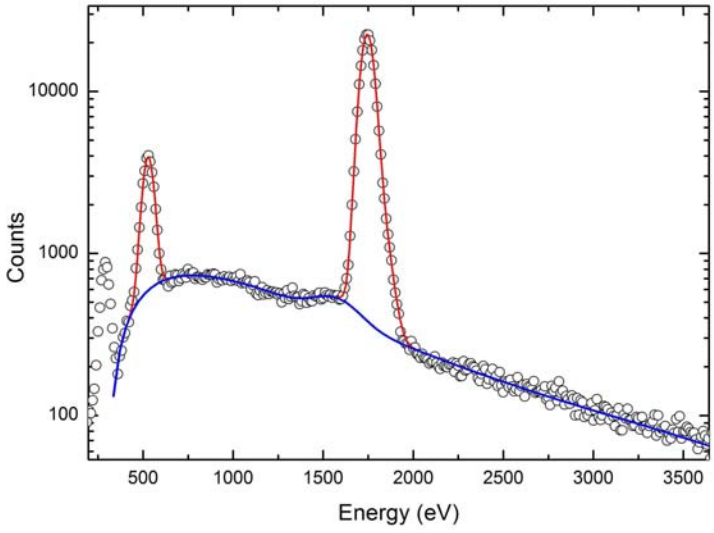

Figure 5.1 Example EDX spectrum of nanoparticles produced by SP with 0.1% diborane.

The peak intensities of oxygen and silicon were determined by a least squares fit to a model that incorporates a polynomial background (blue) as well as Gaussian functions for the Kα emission peaks of silicon and oxygen (red). The smaller peaks in the spectrum between the oxygen and silicon Kα peaks were treated as background and the carbon Kα peak at 250 eV was not considered in the analysis.

A quantitative EDX analysis of the powders was made possible by using an SiO_2 nanoparticle sample as a standard [136]. All nanoparticle samples, including the standard, were prepared and measured under the same conditions, such as time, beam energy and scanning area [137]. As the oxygen to silicon ratio of the stoichiometric SiO_2 standard is 2:1, the sensitivity factor k was calculated by

$$k = \frac{2Si_{Is}}{O_{Is}}, \qquad (5.2)$$

where Si_{Is} and O_{Is} are the measured silicon and oxygen x-ray intensities for the standard. For each subsequent sample the oxygen fraction was calculated as [138]

$$C_O = \frac{O_{Ip}.k}{Si_{Ip} + (O_{Ip}.k)}, \qquad (5.3)$$

where Si_{Ip} and O_{Ip} are the measured silicon and oxygen x-ray intensities of the silicon powder.

5.2.2 Rutherford backscattering spectrometry

Rutherford backscattering spectrometry (RBS), which allows elemental analysis of materials [136, 139], independent of chemical bonding [140], was used to verify the quantitative EDX results for a limited number of powders. RBS was performed with a 6 MV tandem Van der Graaff accelerator, at iThemba Labs, with helium ions (alpha particles) with acceleration energies between 1 and 4 MeV. To obtain substantial backscatter intensity from oxygen, the energy of the ion beam was adjusted to the resonant energy of oxygen [141-143]. The resonance was found by using a SiO_2 standard nanopowder in tablet form and collecting the RBS spectra in steps of 0.01 MeV, between 3.04 and 3.11 MeV. As evident from figure 5.2 the maximum resonance for oxygen, on this particular instrument, was found to be at 3.09 MeV. The solid line in this graph is a polynomial fit to the data.

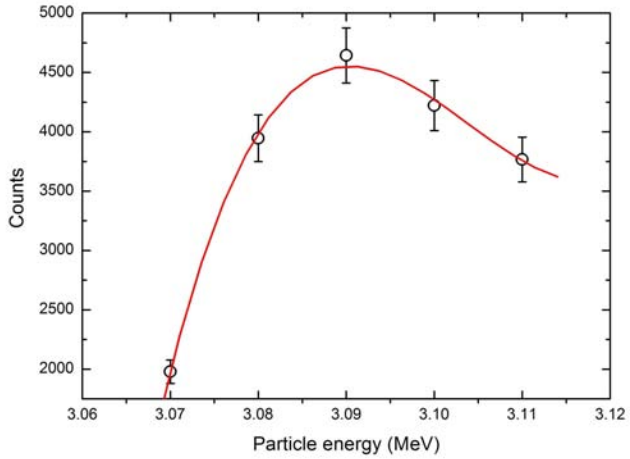

Figure 5.2 Peak intensities (and polynomial fit) of the SiO_2 peak of the RBS spectra collected at the different particle energies, using SiO_2 as a target.

All silicon nanopowders were measured at the resonance of 3.09 MV, with a beam current of 50 ± 2 nA. The beam spot on the sample surface was 2 mm and the scatter angle 165°, with a tilt angle of -10°. For calibration purposes, Pt/Si, Ti/Si and SiO_2/Si thin film samples where also measured together with each batch of silicon nanoparticle samples. As shown for the example in figure 5.3, all spectra were simulated with SIMNRA version 6.03, using the reaction file 6.03/CrSec/AO-_FE94A.RTR for oxygen, and the standard Rutherford reaction file for silicon to obtain quantitative information.

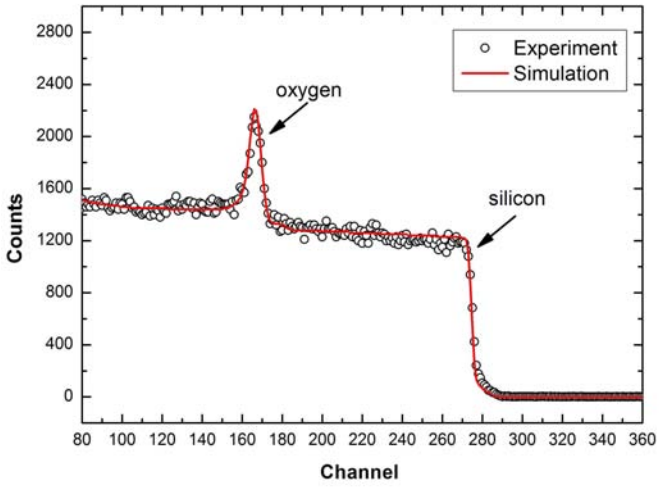

Figure 5.3 Example of the simulation fit to RBS spectra of intrinsic powder produced at 5 mbar, by HWTCP.

5.2.3 X-Ray photoelectron spectroscopy

X-Ray photoelectron spectroscopy (XPS) was used to determine the composition of the outer few nanometres of the nanoparticles [18, 144]. A Physical Electronics Quantum 2000 Scanning x-ray system using monochromatic Al Kα radiation, with a 100 μm spot size, with a raster scan over an area of 0.5 x 0.5 mm was used. For all samples three scans were performed: firstly a low resolution scan over the full energy range at 1 eV per channel, secondly a high resolution scan at 0.25 eV per channel spanning the silicon 2p photoelectron peaks, and finally a high resolution scan at 0.25 eV per channel spanning either the boron 1s peak or the phosphorus 2p peaks, depending upon the dopant gas during production. For all spectra, the instrumental energy shift was corrected with Physical Electronics Inc. Multipak V6 software, using the carbon 1s peak at 285 eV as a reference. The Background for each spectrum was subtracted using the iterative Shirley method [145-148], supplied with the same software. For each of the spectral regions of interest specific peaks were fitted, to describe the intensities of the specific atomic orbitals.

5.3 Spectroscopic characterisation

5.3.1 Raman spectroscopy

A Jobin Yvon LabRAM HR 800 equipped with an Olympus microscope, with a 0.5 x 50 objective, and a laser excitation wavelength of 514 nm, was used to collect Raman spectra from the compressed silicon nanopowder tablets, as prepared for XRD. It was found that the smooth surface of the dense tablet facilitated a stronger Raman signal and that samples were less prone to localised heating effects than loose powders. As Raman spectroscopy is more sensitive to the length, strength and arrangement of chemical bonds, than to the chemical composition [149], it was used to investigate the structural order in the particles. Bulk silicon crystal is characterised by a sharp longitudinal acoustic (LA) mode at 520.6 cm^{-1} [150-152], and a second order peak with a much lower intensity at about 960 cm^{-1}. A broad peak at 480 cm^{-1} corresponds to the longitudinal optical mode of the amorphous phase. In silicon thin films and nanoparticles the crystalline fraction (Xc) may be approximated by

$$X_C = \frac{I_C}{I_C + \gamma I_A}, \qquad (5.4)$$

where I_A and I_C are the integrated intensities of the LO peak at 480 cm^{-1} and the LA peak at 500-520 cm^{-1} respectively. To take into account the difference of the Raman backscattering cross section of crystalline and amorphous silicon, I_A may be multiplied by a correction factor γ, which is roughly 0.8 [153]. This calculation of crystalline fraction is often applied in un-doped [88, 154-156] and doped [157] silicon films, nanopowders [94] and nanowires [158]. Furthermore, the position and symmetry of Raman peaks obtained from measurements of silicon powders are affected by the size and shape of the particles. Generally a red shift (towards lower wave number) and broadening of first-order Raman spectra is observed for nanopowders [150, 151, 159] including silicon nanoparticles [94, 96, 160].

5.3.2 Fast Fourier transform infrared spectroscopy

Fast Fourier transform infrared spectroscopy (FTIR), is sensitive to chemical bond vibrations which may be affected by the local environment surrounding the vibration bond [59]. It is thus suitable to investigate the binding configuration of oxygen and hydrogen in the surface region of the silicon nanoparticles [79, 96, 161, 162]. Of interest to silicon nanopowders produced for this research is the ratio of the integrated intensity of absorption peaks at 2250 cm^{-1}, which result from surface Si-O vibrations [59] and at 2100 cm^{-1}, due to surface Si-H vibrations [59, 68]. Also of interest are the dual absorption peaks at 1050-1100 cm^{-1} and 1150-1200 cm^{-1}, corresponding to stoichiometric (SiO_2) and sub-stoichiometric (SiO_x , $x<2$) silicon oxide respectively [150, 163].

A Perkin Elmer Spectrum 100 FTIR spectrometer was used to collect transmission spectra between 450 and 3500 cm^{-1} at a spectral resolution of 0.4 cm^{-1}. Tablets were produced by mixing a very small quantity of the silicon nanopowder sample with 20 mg of KBr powder, grinding it to a fine powder using a mortar and pestle and then finally compressing it with a force of 7 tons into a 13 mm diameter disc of about 0.5 mm thickness. FTIR spectra were also collected in reflection geometry, between 550 and 3500 cm^{-1} at a spectral resolution of 0.4 cm^{-1}, by using the

instrument's stainless steel plunger to compress a few milligram of powder onto the diamond window.

5.4 Electrical characterisation

The electrical characteristics of nanopowders were determined using a system specifically constructed for that purpose. Figure 5.4 presents a diagram (a) and prototype (b) of the components and workings of the setup.

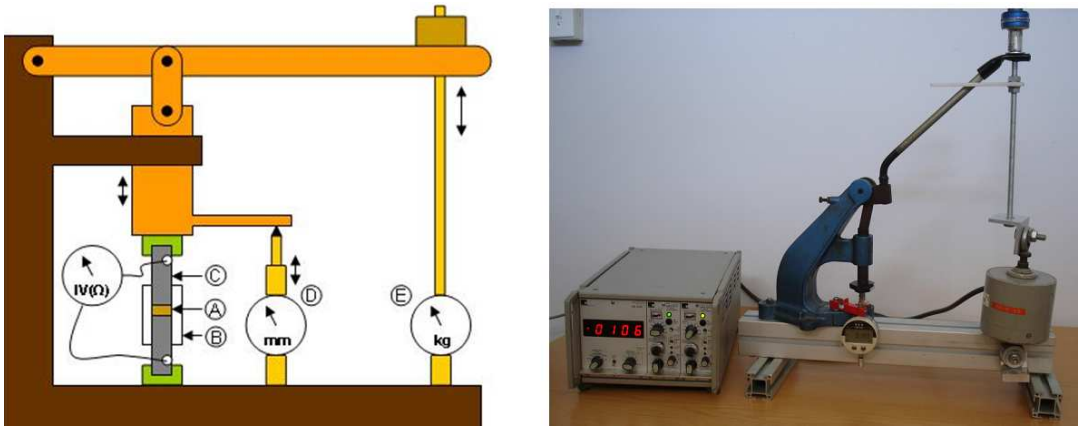

(a) (b)

Figure 5.4 (a) Diagram and (b) image of the measurement setup. (A) The powder, (B) plastic cylinder, (C) pistons, (D) micrometer and (E) load cell are shown in the diagram.

For each sample, about 20 mg of powder (A) was loaded into a plastic cylinder (B) of 8.85 mm internal diameter and compressed between two stainless steel pistons (C) which also serve as the electrical contacts. The applied force was set with a calibrated HBM DA3418 load cell (E) (1 kg force = 2.55 MPa) and the change in separation of the pistons was measured by a micrometer (D) to determine the compression. To enhance any capacitive effect in the powder, current—voltage (I-V) curves were measured in current sweeping mode at different degrees of compression, using a Keithley 4200 semiconductor characterisation system, at room temperature (23°C). A similar electrical characterisation approach has been used by other groups on lead dioxide powders [164], carbon black [165] and metal powders [166].

The conductivity of the compacted powders was determined in the ohmic region, from the measured resistance by

$$\sigma = \frac{h}{RA}, \qquad (5.5)$$

where h is the distance between the contacts, R the resistance, and A the cross sectional area of the compressed powder. Similarly, the effective density of the powder is given by

$$\rho = \frac{m}{hA}, \qquad (5.6)$$

where m is the mass of the powder used in the measurement.

The resistivity of compressed powder is expected to be orders of magnitude higher than the bulk of the same material [164, 165] and depends primarily on the packing density (compression) and geometry of the particles, which affect the contact area between particles, to which electron flow is restricted [167], as well as the surface properties of the particles.

6. RESULTS

As described in chapter 4, silicon nanoparticles were produced by both HWTCP and SP. Three sets of nanopowders were produced by each method, firstly with silane only, secondly with a mixture of diborane and silane, and thirdly with a mixture of phosphine and silane. Each production run resulted in a layer of powder covering all inside surfaces of the reaction chamber. For HWTCP, depending on the production parameters, the powder varied in colour between wine red, at production pressures below 10 mbar, and ochre to brown at 20 mbar and higher. Powders produced by SP at 80 mbar were ochre in colour. A similar colour range has been reported for intrinsic silicon nanoparticles produced by plasma enhanced chemical vapour synthesis [96]. In this chapter a more detailed characterisation of the silicon nanopowders and the nanoparticles forming them will be determined by investigating their agglomeration, shape, size, internal and external structure as well as their composition, spectroscopic and electrical behaviour.

6.1 Structural characterisation

6.1.1 Agglomeration and aggregation

All powders produced by HWTCP and SP, independent of the type and concentration of the dopant gas or pressure, exhibit two main particle configurations: clusters of loose particles and chain-like aggregated (sintered) particle clusters. The TEM micrographs of intrinsic nanoparticles produced by HWTCP at 40 mbar (figure 6.1 (a)) and nanoparticles produced by SP (figure 6.1 (b)) are examples of the first category, clusters of loose particles.

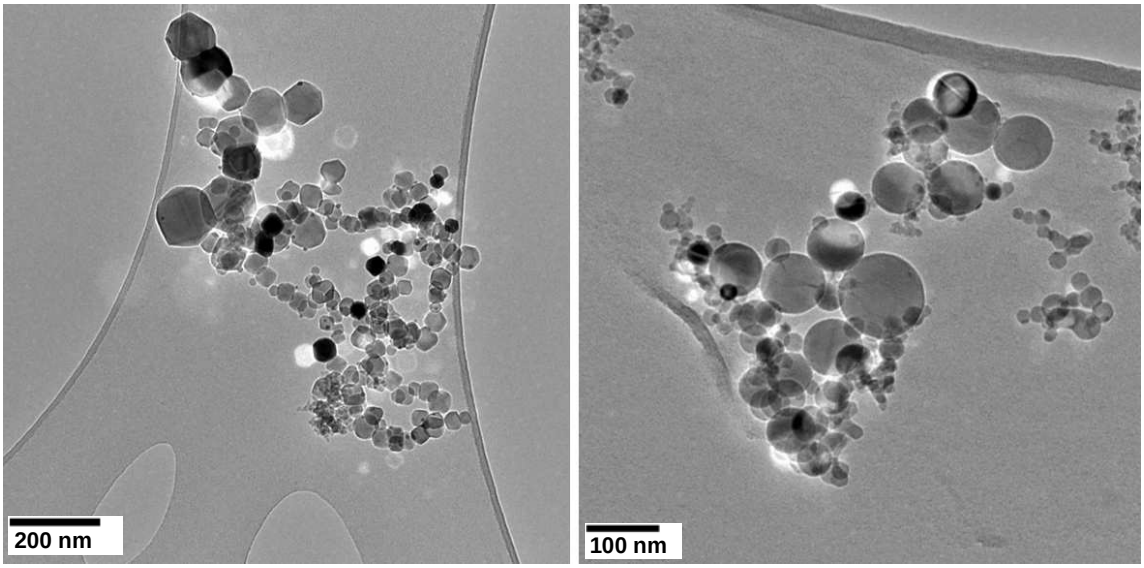

(a) (b)

Figure 6.1 TEM images of clusters of individual intrinsic nanoparticles produced by: (a) HWTCP at 40 mbar and, (b) SP (the white shadows are an artefact of electron beam/particle interaction).

The particles produced by HWTCP (figure 6.1 (a)) appear to be in contact with each other so as to form rings of particles. Furthermore particles of equal size seem to group together. On the other hand particles produced by SP (figure 6.1 (b)) tend to form bunches rather than chains. It is observed that both samples contain particles of various sizes. On the same TEM grids there were also highly agglomerated clusters of particles as seen in figure 6.2 (a) and (b). These clusters appear to be constituted of a number of fused particles, each of a similar size. Such aggregation is observed for all different particle sizes, and appears in powders produced by both HWTCP (figure 6.2 (a)) as well as SP (arrow in figure 6.2 (b)). However, based on the TEM investigation of a large number of clusters, chosen at random on different parts of the grid, powders produced by SP have fewer larger particles in a fused state, than powders synthesised by HWTCP. From an investigation of a number of clusters, chosen at random, a rough estimate suggests that fused clusters make up between 10 and 20% of any powder.

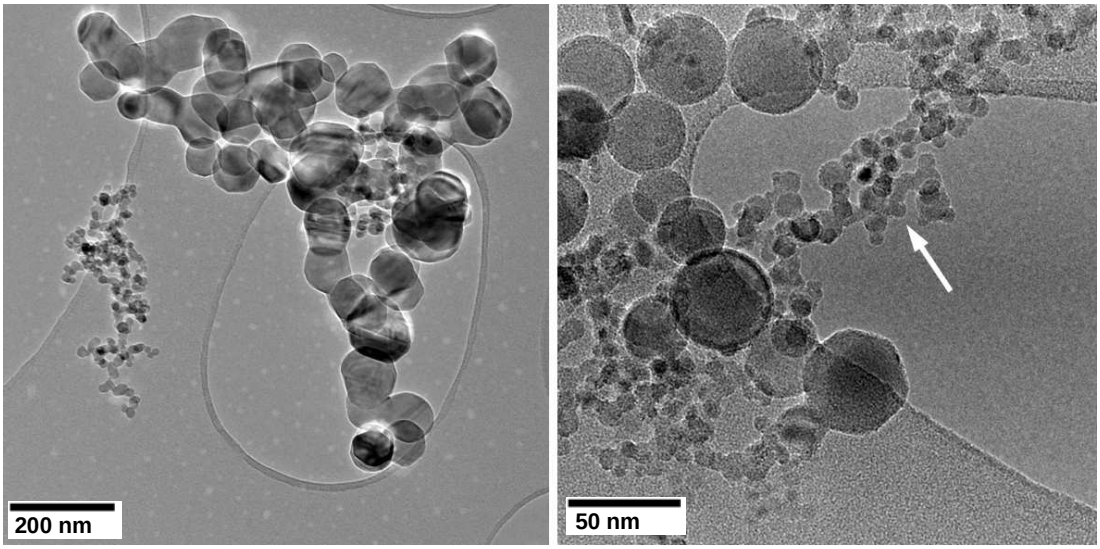

(a) (b)

Figure 6.2 TEM images of fused intrinsic particles produced by: (a) HWTCP at 40 mbar and, (b) SP.

Silicon nanoparticles produced by HWTCP at a pressure of 5 mbar, shown in the TEM image in figure 6.3, appear to be highly agglomerated or possibly aggregated. Such an agglomeration is generally expected for nanopowders with small particle diameters [132]. The particles are shown at relatively low magnification where the internal structure (lattice) may not be visible.

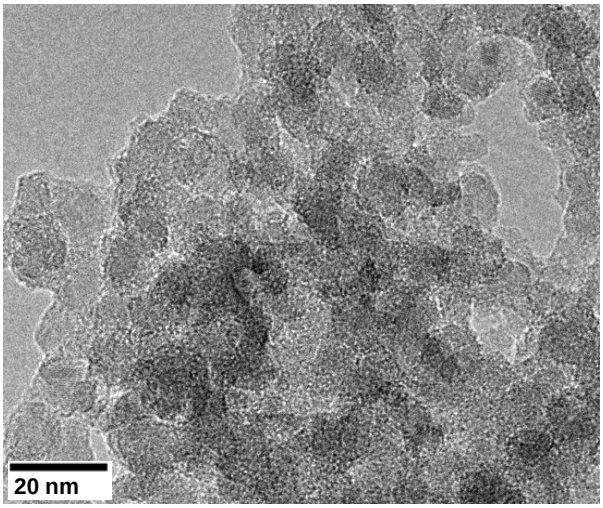

Figure 6.3 TEM image of intrinsic silicon nanoparticles produced by HWTCP at 5 mbar.

6.1.2 Shape

The TEM images shown in Figure 6.4 illustrate the different shapes of the silicon nanoparticles. The shape of the loose particles produced by HWTCP at 40 mbar (a), are multifaceted, while those produced by SP (b) are spherical.

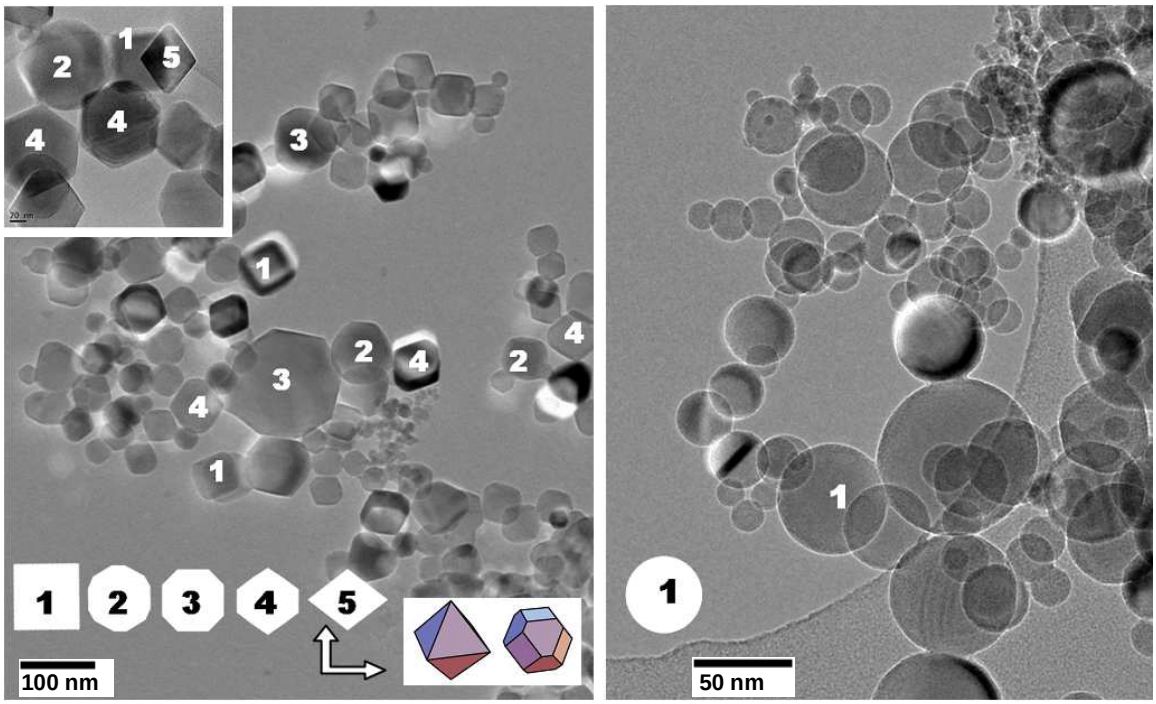

(a) (b)

Figure 6.4 (a) Multifaceted nanoparticles produced by HWTCP at 40 mbar with pure silane (main photograph), and with a mixture of silane and 1% diborane (inset). (b) Spherical nanoparticles produced by SP.

Furthermore, the TEM micrographs of particles produced by HWTCP in figure 6.4 (a), represent different projected views of the same basic morphology (see inset) with a shape ranging from an octahedron to a truncated octahedron [168]. Independent of the dopant gas and its concentration during production, the powders generally constitute a mixture of all shapes throughout the size range. In contrast, all particles produced by SP (figure 6.4 (b)) are spherical, independent of the dopant gas used or the size of the nanoparticles.

6.1.3 Size

The histograms of the size distribution of nanopowders are given in figure 6.5. The distributions were determined by measuring the diameter of more than 500 particles per sample, from randomly chosen particle clusters.

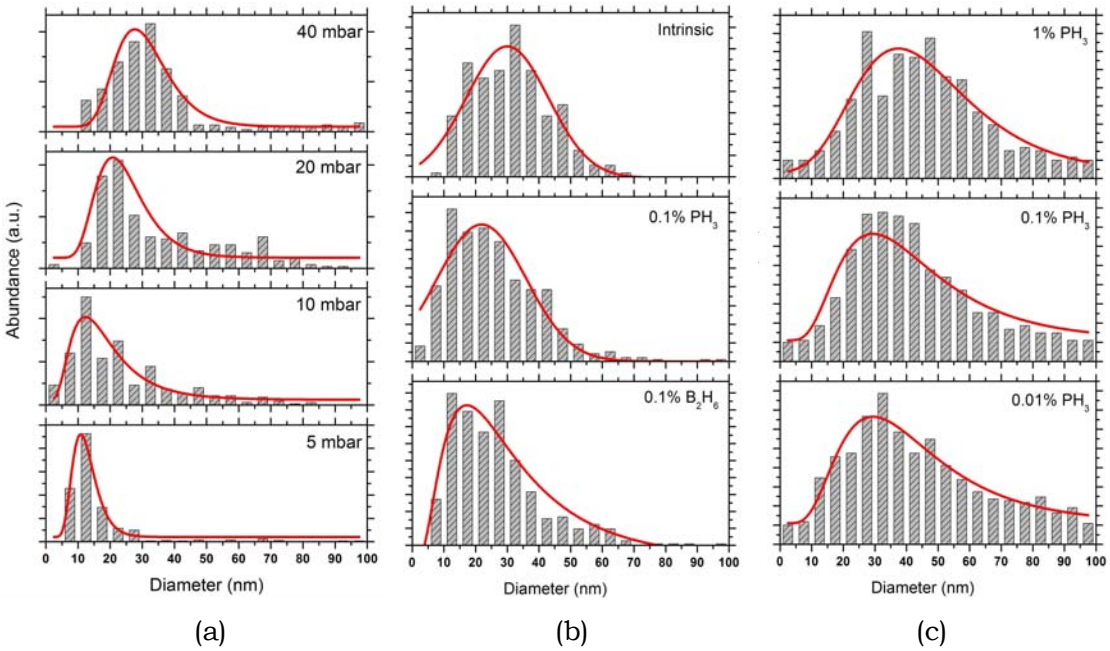

Figure 6.5 Histograms of particle size distributions of (a) intrinsic particles produced by HWTCP at changing pressures; (b) particles produced by SP at 80 mbar, intrinsic and at 0.1 % phosphine and diborane doped gas concentrations; and, (c) particles produced by HWTCP at 40 mbar with varying phosphine dopant gas concentrations. All histograms are fitted with log-normal functions.

Considering the size distributions given in figure 6.5, the mean particle diameter of all particles produced by HWTCP or SP, irrespective of dopant gas concentration or production pressure, is below 50 nm. The size distribution of intrinsic particles produced by HWTCP at pressures of 5, 10, 20 and 40 mbar is represented by the histograms in (figure 6.5 (a)). An increase in production pressure results in an increase in the average particle size from about 11 nm up to 34 nm, accompanied by a broadening of the size distribution. A small percentage of nanoparticles with diameters up to 150 nm are also present in these powders. Silicon nanoparticles

produced by SP (figure 6.5 (b)), show a slight decrease in mean particle diameter from intrinsic particles (~28 nm) to powder produced at 0.1% phosphine (~22 nm) and 0.1% diborane (~18 nm) dopant gas concentrations. A similar average size of approximately 27 nm for spherical particles produced by laser pyrolysis has been reported [169].

Figure 6.5 (c) presents the size distribution of particles produced by HWTCP at 0.01, 0.1 and 1 % phosphine dopant gas concentrations. The average size and distribution do not appear to be significantly affected by the dopant gas concentration. However, compared to the average size and distribution of the SP particles produced with phosphine (~22 nm), given in figure 6.5 (b), the nanopowders produced by HWTCP have a larger average size of approximately 30 to 38 nm and a higher fraction of larger particles.

The powders collected at locations X, Y and Z in the HWTCP reaction chamber, where they differ in colour (chapter 4, figure 4.14(b)), were also investigated by TEM. As shown in figure 6.6 (powders from position X and Z), the lighter coloured powder generally constitutes a greater percentage of larger, loosely packed particles than the darker coloured powder (figure 6.6 (Y)), which is generally made up of a high percentage of smaller, chain-like agglomerated particles.

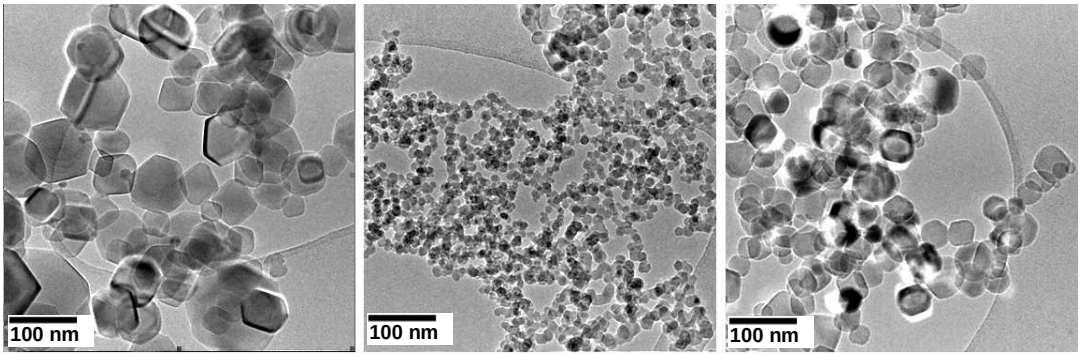

Figure 6.6 Comparison of TEM images of powder collected at positions X, Y and Z, as indicated in figure 4.14(b), where X and Z are ochre coloured and Y is reddish-brown.

This link between colour and particle size is further supported by the colour change observed in the intrinsic powder produced by HWTCP at different pressures (chapter 4, figure 4.15), and the size distribution of these powders given in figure 6.5 (a). Powders produced at lower pressure, which tend to be darker in colour and redder, are on average smaller than those produced at higher pressure.

6.1.4 Internal structure

The internal structure of individual particles was investigated by TEM, at high magnification, and by XRD. As revealed, in the TEM images in figure 6.7, by the lattice structure visible over the full particle, loose particles produced by both (a) SP and (b) HWTCP are mainly monocrystalline.

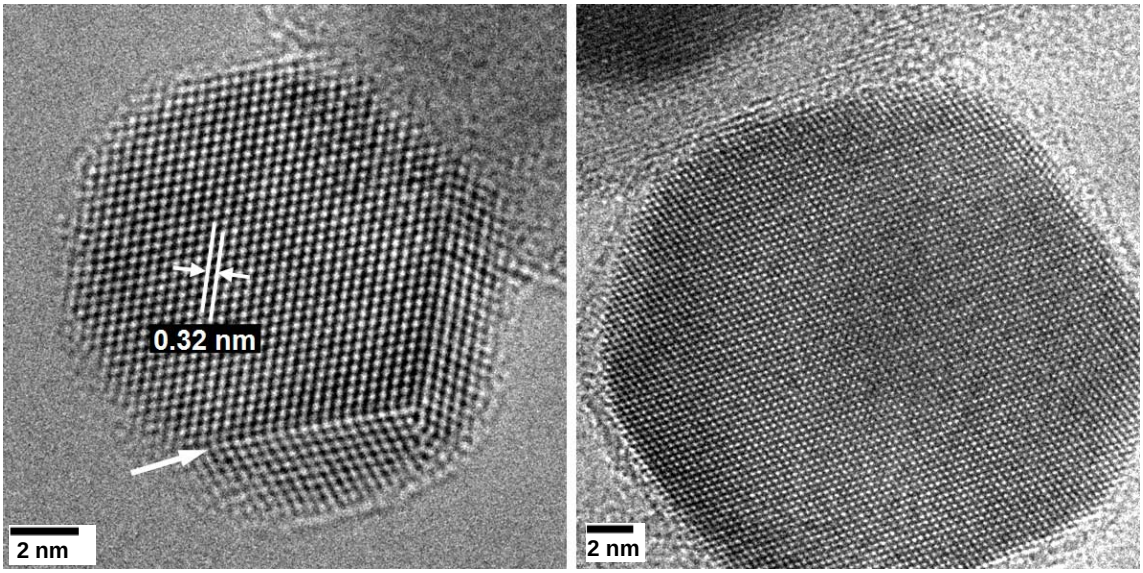

(a) (b)

Figure 6.7 TEM images of monocrystalline silicon nanoparticles produced by: (a) SP with 0.1% diborane and (b) HWTCP at 40 mbar and 0.01 % diborane. Some particles exhibit twinning (arrow in (a)).

The (111) lattice planes can be identified by their interplanar distance of 0.32 nm as indicated in figure 6.7 (a). All particles produced at pressures larger than 20 mbar, by HWTCP or SP, irrespective of dopant gas concentration and size, exhibit high crystallinity. Twinning, as indicated by the arrow in figure 6.7 (a) may be found in a small number of the loose silicon nanoparticles produced by either method. However in the fused nanoparticles produced by HWTCP or SP, shown in figure 6.8,

twinning, multiple grain boundaries and lattice mismatches are the dominant structures.

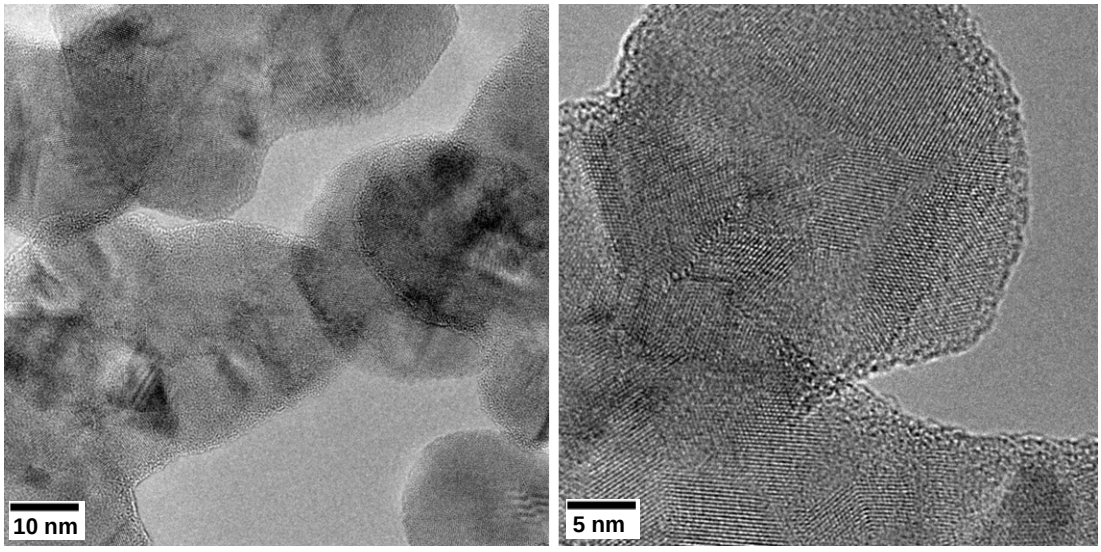

(a) (b)

Figure 6.8 (a) TEM images of fused silicon nanoparticles produced by HWTCP at 40 mbar and 1% diborane gas concentration. (b) Higher magnification image showing multiple grain boundaries and twinning.

As evident from the high magnification TEM image in figure 6.8 (b) the twinning and lattice mismatches are not limited to the interface region between the fused particles but extend into the full volume of the polycrystalline nanoparticles.

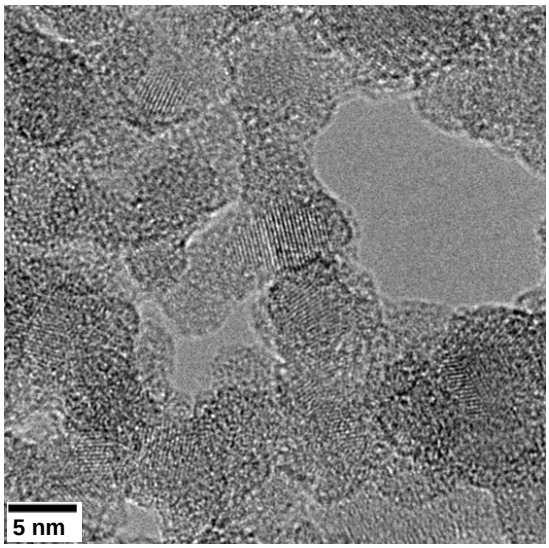

Figure 6.9 TEM image of silicon nanoparticle produced by HWTCP at 5 mbar, at a 0.1% diborane concentration. Crystallites are clearly visible.

Compared to nanopowders produced at higher pressure, silicon nanoparticles produced by HWCVD at 5 mbar (figure 6.9), constitute smaller aggregated particles with a crystalline core, which appear to be fused together within an amorphous phase. This is the same sample as shown in Figure 6.9 at a higher magnification.

The crystallinity of the bulk powders was also investigated by x-ray powder diffraction (XRD). All powders were measured in the form of compressed tablets, produced as described in chapter 5. The XRD patterns of silicon nanopowders produced by HWTCP at 40 mbar with phosphine concentrations of 0.01, 0.1 and 1% are shown in figure 6.10. The diffraction peaks are labelled with their corresponding Miller indices.

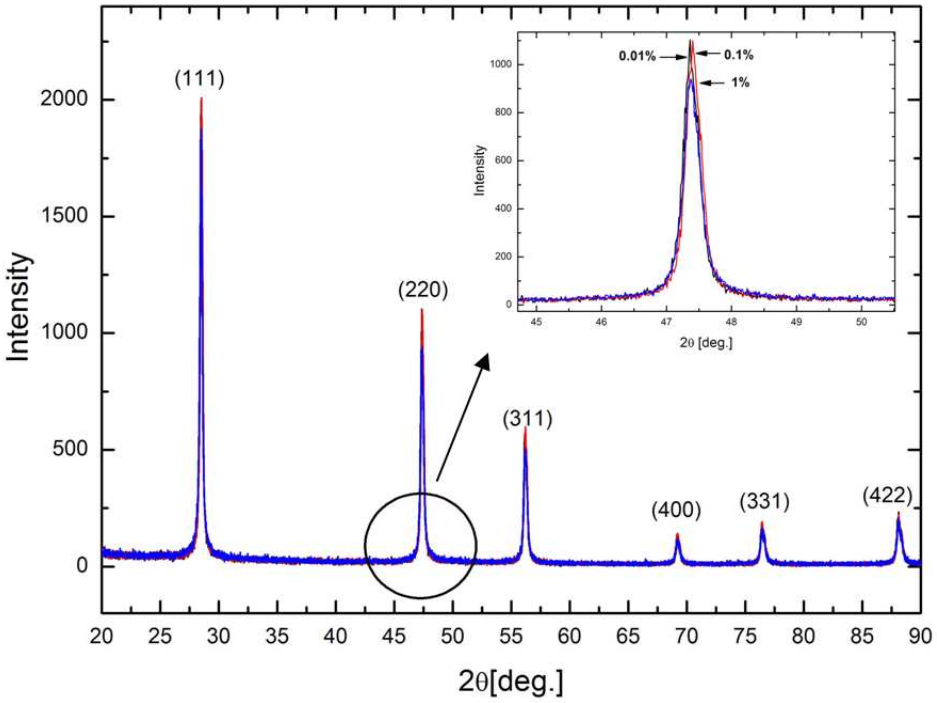

Figure 6.10 XRD patterns of powders produced by HWTCP at 40 mbar with phosphine concentrations of 0.01, 0.1 and 1%. The inset is an expanded view of the (220) diffraction peak.

From the narrow, well defined peaks in the XRD patterns, which do not show any contribution from an amorphous phase, shown in figure 6.10, the crystalline nature of the powders is evident. The sharp peaks at 28.5°, 47° and 56° corresponds to the (111), (220) and (311) crystal planes of crystalline silicon [170, 171]. Furthermore

the three higher order peaks at 69° (400), 76.5° (331) and 88° (422) [3] are also clearly visible in the patterns. As can be seen in the inset, no significant differences in intensity or width (FWHM) of the XRD peak for powders produced at increasing dopant gas concentrations are observed.

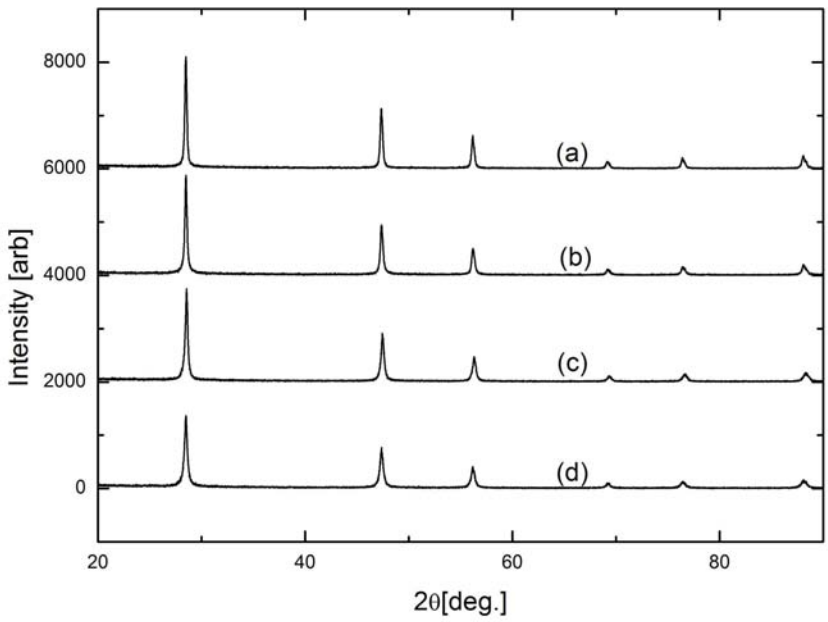

Figure 6.11 XRD patterns of silicon nanopowders produced by HWTCP at 40 mbar with (a) 1% diborane and (b) 1% phosphine as well as silicon nanopowders produced by SP with (c) 1% phosphine and (d) 1% diborane.

Also from the XRD patterns shown in figure 6.11, no significant differences can be observed between XRD patterns of powders produced by HWTCP and SP at pressures of 40 and 80 mbar respectively, irrespective of the dopant gas used or the dopant gas concentration. In contrast the XRD pattern of powder produced by HWTCP at 5 mbar with a 0.1% phosphine concentration (figure 6.12 (a)) has diffraction peaks which are lower in intensity, compared to powder produced under the same conditions at 40 mbar (b), which are superimposed on an underlying broad background. This indicates a lower crystalline fraction in the powder produced at the lower pressure. The peak broadening of nanopowders produced at 5 mbar may be attributed to their smaller average crystallite size compared to that of particles produced at 40 mbar.

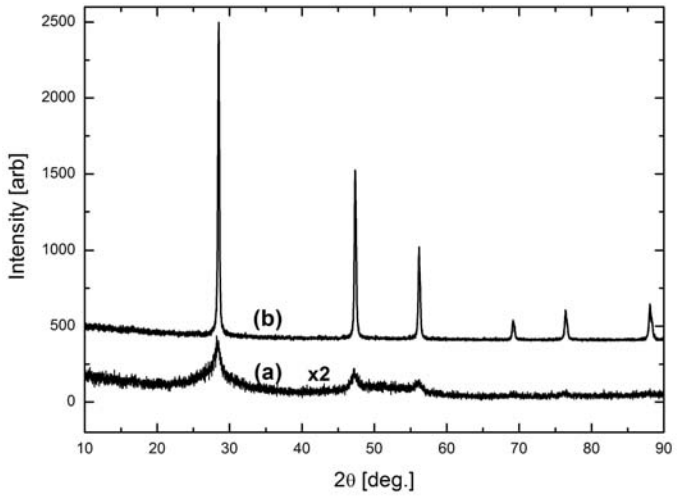

Figure 6.12 (a) XRD pattern of nanoparticles produced by HWTCP at 5 mbar, and (b) XRD pattern of intrinsic silicon nanoparticles produced by HWTCP at 40 mbar.

The average crystallite size of nanopowders was estimated by applying the Scherrer formula [172], using the FWHM of a Lorenzian fit to the (111) diffraction peak. The estimated average crystallite size of all powders, calculated using the same method, is shown in figure 6.13.

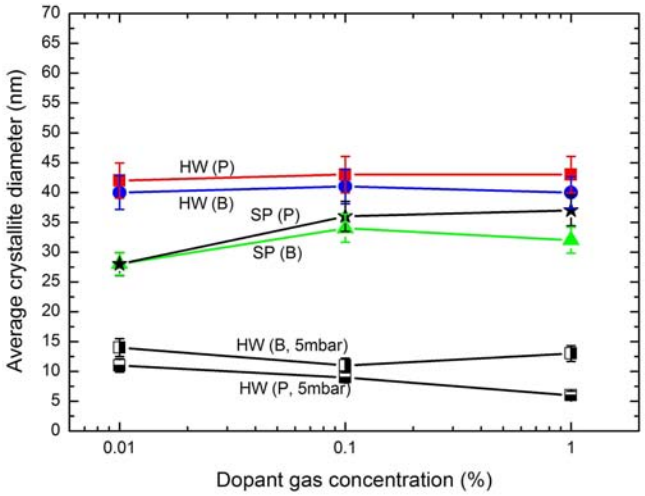

Figure 6.13 Estimate average crystallite size of all silicon nanopowders as determined by the application of the Scherrer equation on the 28.5° XRD line. (Error bars taken as 5% of calculated value).

As evident from this figure, silicon nanopowder produced by HWTCP at 40 mbar (HW(P) and HW(B)), has the largest crystallites in the 40 to 50 nm size range,

followed by nanopowders produced by SP (SP(P) and SP(B)) for which the crystallite size falls in the 30 to 40 nm range. In contrast, powders produced by HWTCP at a pressure of 5 mbar have the smallest crystallites, between 5 and 15 nm.

6.1.5 Surface structure

Using TEM at high magnification, a thin outer layer of a general amorphous nature can be seen on some of the silicon nanoparticles, but there are also regions where the silicon lattice planes can be seen to extend to the surface. The thickness of the thin outer layer varies, depending upon the process and production conditions.

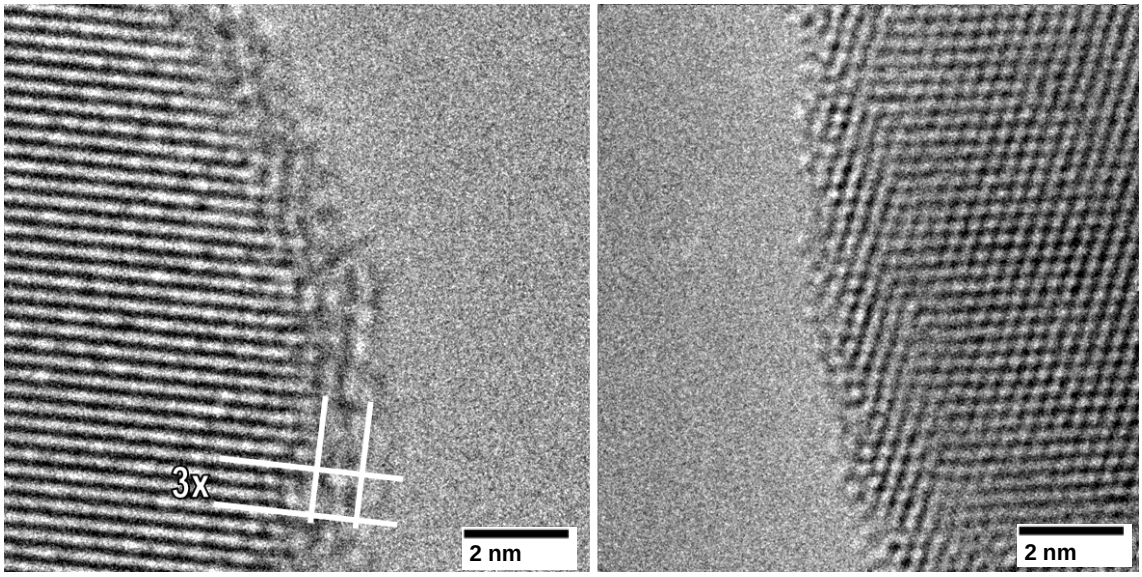

Figure 6.14 Surface structure of nanoparticles produced by SP with (a) 0.01% phosphine, and (b) 0.1% diborane.

In figure 6.14 (a), the amorphous layer on a particle produced by SP with 0.01% phosphine is visible. Its thickness is comparable to the distance between approximately 3 of the (111) crystal planes, as shown by the highlighted square. In the particle shown in figure 6.14 (b), which was produced by SP with 0.1% diborane, the crystal structure extends fully, up to the outer atomic layer of the particle. It thus appears as though the structural disorder is limited to the outer atomic layers of the particle, and that there is no additional amorphous shell.

The images presented in figure 6.14 and figure 6.15, serve as an example of the surface structure of samples of silicon nanoparticles investigated by TEM. As will be shown in section 6.2.2, a better measure of the average thickness of the amorphous layer covering some silicon nanoparticles and its composition, will be concluded by XPS measurements.

In the second example, TEM images of particles produced by HWTCP at 40 mbar with 1% phosphine (figure 6.15 (a)) and 1% diborane (figure 6.15 (b)) are shown.

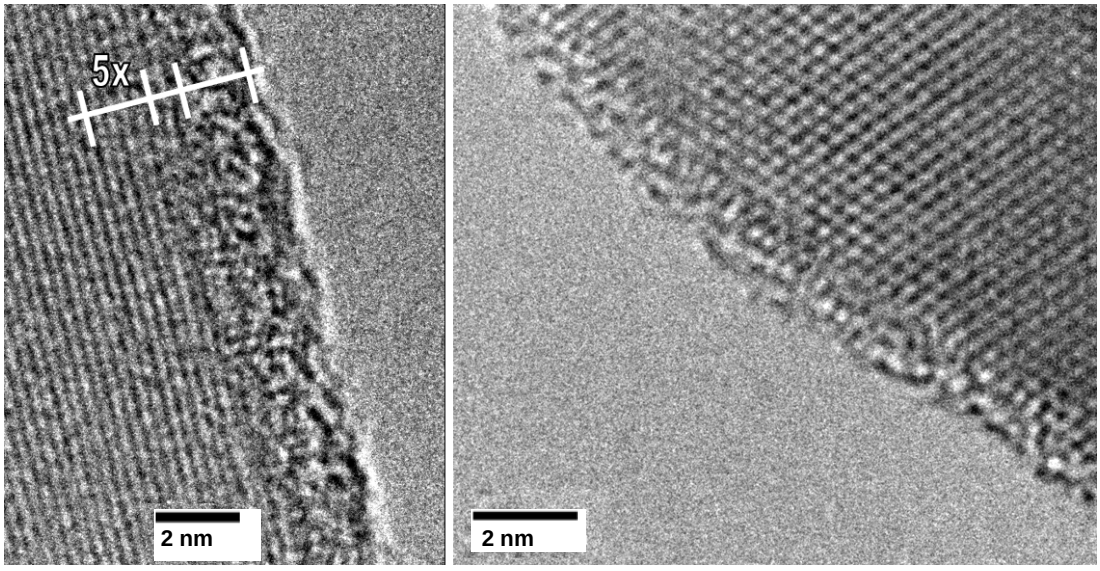

Figure 6.15 Surface structure of nanoparticles produced by HWTCP at 40 mbar, with (a) 1 % phosphine, and (b) 1% diborane.

In the TEM micrograph shown in figure 6.15 (a), of a particle produced by HWTCP at 40 mbar, with 1% phosphine, an amorphous outer layer is clearly visible. The amorphous layer thickness is comparable to the distance between about 5 of the (111) crystal planes. In contrast, the crystal structure in the particle produced by HWTCP with 1% diborane, shown in figure 6.15 (b), extends to the outer last atomic layers of the particle. In nanopowders produced by HWTCP at 5 mbar, the surface region of a single particle is difficult to define, because the particles are surrounded by an amorphous tissue, indicated by the arrow (a) in figure 6.16.

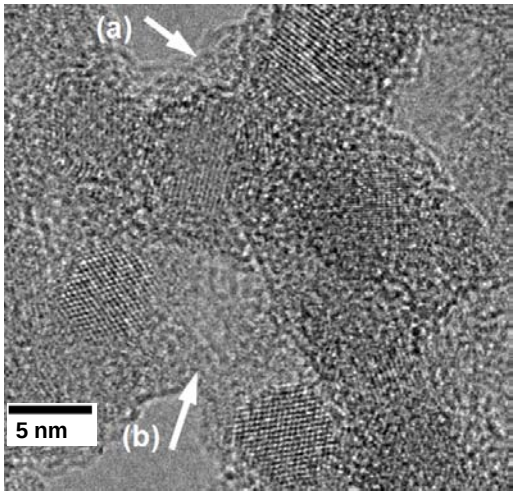

Figure 6.16 Silicon nanoparticles produced by HWTCP at 5 mbar and 0.1% diborane concentration.

However what appears to be another amorphous region, shown by the arrow (b), may be attributed to particles that are not in diffraction condition and hence show no lattice planes.

6.2 Compositional characterisation

Energy dispersive x-ray spectroscopy (EDX) was used to determine the bulk composition of the silicon nanopowders. For a detailed analysis of the composition of the surface region, which is approximately the first 2 nm of the particles, x-ray photoelectron spectroscopy (XPS) was used.

6.2.1 Bulk composition

An example of an EDX spectrum of a silicon nanopowder produced by SP at 80 mbar with 1% phosphine dopant gas is shown in figure 6.17. The strong x-ray peaks at 520 eV and 1735 eV indicate that the powder constitutes mainly oxygen and silicon respectively.

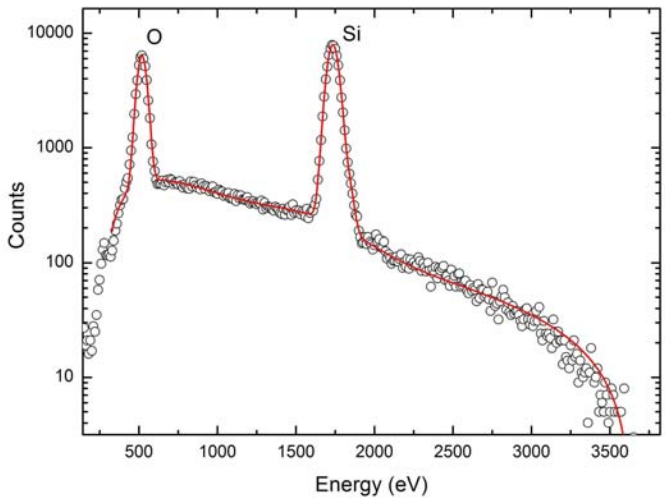

Figure 6.17 XRD spectrum of a silicon nanopowder produced by SP at 80 mbar and 1% phosphine concentration. The peaks at 520 eV and 1735 eV originate from oxygen and silicon respectively.

The oxygen content of each silicon nanopowder was determined by fitting peaks to the spectrum and calibrating with an SiO_2 standard as described in chapter 5. The total oxygen content of all samples produced by HWTCP and SP at pressures of 40 and 80 mbar at 0.01, 0.1 and 1 % dopant gas concentrations is given in figure 6.18.

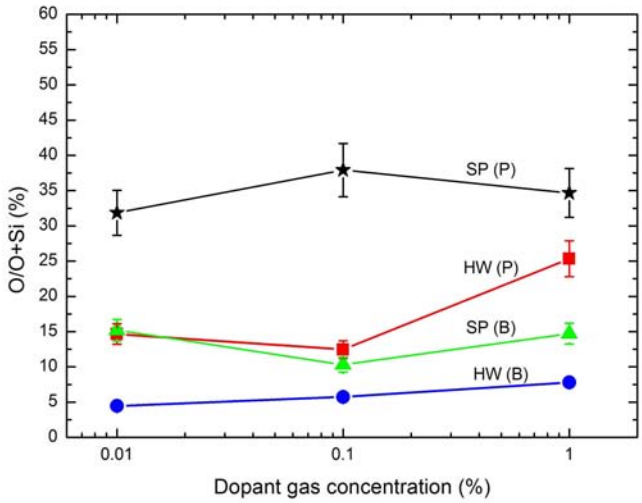

Figure 6.18 Comparison of the oxygen ratio of the silicon nanopowders produced by HWTCP and SP at 40 and 80 mbar respectively, at different dopant concentrations.

From figure 6.18 it may be concluded that, silicon nanopowders produced in the presence of dopant gas exhibit an increase in oxygen content with an increase in dopant gas concentration. Silicon nanopowders produced by SP and HWTCP with phospine have a higher oxygen content than powders produced with the same processes using diborane as the dopant. In general powders produced by HWTCP with diborane or phosphine, contain less oxygen than those produced by SP. In comparison, the oxygen content of powder produced by HWTCP at 5 mbar with a 0.1% diborane concentration is 48% but with 0.1% phosphine concentration increases to 64%. This higher oxygen content in powders produced at 5 mbar, compared to powders produced at higher pressures, is also observed in the oxygen content of the intrinsic series shown in figure 6.19. The oxygen content of intrinsic silicon nanopowder, as measured by EDX, increases with a decrease in the production pressure. Furthermore, as shown in figure 6.19, Rutherford backscattering spectrometry (RBS) measurements on the same silicon nanopowders are consistent with the EDX measurements. The systematically lower concentration obtained from the RBS measurements can be attributed to the fact that lighter elements generally have a lower backscatter cross-section [141-143], which may not be fully compensated for by the oxygen resonance reaction file in the RBS simulation software, SIMNRA.

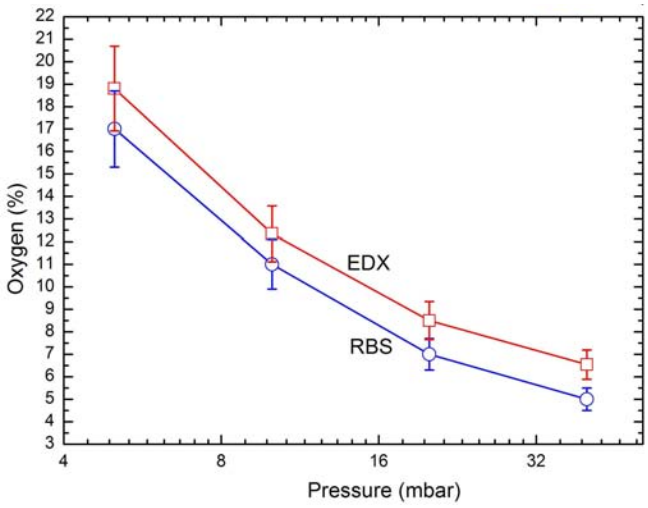

Figure 6.19 Comparison of oxygen content measured by EDX (□) and RBS (o), of intrinsic silicon nanopowders produced by HWTCP at different production pressures.

To determine if dopant atoms have been incorporated in the particles, EDX spectra of the powders produced with phosphine and diborane were collected at 15 kV and 2 kV respectively. In figure 6.20 the spectra of powder produced by SP with 0.01% to 0.1% and 1% phosphine concentrations is shown.

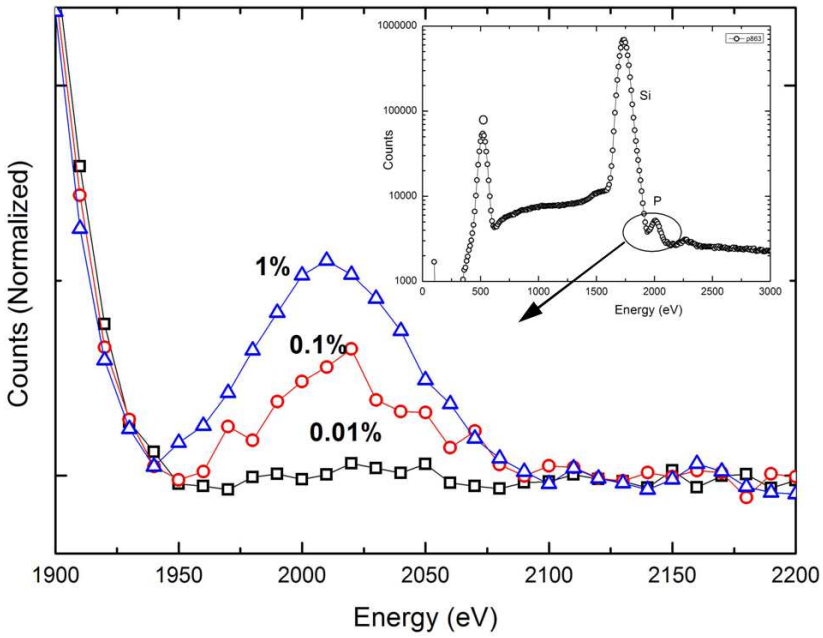

Figure 6.20 EDX spectra of particles produced by SP at 80 mbar showing an increase of phosphorus in the powder for an increase in phosphine concentration (from 0.01% to 0.1% and 1%) during production.

As shown in the inset of figure 6.20 the phosphorus peak is clearly visible at an energy of about 2020 eV. Furthermore, as shown by the main graph, an increase in phosphine concentration during the production, results in an increase in the peak intensity, indicating an increase in phosphorus atoms in the powder. In figure 6.21 the phosphorus atom concentrations of all powders produced with phosphine dopant gas are given as a percentage of the silicon peak measured by EDX. As can be seen, an increase in phosphine dopant gas concentration during production, results in an increase in the number of phosphorus atoms in the powder irrespective of whether the particles are produced by HWTCP at 40 mbar or by SP.

For both EDX instruments the boron Kα line at 182 eV was below the detection limit of the instruments, and thus could not be measured.

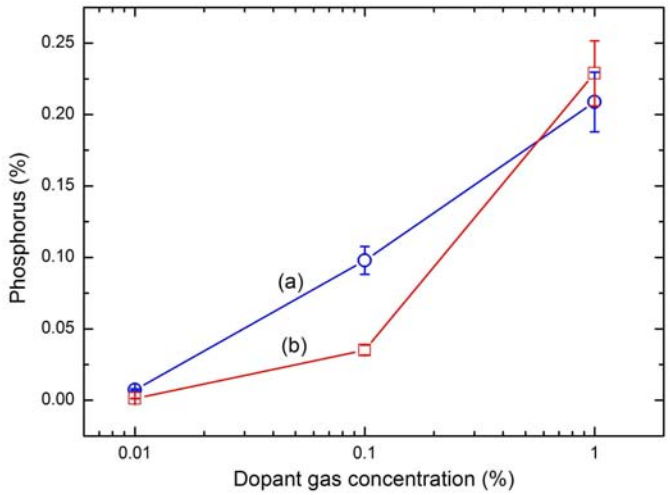

Figure 6.21 Concentration of phosphorus atoms as measured by EDX, on powders produced by (a) HWTCP at 40 mbar and (b) by SP, with increasing phosphine dopant concentrations.

6.2.2 Surface composition

The composition of the near surface region of the silicon nanoparticles was investigated using XPS, as described in chapter 5. The areas of interest in the XPS spectrum are the silicon 2p peaks at around 100 eV, the phosporus 2p peaks at 130 eV and the boron 1s peak at 188 eV. Silicon loss peaks (Ω_{Si}), expected at 117, 134, 167 and 184 eV were taken into consideration in the fitting of the peaks of interest.

As shown in figure 6.22, after subtraction of the background, a best least squares fit of the Si 2p peak was achieved by fitting all five peaks corresponding to the different oxidisation states of silicon [173] as shown in the spectrum at about: 99.0 eV (Si), 100.0 eV (Si^{1+}), 100.65 eV (Si^{2+}), 101.5 eV (Si^{3+}) and 103.0 eV (Si^{4+}). The Si^{4+} peak represents stoichiometric silicon oxide (SiO_2).

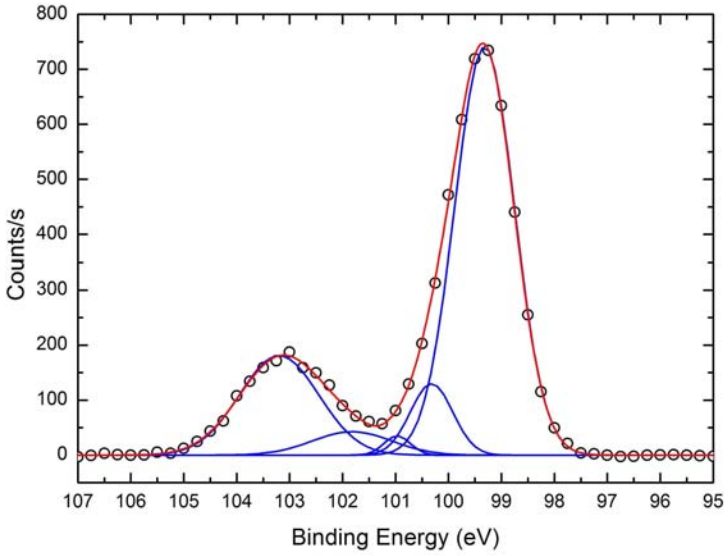

Figure 6.22 Photoemission energy spectrum of the Si 2p peak, of powder produced by SP with 0.1% phosphine concentration. The best least squares fit was achieved, with 5 Gaussian peaks at about: 99.0 eV (Si), 100.0 eV (Si^{1+}), 100.65 eV (Si^{2+}), 101.5 eV (Si^{3+}), 103.0 eV (Si^{4+}).

From the XPS spectrum in figure 6.22 it is apparent that the top 2 – 3 nm of particles contains fully oxidised silicon, confirming that the amorphous layer on the silicon nanoparticles observed by TEM constitutes SiO_2.

In figure 6.23 (a) and (b) the integrated intensities of the three sub-oxides and the silicon oxide XPS peaks of silicon nanopowder produced by SP are given. As apparent from figure 6.23 (a), oxides increase slightly with increasing diborane concentrations in powders produced with diborane. However, in powders produced with phosphine (figure 6.23 (b)), the ratio of Si^{4+} to the other silicon sub-oxides increases markedly at higher phosphine concentrations. The same trend is observed for silicon nanoparticles produced by HWTCP at 40 mbar with phosphine and diborane.

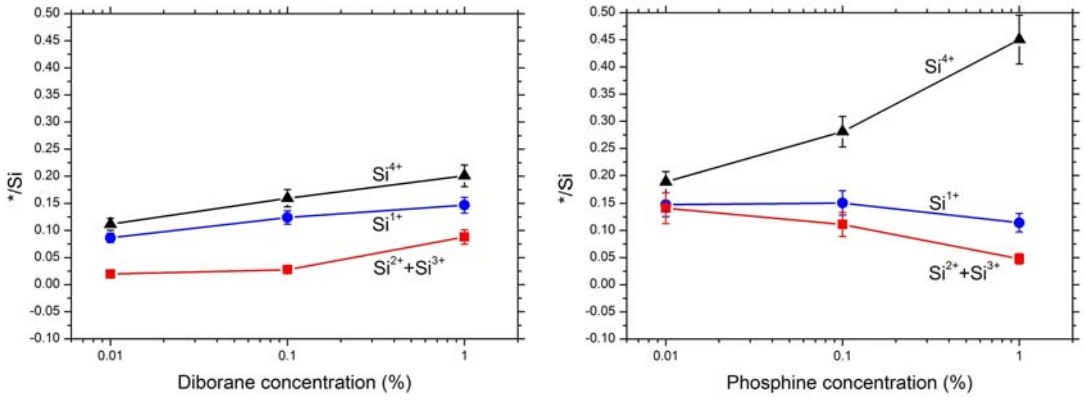

Figure 6.23 A comparative plot of the intensities of the three sub-oxide and fully oxidised silicon photoemission peaks from silicon nanopowders produced by SP with: (a) diborane and (b) phosphine.

To estimate the shell thickness on the silicon nanoparticles, attributable to SiO_2, the ratio of Si to SiO_2 (Si^{4+}), as determined by fitting the 5 Gauss functions to the silicon 2p peaks was used [174]. For powder, if the average separation between particles (or clusters) is at least equal to their radius R, all possible take-off angles are sampled. The effective photoelectron escape depth λ is then given by the geometrical average over all possible angles to the particle surface.

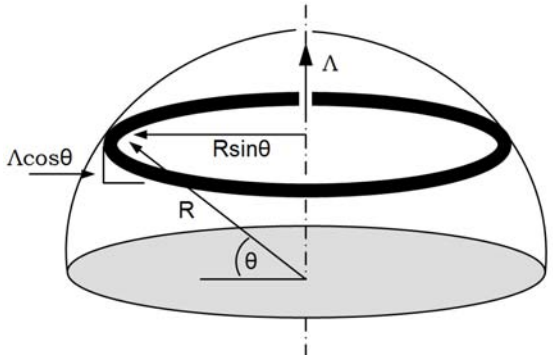

Figure 6.24 Graphic presentations of the take-off angles of excited electrons in XPS of a powder.

The ring element shown in figure 6.24 has a surface area

$$dA = 2\pi R \sin\theta R d\theta, \qquad (6.1)$$

where θ is the complementary angle to the take-off angle.

From elementary geometrical considerations the weighted average λ of the escape depth Λ is [174]

$$\lambda = \frac{1}{A}\int_0^{\pi/2} \Lambda\cos\theta 2\pi R^2 \sin\theta d\theta = \frac{\pi R^2}{2\pi R^2}\Lambda\int_0^{\pi/2} 2\sin\theta\cos\theta d\theta = \frac{\Lambda}{2}\int_0^{\pi/2} \Lambda\sin 2\theta d\theta = \frac{\Lambda}{2} \qquad (6.2)$$

For Si 2p photoelectrons the perpendicular escape depth in silicon is 2.11 nm, but there are no good estimates for the escape depth through the oxide layer [175]. In [175] it is assumed that the maximum escape depth is equal to the inelastic mean free path of 3.80 nm. Using these values, an approximate depth of 1.9 nm in SiO_2 and 1.055 nm in silicon is probed by the XPS measurement [174]. The values above were used to calculate the average thickness of the SiO_2 layer on particles, using the equation:

$$y = \frac{P_{SiO_2} \times R_X}{(R_X + 1)}, \qquad (6.3)$$

where y is the thickness of the SiO_2 layer, P_{SiO2} is the photoelectron escape depth in SiO_2 and R_X is the ratio of the integrated intensities of the SiO_2 and silicon photoemission peaks. The maximum SiO_2 layer thickness measurable is of the order of 2 nm. Using the data from the Si 2p peaks of the XPS spectra and the equation above, the thickness of the SiO_2 shell of all silicon nanoparticles was estimated and is presented in figure 6.25.

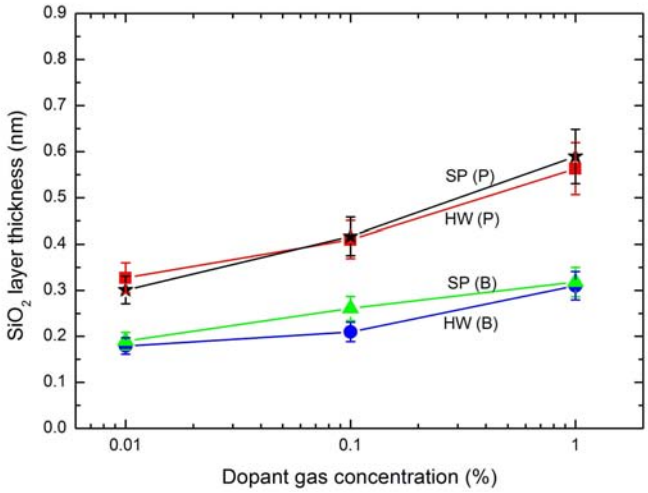

Figure 6.25 The estimated SiO_2 layer thickness of all particles at different dopant gas concentrations.

From figure 6.25 the tendency is clear. Irrespective of the pyrolysis process, the thickness of the SiO_2 shell for all nanoparticles produced in the presence of phosphine or diborane increases with an increase in dopant gas concentration. Furthermore, particles produced with phosphine have a thicker oxide layer than those produced with diborane. The SiO_2 shell thickness of nanoparticles produced by HWTCP at 5 mbar was also calculated. It is 0.82 nm for nanoparticles produced with 1% diborane and 1.1 nm for nanoparticles produced with 1% Phosphine. Additionally, the ratio of the Si^{1+} to the Si peak in the photoelectron spectrum points to a high percentage of Si^{1+} bonds, between 62% and 85 %, in nanoparticles produced by HWTCP at 5 mbar with 1% phosphine and 1% diborane concentrations respectively. In contrast, nanoparticles produced by HWTCP and SP at 40 and 80 mbar respectively, have a Si^{1+}/Si ratio between 8% and 15%, irrespective of dopant gas or concentration.

The region of the XPS spectrum around the boron 1s photoemission peak was investigated to determine boron concentrations in the surface region of particles produced with diborane. A detailed scan was executed on particles produced by HWTCP and SP with 0.01, 0.1 and 1 % diborane concentrations.

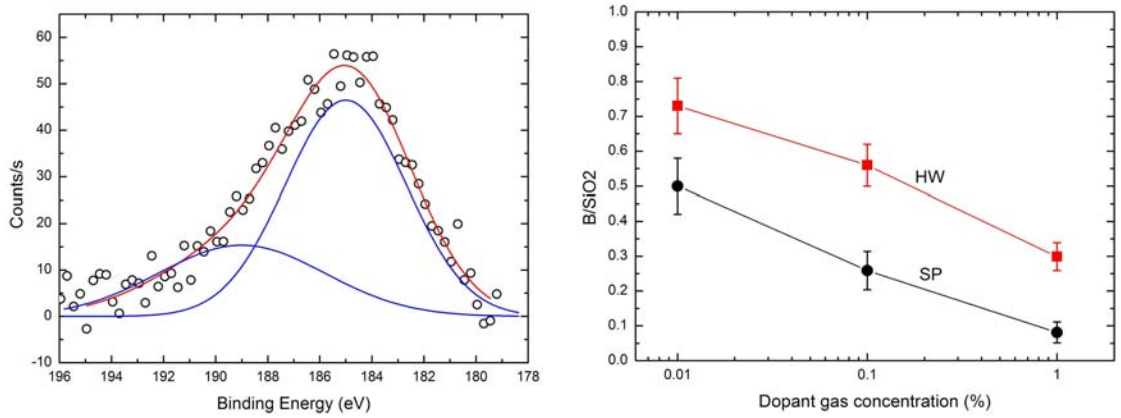

Figure 6.26 (a) Photoemission energy spectrum of the boron 1s peak of powder produced by HWTCP at 40 mbar, with 0.1% diborane. (b) Comparison of boron concentrations in all silicon nanopowders produced with diborane, as a ratio of SiO_2.

In figure 6.26 (a) the results of XPS of the boron 1s peak, of powder produced by HWTCP at 40 mbar, with 0.1% diborane is shown. The best fit was achieved by a superposition of two Gaussian peaks corresponding to the boron 1s peak at about 188 eV [176] and the overlapping silicon loss peak at about 184 eV. As indicated in figure 6.26 (b), if the intensity of the boron peak is expressed as a ratio to that of the silicon oxide peak, this decreases with an increase in diborane dopant concentration, for particles produced by HWTCP at 40 mbar and SP. For particles produced by HWTCP at 5 mbar with a 1% diborane concentration the ratio is 0.16, which is near to that of particles produced at 40 and 80 mbar with the highest diborane concentration.

The photoemission energy spectrum of the phosphorus 2p peak, of powder produced by HWTCP at 40 mbar, with 0.1% phosphine is shown in figure 6.27.

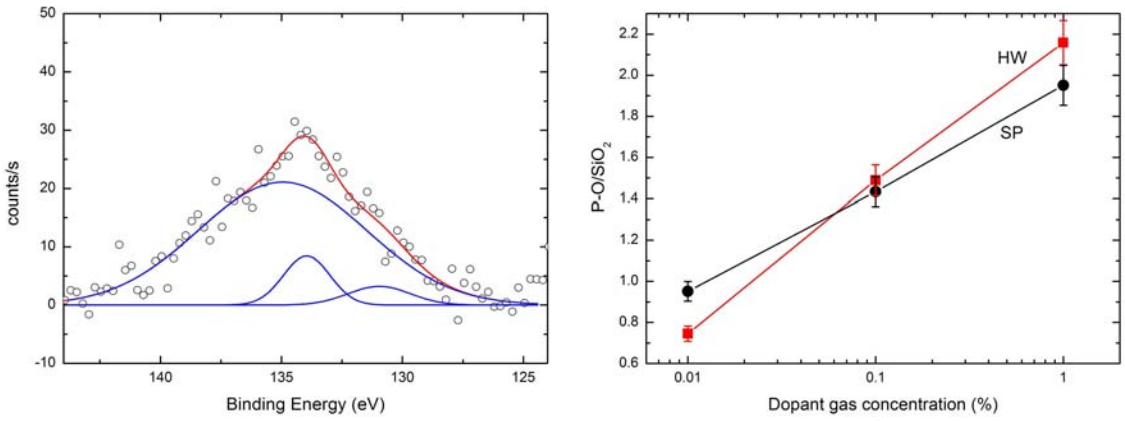

Figure 6.27 (a) Photoemission energy spectrum of the P 2p peak of powder produced by HWTCP at 40 mbar, with 0.1% phosphine. (b) Comparison of phosphorus concentrations in all silicon nanopowders produced with phosphine, as a ratio of SiO_2.

To analyse this region of the XPS spectrum, shown in figure 6.27 (a), the best least squares fit was achieved with 3 Gaussian peaks, corresponding to the Si loss peak at 134 eV, the P-O peak at 135 eV [177-179] and the combined P 2p peaks, at 131 eV [179-182]. Based on this peak fit method, the ratio of the intensities of the P-O bond to the SiO_2 was measured and calculated for all powders produced by HWTCP and SP at pressures of 40 and 80 mbar. A comparison of the ratios is presented in

figure 6.27 (b). From this figure it is evident that the number of phosphorus atoms in the outer 2-3 nm of the silicon nanoparticles increases with increasing phosphine concentration during production. Furthermore, no significant difference in the ratios is discernible between HWTCP and SP. The P-O/SiO_2 ratio for particles produced by HWTCP at 5 mbar with a 1% phosphine concentration was 0.1, which is near to that of particles produced at 40 and 80 mbar with the lowest dopant concentration.

6.3 Spectroscopic characterisation

6.3.1 Raman spectroscopy

The Raman spectra presented in figure 6.28 are of powders produced by HWTCP at 40 mbar and 0.01, 0.1 and 1 % phosphine concentrations. The single sharp peak of high intensity, centred at around 516 cm^{-1} originates from the transverse optical (TO2) vibrational mode of tetrahedral bonded silicon in the crystalline phase [183]. This peak may also contain contributions from tetrahedral S-O bonds in SiO_2, as found in coesite [184] produced at high temperature.

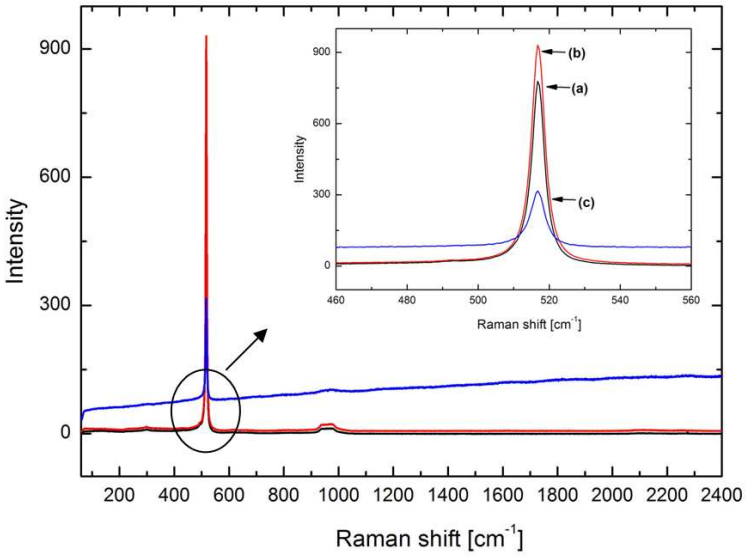

Figure 6.28 Raman spectra of silicon nanoparticles produced by HWTCP at 40 mbar at a phosphine concentration of (a) 0.01%, (b) 0.1% and (c) 1%.

However, as care was taken not to oxidise (burn) or anneal the powder during Raman measurements, the peak at 516 cm^{-1} in the spectra shown in figure 6.28 is attributed to crystalline silicon.

As a reference the Raman spectrum of a silicon wafer was collected. It has a sharp, narrow peak at 520 cm^{-1}. In comparison the TO2 peak of the Raman spectra of the silicon nanoparticles shown in figure 6.28 is broader and slightly red shifted (516 cm^{-1}), both of which can be attributed to particle size effects [7, 58, 185, 186]. Smaller peaks are also visible at about 300 and 960 cm^{-1}. The higher background in the Raman spectrum of nanopowder produced at 1%, observed in figure 6.28 is ascribed to the photoluminescent effect in that powder which has been linked to an oxide layer on silicon nanoparticles [79, 187]. The reduction in peak intensity as shown in the inset of figure 6.28 may be ascribed to an increased absorption of that powder due to differences in packing densities, particles size and agglomeration [188]. There is no significant difference between the FWHM of the TO2 peak of the Raman spectra of the powders shown in figure 6.28.

The Raman spectra of intrinsic powders, produced with an increase in production pressure, are shown in figure 6.29 (a).

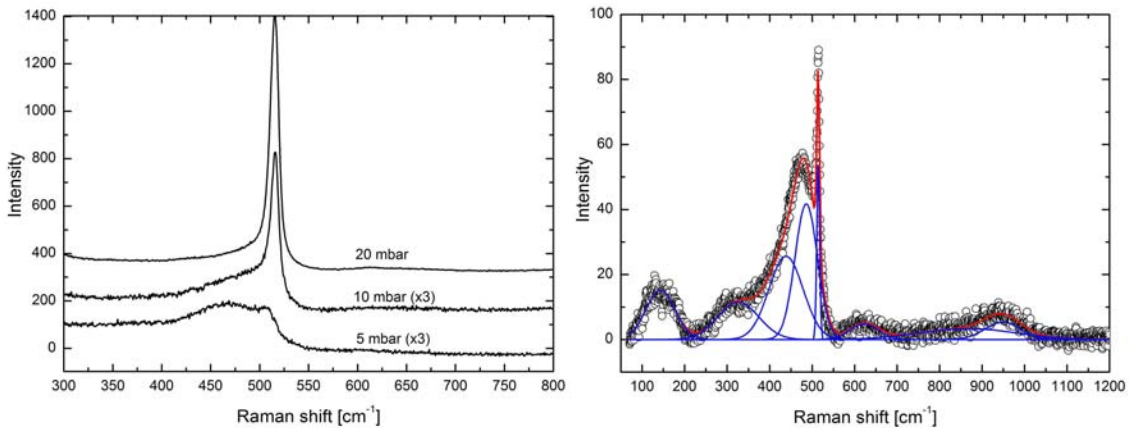

Figure 6.29 (a) Raman spectra of intrinsic nanoparticles produced by HWTCP at different pressures and (b) Raman spectra of silicon nanopowder produced by HWTCP at 5 mbar with a 0.1% phosphine concentration.

Staring with the Raman spectrum of the nanoparticles produced at a 5 mbar, the broad peak centred around 460 cm^{-1} is dominant. It constitutes two peaks, one at about 430 cm^{-1}, assigned to SiO_2 [184], and at about 480 cm^{-1}, generally assigned to amorphous silicon. The smaller peak on its shoulder, at around 510 cm^{-1} corresponding to the TO2 vibrational mode is assigned to the onset of crystallinity in the silicon, as per [183, 188, 189]. Continuing with figure 6.29 (a), as the synthesis pressure increases to 10 mbar the peak at 516 cm^{-1} starts to dominate while the peaks at 430 and 480 cm^{-1} are less pronounced. However at 20 mbar the 516 cm^{-1} peak dominates completely, with only a broad, low intensity peak remaining at 480 cm^{-1}, indicating a high degree of crystallinity in this sample.

The Raman spectrum shown in figure 6.29 (b) was collected from a powder produced by HWTCP at 5 mbar and 0.1% phosphine concentration. The model that produced the best least squares fit, incorporated 8 Gaussian peaks at 143, 328, 435, 480, 515, 620, 843 and 948cm^{-1}. These peaks correspond to the transverse acoustic (TA), longitudinal acoustic (LA), longitudinal optical (LO), first transverse optical (TO1), second transverse optical (TO2) as well as second order LA, LO and TO vibration modes of silicon respectively [189].

6.3.2 FTIR

FTIR was used to gain a general understanding of specific chemical bonds, including Si-O, Si-H and O-H, in the surface region of the silicon nanoparticles. The position of these and other peaks are illustrated in the spectra of silicon nanopowders produced by HWTCP at 5 mbar with 0.1% phosphine and 0.1% diborane concentrations respectively, as shown in figure 6.30.

The most prominent feature in these spectra is the strong absorption band between 1000 and 1200 cm^{-1}. As can be seen in both graphs, in figure 6.30, this region of the spectrum consist of two peaks, the first at about 1070 cm^{-1} and the second at about 1200 cm^{-1}. Both peaks fall in the region of the transverse-optical (TO) and longitudinal-optical (TO) stretching modes of the Si-O-Si bonds respectively [190], and have been attributed to surface oxides in porous silicon and silicon nanoparticles [83, 88, 191, 192].

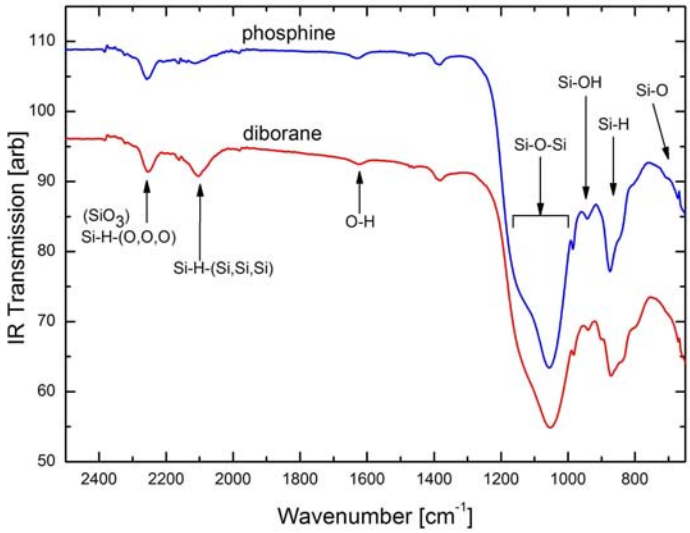

Figure 6.30 FTIR spectra of powder produced by HWTCP at 5 mbar with a 0.1% concentration of (a) phosphine and (b) diborane.

Furthermore the 1070 cm^{-1} peak is often attributed to Si-O stretching vibrations of sub-stoichiometric oxide (SiO_x (x<2)) and the 1200 cm^{-1} peak is attributed to stoichiometric Si-O vibrations (SiO_2) [150, 193, 194]. The ratio of the peaks may give an indication of the respective concentrations of these phases in the top ~1 nm of the silicon oxide layer, as has been shown experimentally [190] and supported by modelling [195]. It was shown that for a SiO_x (x<2) layer thicker than 0.5 nm the lower frequency peak (1070 cm^{-1}) dominates, while for even thinner layers of SiO_2 the peak intensity is similar [190].

Another feature in the spectra in figure 6.30 is the ratio of the peaks at 2250 cm^{-1} and 2100 cm^{-1}. The peak at 2250 cm^{-1} is assigned to H-Si-(O,O,O), an indication of hydrogen trapped in micro-voids [192], and so may be expected in the small and highly agglomerated particles. The absorption at 2250 cm^{-1} is also an indicator of increased oxygen bonds, as they correspond to Si-O-Si wag modes and surface SiO_3 vibrations [83, 96, 132]. The peak at 2100 cm^{-1} assigned to H-Si-(Si,Si,Si) is a sign of surface passivation by hydrogen atoms [196]. A further indication of the incorporation of hydrogen in the structure may be found in peaks at 800 cm^{-1} to 890 cm^{-1} corresponding to the Si-H_2 bending modes [132]. As the oxidation of the silicon nanoparticles dominates their electrical conductivity, the hydrogen vibration modes where not investigated in further detail.

In figure 6.31 the FTIR spectra of intrinsic silicon nanopowders, produced by HWTCP at different pressures is shown. A significant difference between the spectra is the change in the ratio of the two peaks at 1070 cm^{-1} and 1200 cm^{-1}. Starting from a dominant 1070 cm^{-1} peak from powders produced at 5 mbar, the increase in intensity of the 1200 cm^{-1} peak with increasing production pressure is apparent.

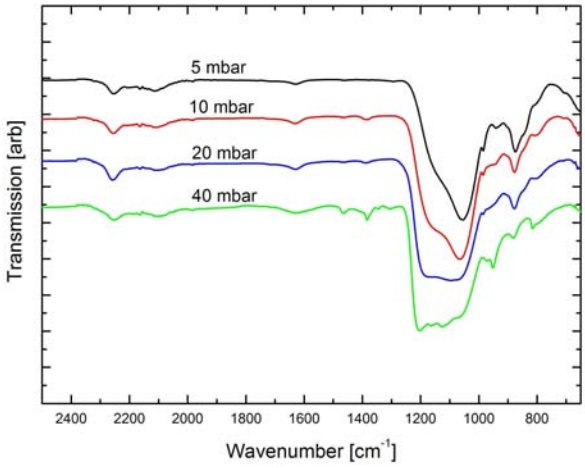

Figure 6.31 FTIR spectra of intrinsic silicon nanoparticles produced by HWTCP at pressures between 5 and 40 mbar.

In figure 6.32 the FTIR spectra of silicon nanopowders produced by (a) HWTCP at 40 mbar and different phosphine concentrations and by (b) SP at 80 mbar and different diborane concentrations are presented.

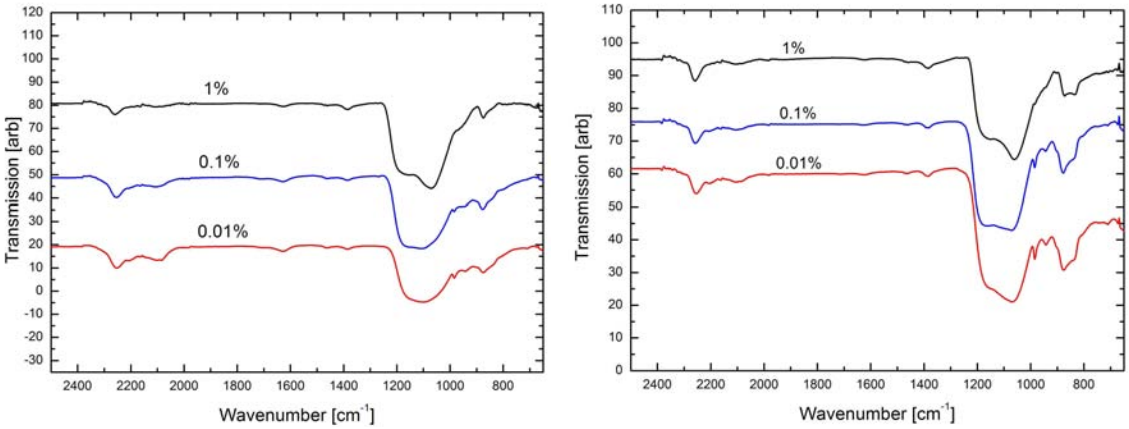

Figure 6.32 FTIR spectra of silicon nanopowder produced by (a) HWTCP at 40 mbar and different phosphine concentrations, and (b) silicon nanopowder produced by SP at 80 mbar and different diborane concentrations.

For silicon nanoparticles produced with either phosphine (figure 6.32 (a)) or diborane (figure 6.32 (b)), the 2100 cm^{-1} peak, compared to the 2250 cm^{-1} peak, decreases with an increase in dopant concentrations, indicating a higher level of hydrogen [79] in the powders produced at lower dopant concentrations and a higher level of oxides in the powder produced at higher dopant concentrations. Another feature in both spectra given in figure 6.32 (a) and (b), is the similar intensity of the SiO_2 and SiO_x ($0<x<2$) peaks at 1200 cm^{-1} and 1070 cm^{-1} for all dopant concentrations.

6.4 Electrical characterisation

The electrical properties of powders were investigated by using the technique described in chapter 5, which has been reported for measuring the resistivity of conducting powders [164-166]. A current is passed through a known volume of powder at a known compression (density) while measuring the change in potential as a V-I curve.

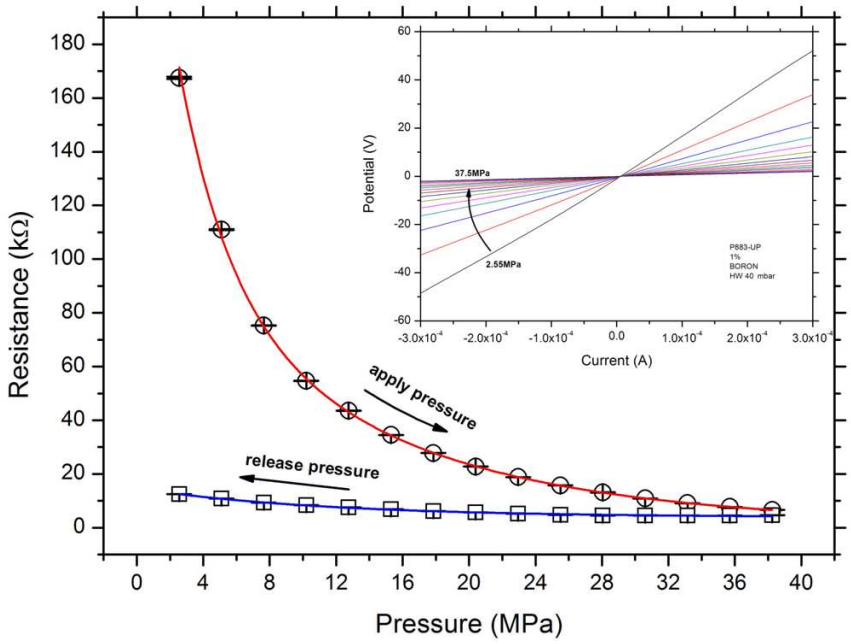

Figure 6.33 Decrease in the resistance of silicon nanopowder upon the application of pressure (compression), for a powder produced by HWTCP at 40 mbar and 1% diborane gas concentration.

The effect of compression on the resistance of a silicon nanopowder produced by HWTCP at 40 mbar is illustrated in figure 6.33. As the compression increases, the resistance decreases, partially due to an increase in the number of, and contact area between particles. The inset shows the V-I curve of each compression step of 2.55 MPa for the same powder.

The resistance increases slightly upon release of the pressure, indicating complete compaction and elastic compression of the powder. For both compression and decompression cycles the change in resistance can be described by an exponential decay function (solid lines).

The V-I curves shown in figure 6.34 originate from compression experiments of a powder produced by HWTCP at 40 mbar with 1% phosphine.

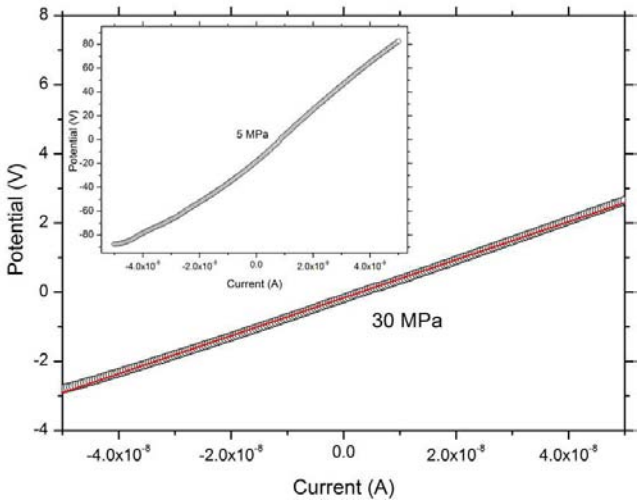

Figure 6.34 V-I curves of powder produced by HWTCP at 40 mbar, with a 1% phosphine concentration. Non-linear behaviour is evident at lower compression (inset).

While the main curve in figure 6.34, collected at a pressure of 30 MPa approaches ohmic behaviour shown by its approach to linearity, the inset curve collected at a lower compression (5 MPa) exhibits a shallow s-curve which indicates a diode behaviour, most likely caused by a Shottkey contact between the steel pistons and the powder. In comparison, the V-I curves of compression experiments of a powder produced by HWTCP at 40 mbar with a 1% diborane concentration (figure 6.35), do not exhibit such a strong s-shape as in figure 6.34 at lower pressures, which is an indication of ohmic behaviour.

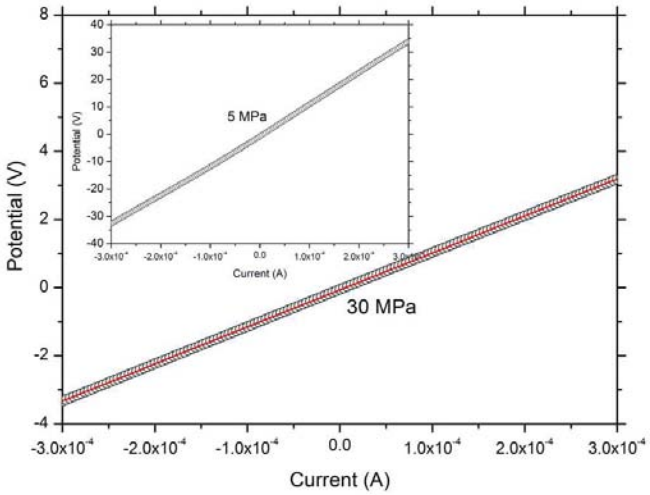

Figure 6.35 V-I curves of powder produced by HWTCP at 40 mbar, with a 1% diborane concentration. The powder shows ohmic behaviour at high and low (inset) compression rates.

For all silicon nanopowders, irrespective of the production process, the V-I curves collected from the powders under high compression are considerably more linear than those collected at low compression. Furthermore for powders produced with phosphine the curvature is stronger than for those produced with diborane.

The non-ohmic resistance behaviour found in the V-I measurements may be described by adopting an equivalent circuit approach [164], shown in figure 6.36. It comprises a capacitor (C) and resistor (R_P) in parallel, in series with a resistor (R_S). The current supply terminals (V_M and V_0) represent the plungers in the measurement apparatus.

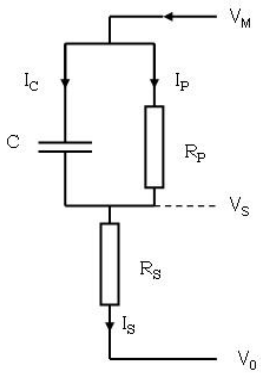

Figure 6.36 Equivalent circuit of compressed silicon nanopowder, comprising a capacitor (C) and resistor (R_P) in parallel, in series with a resistor (R_S).

V-I curves of all powders were collected over a wide range of compression (2.55 to 35.7 MPa), with a short current sweep dwell time of 0.1 s to enhance capacitive effects. However for the purpose of comparing resistivities of the silicon nano-powders, the non-ohmic region of the powder was avoided by calculating the resistivities based on the V-I curves in the ohmic region and under a compression of 20 MPa. In figure 6.37 the resistivity of all powders produced by HWTCP at 40 mbar and SP at 80 mbar, at different dopant concentrations, is shown.

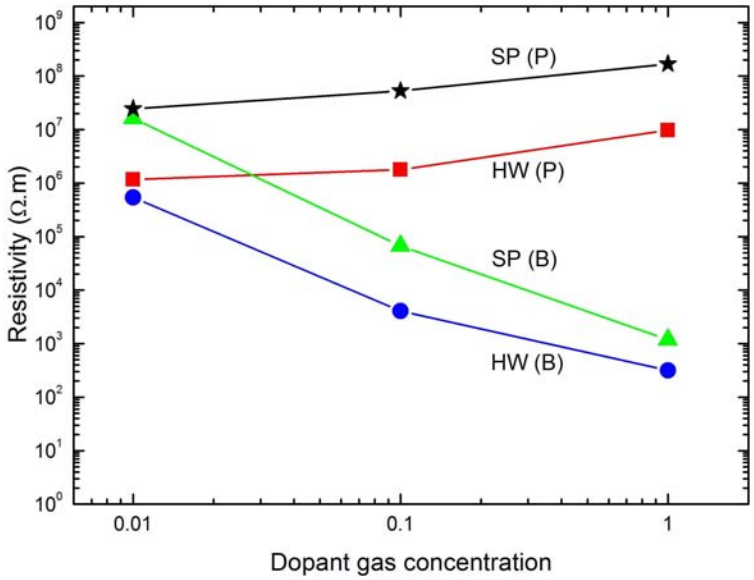

Figure 6.37 A comparison of the resistivity values of all powders produced by HWTCP at 40 mbar and SP with varying concentrations of phosphine and diborane.

The first feature in figure 6.37 is that powders produced by HWTCP and SP with diborane (marked as HW (B) and SP (B)), exhibit a decrease in resistivity with an increase in diborane concentration. In contrast, powders produced by HWTCP and SP with phosphine (marked as HW (P) and SP (P)), show an increase in resistivity with an increase in phosphine concentration. Furthermore all powders produced by SP show a higher resistivity compared to powders produced by HWTCP, at the equivalent dopant concentrations. The resistivity of the intrinsic silicon nanoparticles produced by HWTCP and SP at 40 and 80 mbar respectively was measured in the same way. The intrinsic HWCVD particles have a resistivity of 1.43×10^7 Ω.m and the SP particles 1.12×10^7 Ω.m.

The resistivity of powders produced by HWTCP at 5 mbar with diborane and phosphine dopants is shown in figure 6.38.

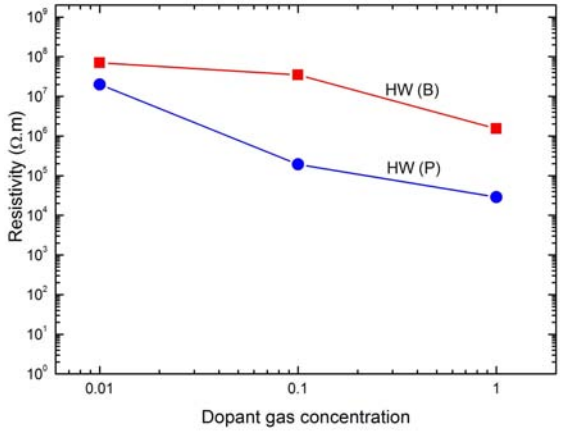

Figure 6.38 A comparison of the resistivity values of all powders produced by HWTCP and 5 mbar, with varying concentrations of phosphine and diborane.

Compared to powders produced by HWTCP at 40 mbar and by SP, powders produced by HWTCP at 5 mbar have a higher resistivity, for the equivalent dopant concentrations. However, as apparent in figure 6.38, powders produced at 5 mbar show a decrease in resistivity with an increase in dopant gas concentration of both diborane and phosphine. The higher resistivity of silicon nanoparticles produced at lower pressure is also illustrated in the resistance of intrinsic powders produced by HWTCP at different synthesis pressures, as shown in figure 6.39.

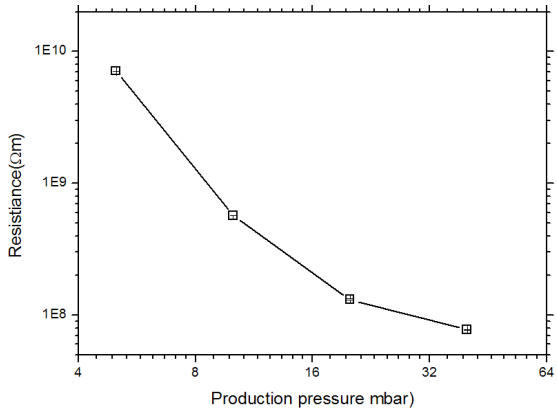

Figure 6.39 The resistance of intrinsic silicon nanopowders produced by HWTCP, compressed to the same density.

As evidenced by the negative slope in the graph shown in figure 6.39, a decrease in resistance is observed with an increase in synthesis pressure.

7. DISCUSSION

For the first time, silicon nanoparticles doped with electrically active boron and phosphor, have been produced by hot wire thermal catalytic pyrolysis (HWTCP) and spark pyrolysis (SP). The successful doping is evident from the decrease in resistivity (figure 6.37) of all silicon nanoparticles produced by HWTCP (HW(B)) and SP (SP(B)) at 40 and 80 mbar, with increasing diborane concentrations, as well as in powders produced by HWTCP with diborane and phosphine at 5mbar (figure 6.38). Such decrease in resistivity is expected in silicon, with an increase in dopant atom concentrations [97, 99, 197]. The successful doping makes these silicon nanoparticles suitable for their intended electronic application.

As evident in figure 6.37 the resistivity of silicon nanoparticles produced by HWTCP (HW(P)) and SP (SP(P)) with phosphine, at 40 and 80 mbar, increases with an increase in phosphine concentration. As determined by EDX, this increase in resistivity cannot be ascribed to the lack of phosphine. As shown in figure 6.21, an increase in phosphorus concentration is detected for silicon nanoparticles produced with increasing phosphine concentrations. However, as observed in the oxygen content determined by EDX (figure 6.18), powders produced with phosphine generally have higher oxygen content than those produced with diborane. Furthermore, from TEM images and XPS, it was established that the oxygen resides in an amorphous shell around the particles. The assumption is thus made that the lower conductivity of silicon nanoparticles produced with increasing phosphine concentration is related to the presence of an oxide layer, which is thicker in particles produced with phosphine than for those produced with diborane.

Using the method described in chapter 6, the thickness of the SiO_2 layer on the silicon nanoparticles was estimated by XPS. As can be seen in figure 7.1 the thickness of the oxide layer increases with an increase in dopant gas concentration. A similar increase of the total oxygen content in the powders, with increased dopant gas concentrations, has been measured by EDX (figure 6.18). Of the stable sub-oxides (figure 6.22), the Si^{1+} state, corresponding to an oxygen atom bridging two

surface silicon atoms, dominates. The most stable of the silicon oxygen configurations is however the Si^{2+} state, corresponding to a back-bonded oxygen configuration. There is also a broad shallow peak due to the Si^{3+} sub-oxide. Taken together, these are an indication that in the silicon nanoparticles, meta-stable silicon sub-oxides are reduced and prevent the formation of higher oxides.

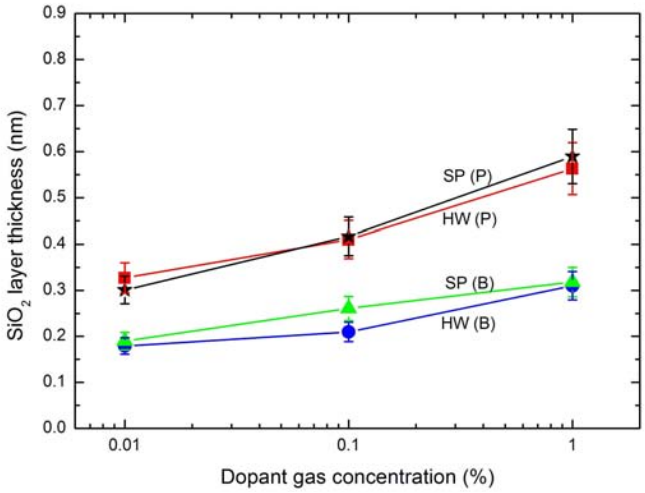

Figure 7.1 The estimated SiO_2 layer thickness of all silicon nanoparticles at the different dopant gas concentrations.

Furthermore, as observed in figure 7.1, the estimated SiO_2 layer thickness on silicon nanoparticles produced with phosphine is twice that of particles produced with diborane at equivalent concentrations. Indeed, as seen from the TEM images, at an estimated thickness of only 2 to 3 Angstroms it may not be appropriate to consider this as a layer of stoichiometric oxide for the boron doped nanoparticles. Based on the state of the vacuum during production, as highlighted in chapter 4, care was taken to minimise the oxygen present in the camber, and thus the oxygen is attributed to native oxides which form when the silicon nanoparticles are exposed to air. The same has been suggested for silicon nanoparticles with varying oxide thickness between 0.5 and 5 nm [7, 9, 10, 22, 23].

A comparison of the integrated intensities of the boron 1s and phosphorus 2p peaks of the silicon nanoparticles is given in figure 7.2 (a) and (b) respectively. The particles were produced by HWTCP at 40 mbar and SP.

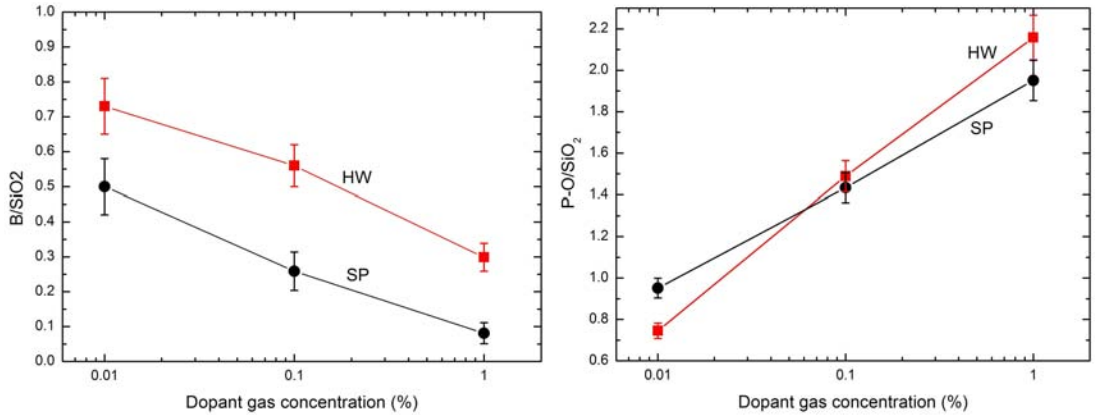

(a) (b)

Figure 7.2 (a) Comparison of boron concentrations in all silicon nanopowders produced with diborane, as a ratio of SiO_2. (b) Comparison of phosphorus concentrations in all silicon nanopowders produced with phosphine, as a ratio of SiO_2.

The decrease in boron concentration (figure 7.2 (a)) with an increase in diborane concentration corresponds to an increase in surface oxide (figure 7.1). This is a clear indication that the boron atoms are not primarily located at the surface. In contrast, in figure 7.2 (b), an increase in phosphorus is observed with an increase in phosphine concentration and again corresponds to an increase in oxide layer thickness. The phosphorus atoms are thus primarily trapped in the oxide or at the oxide/silicon interface [12]. Here they are electrically inactive, and so do not contribute to the charge transport.

A further observation from the XPS spectra in figure 6.23 (a), is that oxides increase slightly with increasing diborane concentrations in powders produced with diborane. However, in powder produced with phosphine (figure 6.23 (b)), the ratio of SiO_2 to the silicon sub-oxides increases drastically at higher phosphine concentrations. This suggests that in silicon nanoparticles produced with phosphine, meta-stable sub-oxides become fully oxidised at higher phosphine concentrations.

The Cabrera-Mott mechanism [198] offers a way of interpreting the thicker oxide layer observed on particles produced with phosphine. A virgin silicon surface on a silicon nanoparticle will rapidly form a thin native oxide layer when exposed to air.

Electrons may now tunnel through the thin oxide layer to the surface. Some oxygen atoms adsorbed on the surface will be ionized and acquire a negative charge, to form an electric potential V_{OL} across the oxide layer. Assisted by V_{OL}, oxygen ions diffuse through the silicon oxide layer to oxidise the silicon underneath [12]. From the model it can be deducted that in the case of phosphorous doped silicon nanoparticles there is a higher concentration of free electrons, induced by the phosphorus. This results in an increase in V_{OL}, which boosts the transport of the oxygen ions through the silicon oxide layer, resulting in a more efficient oxidation. In boron doping, the low electron concentration reduces V_{OL}, and thus boron doped nanoparticles are less oxidised [12].

Another observation from figure 6.37 (a) is the higher resistivity of all silicon nanopowders produced by SP compared to those produced by HWTCP at the same dopant gas concentrations. From the TEM investigation it is apparent that all particles produced by HWTCP at 40 mbar are faceted while those produced by SP are spherical. It is probable that this difference in shape accounts for differences in resistivity between particles produced by HWTCP and SP.

In a compacted nanopowder, charge carriers have to follow a path, from one electrode, to the other, through the particles and through inter-particle boundaries. The electrical conductivity of the compressed powder will be directly proportional to the filled cross-sectional area [199] or the packing density (porosity) of the powder, which is directly proportional to the sum of the contact areas of the particles in that cross section. It is also affected by the size and shape of the particles in the powder [200].

To determine whether the shape of the silicon nanoparticles may account for the differences in resistivity between spherical and faceted shapes, a simple first order approach is to estimate the contact area between two particles of the same type, assuming equal volume. To first order the contact area between two incompressible spheres is essentially zero. For real particles the compression, however small, needs to be taken into consideration. For two spherical silicon nanoparticles, pressed together, the area of contact will depend on the pressure. For the calculations, only the lateral conduction path through particles will be taken into account. From experiments conducted on the compression of individual spherical silicon

nanoparticles [201], a force of 2 μN (440 MPa) is required to compress a 38 nm diameter sphere by 1 nm.

For the resistivity measurements presented in figure 6.33 the maximum pressure used to compress the silicon nanoparticles produced here, was 40 MPa. This is ten times less than in the single particle experiments reported in [201]. Assuming elastic deformation in the silicon nanoparticles [202], the compression distance δ on 38 nm diameter particles under 40 MPa compression will thus be 0.1 nm.

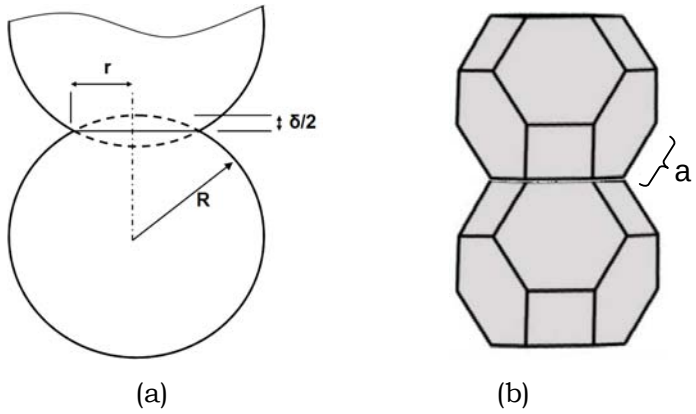

Figure 7.3 (a) Diagram of contact area between spherical particles. (b) Stacked truncated octahedron with the edge length *a*.

As shown in figure 7.3 (a) the radius *r* of the contact area between the two compressed spherical silicon nanoparticles of radius *R*, can now be calculated by [201]:

$$r = \sqrt{\delta R - \frac{\delta^2}{4}} . \qquad (7.1)$$

The radius of the contact area between two spherical silicon nanoparticles of 38 nm diameter, under 40 MPa compression, is thus 2 nm and the contact area is 12 nm^2.

To determine the contact area of two truncated octahedra, the same volume as the spherical silicon nanoparticles discussed above, is assumed. The diameter of this truncated octahedron, $D = a\sqrt{10}$, will be 43 nm and the edge length *a*, indicated in

figure 7.3(b) is 13.6 nm. The surface areas of the square and hexagonal faces of this octahedron are thus 185 nm^2 and 480 nm^2 respectively. These are more than ten times larger than that of the spherical particles. The higher resistivity of silicon nanoparticles produced by SP compared to those produced by HWTCP can therefore be attributed to the difference in the shape of the silicon nanoparticles produced by each process.

To explain the difference in shape between silicon nanoparticles produced by HWTCP and SP, the difference in the processes has to be investigated. In figure 7.4 it is graphically shown how in both production processes, particles start to form in the supersaturated vapour, by homogeneous nucleation, to form liquid silicon droplets [7, 203]. The droplets are expected to be spherical, to maintain minimum surface energy. As the pressure in both processes is high, sufficient precursor species collide with the nucleating particle, resulting in accelerated growth. The difference in the shape of particles produced by SP and HWTCP originates from the difference in the rate of cooling, between the processes.

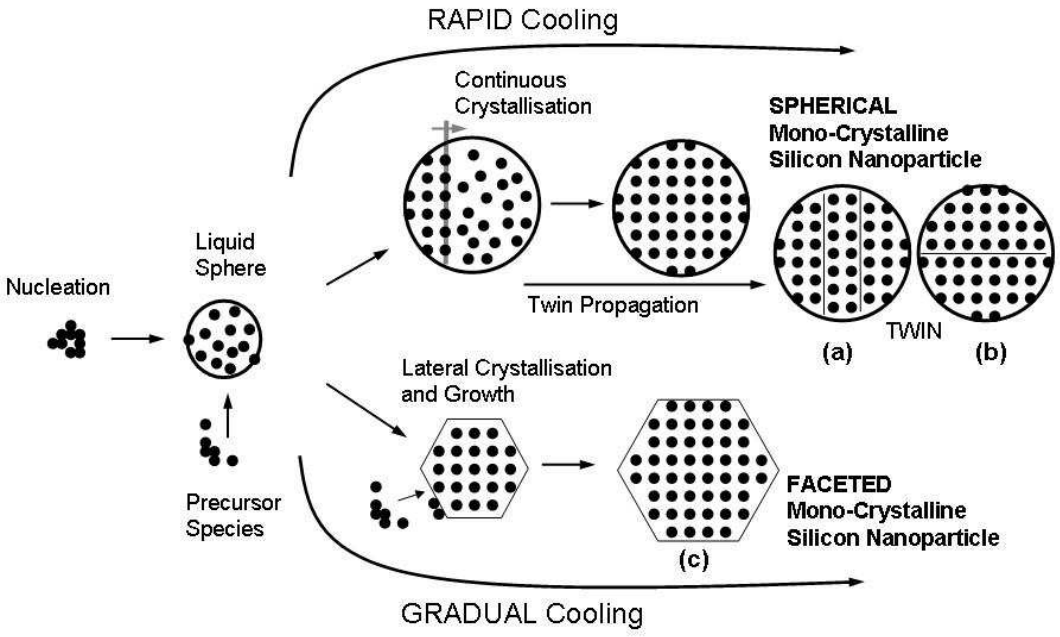

Figure 7.4 Silicon nanoparticle growth process for spherical and faceted particles. In continuous crystallisation twins may start with a twin nucleation site and propagate vertically along the crystallisation front.

The high temperature spark, which lasts for approximately 100 ns, creates the conditions for rapid pyrolysis and rapid cooling. Crystallisation of the spherical droplets start from a crystal nucleation site on its edge and propagates through the crystal as a crystallisation front [203] at the solid/liquid interface. The process results in spherical single crystal silicon nanoparticles. Similar results have been reported for laser pyrolysis [7, 204] and plasma synthesis with accelerated cooling [203, 205]. However, as observed in the TEM images of particles produced by SP, shown in the TEM image in figure 7.5, the continuous rapid crystallisation process may result in twinning, as marked by the arrows.

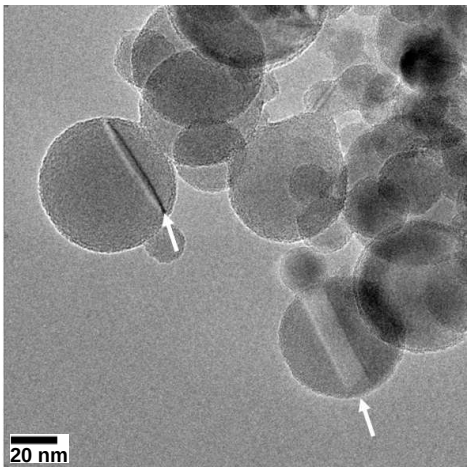

Figure 7.5 An example of twinning is visible in the TEM images of intrinsic silicon nanoparticles produced by SP at 80 mbar.

Two mechanisms may be responsible for twinning. Firstly, twinning may originate along the crystallisation front as shown in figure 7.4 (a), where it arises from tensile stresses. These stresses are caused by volume contractions during crystallisation [206], which are relieved by partial dislocations passing through the lattice, creating stacking faults [95]. Secondly a twin may originate at the nuclear crystallisation site, to propagate along the crystallisation front, to form the twin perpendicular to it (figure 7.4 (b)). For fcc crystals, such as silicon nanoparticles, twinning is expected along the $\{111\}$ planes [203, 207].

Continuing with figure 7.4, in contrast to spark pyrolysis, which is a short, cyclic process, the HWTCP process has a continuous heat source, resulting in continuous pyrolysis and a moderate temperature gradient around the filament. The low

number of particles with twinning, in silicon nanoparticles produced by HWTCP at 40 mbar, as observed by TEM, indicates that the HWTCP process allows lattice mismatches to be self-corrected by rearranging atoms in the growth process. The liquid silicon droplets gradually cool as they move away from the filament. There is sufficient time and energy for atoms to find energy favourable growth sites. The crystal planes of the nanocrystals therefore start to grow laterally [22] to form faceted particles [13], as shown in figure 7.4 (c). Furthermore, species in the vapour have enough energy to find an energy favourable sight and contribute to continued particle growth. Given ideal conditions an individual particle takes the shape with the lowest total surface energy, a truncated octahedron [168, 208-211] (See appendix B). However, the temperature gradient around the filament creates differences in cooling gradients, which is responsible for the different states of faceted shapes in particles produced by HWTCP as shown in figure 6.4 (a).

The shape of the silicon nanoparticles produced by HWTCP and SP is therefore directly linked to the cooling rate and the synthesis temperature. At a high synthesis temperature and rapid cooling such as in SP, crystalline spherical particles are formed. However at moderate synthesis temperatures and cooling rates, faceted particles are formed.

The particle size histograms shown in figure 6.5 indicate that the average diameter of 22 nm of silicon nanoparticles produced by SP is smaller than that of particles produced by HWTCP, which is approximately 34 nm. This trend is supported by the crystallite size calculations, using the Scherrer method on XRD patterns (figure 6.13). The crystallite sizes of nanoparticles produced by HWTCP at 40 mbar are generally 20-40% larger than those produced by SP at 80 mbar, for the same dopant gas and concentration. The difference in size is attributed to the residence time of the growing particle in the high temperature growth zone. In SP a small volume of vapour is heated for a short period. There is insufficient time for particles to grow. In HWTCP there is a large heat zone, and particles have a long residence time to grow in size. Furthermore, compared to SP, a higher percentage of particles, produced by HWTCP (figure 6.5 (c)) are larger than twice the average size.

Particles produced at a low pressure are smallest and, as observed by TEM (figure 6.3) surrounded by a thicker amorphous shell. This is supported by the broad

peaks at 430 and 480 cm^{-1} in the Raman spectrum (figure 6.28) as well as the well expressed 1070 cm^{-1} FTIR peak which corresponds to Si-O vibrations in amorphous SiO_x (x<2). As the production pressure is increased the particle diameter increases. This increase can be explained by a pressure induced increase in collisions between species and the nucleation particle in the reactor, leading to higher growth rates. Furthermore, as the size increases, the particles become more crystalline (figure 6.12) and thus oxidise less, resulting in a thinner oxide layer and a decrease in resistance in these powders. The decrease in the oxide layer thickness is further supported by the increase in the intensity of the 1200 cm^{-1} FTIR peak relative to the 1070 cm^{-1} peak, as shown in figure 6.31. In all FTIR spectra of powders produced by HWTCP and SP at all dopant concentrations (figure 6.32), these two FTIR peaks feature prominently, indicating that the silicon oxide layer is less than 0.5 nm thick [190].

Finally, the particle size has an additional effect on the measured conductivity. The total contact area of the nanoparticles in a cross section will be equal for all sizes of particles. However, the number of inter-particle interfaces will increase inversely proportionally to the decrease in diameter. Given that the oxide layers are equally thick (figure 6.25), the 20% smaller particles produced by SP will have 25% more interfaces than particles produced by HWTCP for the same volume and compaction of particles. Thus some of the higher resistivity in silicon nanoparticles produced by SP may be attributed to their smaller average size.

8. CONCLUSION

The goal of producing doped silicon nanoparticles with clean surfaces, and which are suitable for electronic applications, has been achieved. For the first time, silicon nanoparticles doped with electrically active boron and phosphorus, have been produced by the known bottom-up process of hot wire thermal catalytic pyrolysis (HWTCP) and by the newly introduced spark pyrolysis (SP) process. The latter was developed as part of this thesis.

Both processes predominantly produce monocrystalline silicon nanoparticles, which are spherical in SP and faceted in HWTCP, and have an average diameter of 22 nm and 34 nm respectively. HWTCP at low pressures produces highly aggregated nanoparticles with a diameter of approximately 10 nm, which are surrounded by an amorphous network.

The shape of the nanoparticles is governed by the synthesis temperature and cooling rate of the processes. In SP, the short-lived, high temperature and cyclic spark process creates the conditions for rapid pyrolysis and rapid cooling. Continuous crystallisation of the spherical liquid nucleation particle results in spherical single crystal silicon nanoparticles with possible twinning resulting from defects along the crystallisation front. However in the HWTCP process, the continuous heat source results in uninterrupted pyrolysis and a moderate cooling rate. The crystal planes of the nucleating particle can grow laterally in such a way that surface energy is reduced, thus taking on a faceted shape, of which the truncated octahedron has the lowest surface energy. Furthermore due to the longer synthesis time, particle diameters are on average larger than those of particles produced by SP. The difference in shape of particles produced by HWTCP and SP has an effect on the resistivity of compacted powders. Truncated octahedra have about ten times more inter-particle contact area than spherical particles for the same particle volume. The greater contact area accounts for the lower resistivity in the compacted faceted particles produced by HWTCP compared to the spherical particles produced by SP.

The production pressure also influences the particle size. Intrinsic particles produced by HWTCP steadily increase in diameter from an average of 10 nm when produced at 5 mbar to a diameter of 34 nm at 40 mbar. This increase in size results from an increase in collisions between species and the nucleating particle in the reactor at higher pressure, leading to higher growth rates.

The successful doping is evident from the decrease in resistivity of silicon nanoparticles produced by HWTCP at 40 mbar and SP at 80 mbar. The same does not apply to silicon nanoparticles produced with phosphine at high gas pressures, where the resistivity increases with increasing phosphine concentrations. This effect is attributed to the increase of the oxide surface layer thickness from about 0.3 nm to 0.6 nm on these particles. Furthermore, the phosphor atoms are not incorporated in the silicon but rather in the oxide layer where they are electrically inactive. In contrast all particles produced by HWTCP at 5 mbar with either phosphine and diborane show successful doping behaviour. Their resistivity decreases with an increase in dopant gas concentrations.

In conclusion, this thesis has shown that a high vacuum system operated at low base pressures can produce electrically active silicon nanoparticles with oxygen passivated surfaces. Both processes offer a fairly simple route to doped crystalline silicon nanoparticle synthesis.

REFERENCES

[1] Britton, D.T. and M. Härting, *Printed Nanoparticulate Composites for Silicon Thick Film Electronics.* Pure and Applied Chemistry, 2006. 78: p. 1723.

[2] Härting, M., J. Zhang, D.R. Gamota, and D.T. Britton, *Fully printed silicon field effect transistors.* Applied Physics Letters, 2009. 94(19): p. 193509-3.

[3] Gupta, A. and H. Wiggers, *Surface chemistry and photoluminescence property of functionalized silicon nanoparticles.* Physica E: Low-dimensional Systems and Nanostructures, 2009. 41(6): p. 1010-1014.

[4] Harwell, D.E., J.C. Croney, W.J. Qin, J.T. Thornton, J.H. Day, E.K. Hajime, and D.M. Jameson, *Effects of surface passivation on silicon nanoparticle photoluminescence.* Chemistry Letters, 2003. 32(12): p. 1194-1195.

[5] Makimura, T., T. Mizuta, and K. Murakami, *Laser ablation synthesis of hydrogenated silicon nanoparticles with green photoluminescence in the gas phase.* Japanese Journal of Applied Physics Part 2-Letters, 2002. 41(2A): p. L144-L146.

[6] Ledoux, G., O. Guillois, C. Reynaud, F. Huisken, B. Kohn, and V. Paillard, *Photoluminescence of silicon nanocrystallites: an astrophysical application.* Materials Science and Engineering B, 2000. 69-70: p. 350-354.

[7] Huisken, F., H. Hofmeister, B. Kohn, M.A. Laguna, and V. Paillard, *Laser production and deposition of light-emitting silicon nanoparticles.* Applied Surface Science, 2000. 154-155: p. 305-313.

[8] Wang, G., S.-T. Yau, K. Mantey, and M.H. Nayfeh, *Fluorescent Si nanoparticle-based electrode for sensing biomedical substances.* Optics Communications, 2008. 281(7): p. 1765-1770.

[9] Roura, P., J. Farjas, A. Pinyol, and E. Bertran, *The crystallization temperature of silicon nanoparticles.* Nanotechnology, 2007. 18(17): p. 175705.

[10] Lacour, F., O. Guillois, X. Portier, H. Perez, N. Herlin, and C. Reynaud, *Laser pyrolysis synthesis and characterization of luminescent silicon nanocrystals.* Physica E: Low-dimensional Systems and Nanostructures, 2007. 38(1-2): p. 11-15.

[11] Britton, D.T., E.A. Odo, G.G. Gonfa, E.O. Jonah, and M. Härting, *Size distribution and surface characteristics of silicon nanoparticles.* Journal of Applied Crystallography, 2009. 42(3): p. 448-456.

[12] Pi, X.D., R. Gresback, R.W. Liptak, S.A. Campbell, and U. Kortshagen, *Doping efficiency, dopant location, and oxidation of Si nanocrystals.* Applied Physics Letters, 2008. 92(12): p. 123102-3.

[13] Kortshagen, U.R., L. Mangolini, and A. Babat, *Plasma synthesis of semiconductor nanocrystals for nanoelectronics and luminescence applications.* Journal of Nanoparticle Research, 2007. 9: p. 39-52.

[14] Ostraat, M.L., M. Brongersma, H.A. Atwater, and R.C. Flagan, *Nanoengineered silicon/silicon dioxide nanoparticle heterostructures.* Solid State Sciences, 2005. 7(7): p. 882-890.

[15] Kruis, F.E., H. Fissan, and A. Peled, *Synthesis of nanoparticles in the gas phase for electronic, optical and magnetic applications--a review.* Journal of Aerosol Science, 1998. 29(5-6): p. 511-535.

[16] Swihart, M.T., *Vapor-phase synthesis of nanoparticles.* Current Opinion in Colloid & Interface Science, 2003. 8(1): p. 127-133.

[17] Scriba, M.R., C. Arendse, M. Härting, and D.T. Britton, *Hot-wire synthesis of Si nanoparticles.* Thin Solid Films, 2008. 516(5): p. 844-846.

[18] Scriba, M.R., D.T. Britton, C. Arendse, M.J. van Staden, and M. Härting, *Composition and crystallinity of silicon nanoparticles synthesised by hot wire thermal catalytic pyrolysis at different pressures.* Thin Solid Films, 2009. 517(12): p. 3484-3487.

[19] Kumar, P. and B. Schroeder, *Electrical properties/Doping efficiency of doped microcrystalline silicon layers prepared by hot-wire chemical vapor deposition.* Thin Solid Films, 2008. 516(5): p. 580-583.

[20] Guillet, J., C. Niikura, J.E. Bourée, J.P. Kleider, C. Longeaud, and R. Brüggemann, *Microcrystalline silicon deposited by the hot-wire CVD technique.* Materials Science and Engineering B, 2000. 69-70: p. 284-288.

[21] Brüggemann, R., A. Hierzenberger, P. Reinig, M. Rojahn, M.B. Schubert, S. Schweizer, H.N. Wanka, and I. Zrinscak, *Electronic and optical properties of hot-wire-deposited microcrystalline silicon.* Journal of Non-Crystalline Solids, 1998. 227-230(Part 2): p. 982.

[22] Babat, A., C. Anderson, C.R. Perry, C.B. Carter, S.A. Campbell, and U. Kortshagen, *Plasma synthesis of single-crystal silicon nanoparticles for novel electronic device applications.* Plasma Phys. Control. Fusion, 2004. 46: p. B97-B109.

[23] Hofmeister, H. and P. Kodderitzsch, *Nonosized Silicon Particles by inert gas arc evaporation.* Nanostructured Materials, 1999. 12: p. 203-206.

[24] Hummel, R.E., *Electronic Properties of Materials*. 1985: Springer Verlag.

[25] Sze, S.M., *Semiconductor Devices-Physics and Technology*. 1985: Bell Telephone Laboratories Inc.

[26] Neamen, D.A., *Semiconductor Physics and Devices*. 2003: McGraw-Hill.

[27] Mishra, U.K. and J. Singh, *Semiconductor Device Physics and Design*. 2008: Springer.

[28] Kittel, C., *Introduction to Solid State Physics*. 1 ed. 2005: John Wiley & Sons, Inc.

[29] Singh, J. and K. Shimakawa, *Advances in Amorphous Semiconductors*. 2003: Taylor & Francis.

[30] Kumar, V., *Nanosilicon*. 2007: Elsivier.

[31] Rockett, A., *The Materials Science of Semiconductors*. 2008: Springer Science+Business Media, LLC.

[32] van Zeghbroeck, B., *Principles of Semiconductor Devices and Heterojunctions*. 2009: Prentice Hall.

[33] Colinge, J.P. and C.A. Colinge, *Physics of Semiconductor Devices*. 2002: Kluwer Academic Publishers.

[34] Sze, S.M. and K.K. Ng, *Physics of Semiconductor Devices*. 2007: John Wiley & Sons,.

[35] Schmid, G., *Nanoparticles*. Schmid, G. ed. 2004: Wiley-VCH.

[36] Stutzmann, M., *Hydrogen passivation of boron acceptors in silicon: Raman studies.* Physical Review B, 1987. 35(11): p. 5921.

[37] Rowsell, B.D. and J.G.C. Veinot, *Reductive thermolysis of a heterocyclic precursor: a convenient method for preparing luminescent, surfactant-stabilized silicon nanoparticles.* Nanotechnology 2005. 16: p. 732-736.

[38] Canham, L.T., *Silicon quantum wire array fabrication by electrochemical and chemical dissolution of wafers*. Applied Physics Letters 1990. 57: p. 1046.

[39] Parak, W.J., L. Manna, F.C. Simmel, D. Gerion, and P. Alivisatos, *Nanoparticles - From Theory to Application. Ch1: Quantum Dots*, ed. G. Schmid. 2005: Wiley-VCH.

[40] Terekhov, V.A., V.M. Kashkarov, S.Y. Turishchev, K.N. Pankov, V.A. Volodin, M.D. Efremov, D.V. Marin, A.G. Cherkov, S.V. Goryainov, A.I. Korchagin, V.V. Cherepkov, A.V. Lavrukhin, S.N. Fadeev, R.A. Salimov, and S.P. Bardakhanov, *Structure and optical properties of silicon nanopowders.* Materials Science and Engineering: B, 2008. 147(2-3): p. 222-225.

[41] Klimov, V.I., *Semiconductor and Metal Nanocrystals - Synthesis and Electronic and Optical Properties*. 2004: Marcel Dekker, Inc.

[42] Hosokawa, M., K. Nogi, M. Naito, and T. Yokayama, *Nanoparticle technology handbook*. 2007: Elsevier B.V.

[43] Voz, C., D. Peiro, J. Bertomeu, D. Soler, M. Fonrodona, and J. Andreu, *Optimisation of doped microcrystalline silicon films deposited at very low temperatures by hot-wire CVD.* Materials Science and Engineering B, 2000. 69-70: p. 278-283.

[44] Seraphin, A.A., E. Werwa, and K.D. Kolenbrander, *Influence of nanostructure size on the luminescence behavior of silicon nanoparticle thin films.* Journal of Materials Research, 1997. 12(12): p. 3386-3392.

[45] Balberg, I., E. Savir, and J. Jedrzejewski, *The mutual exclusion of luminescence and transport in nanocrystalline silicon networks.* Journal of Non-Crystalline Solids, 2004. 338-340: p. 102-105.

[46] Chen, H.S., J.J. Chiu, and T.P. Perng, *On the photoluminescence of Si nanoparticles.* Mater.Phys.Mech, 2001. 4: p. 62-66.

[47] Zhu, X.P., T. Yukawa, M. Hirai, T. Suzuki, H. Suematsu, W. Jiang, and K. Yatsui, *Defect-related photoluminescence of silicon nanoparticles produced by pulsed ion-beam ablation in vacuum.* Applied Surface Science, 2005. 242(3-4): p. 256-260.

[48] Trave, E., V. Bello, F. Enrichi, G. Mattei, E. Borsella, M. Carpanese, M. Falconieri, C. Abate, N. Herlin-Boime, and K. Jursiokova, *Towards controllable optical properties of silicon based nanoparticles for applications in opto-electronics.* Optical Materials, 2005. 27(5): p. 1014-1019.

[49] Kanemitsu, Y., *Excitons in silicon quantum structures.* Journal of Luminescence, 1999. 83-84: p. 283-290.

[50] Colder, A., F. Huisken, E. Trave, G. Ledoux, O. Guillios, C. Reynaud, H. Hofmeister, and E. Pippel, *Strong visible photoluminescence from hollow silica nanoparticles.* Nanotechnology, 2004. 15: p. L1-L4.

[51] Delerue, C., M. Lannoo, G. Allan, and E. Martin, *Theoretical descriptions of porous silicon.* Thin Solid Films, 1995. 255(1-2): p. 27-34.

[52] Kanemitsu, Y., *Light emission from porous silicon and related materials.* Physics Reports, 1995. 263(1): p. 1-91.

[53] Lam, C., Y.F. Zhang, Y.H. Tang, C.S. Lee, I. Bello, and S.T. Lee, *Large-scale synthesis of ultra fine Si nanoparticles by ball milling.* Journal of Crystal Growth, 2000. 220: p. 466.

[54] Araujo-Andrade, C., F.J. Espinoza-Beltran, S. Jimenez-Sandoval, and J. Gonzalez-Hern, *Synthesis of nanocrystalline Si particles from a solid-state reaction during a ball-milling process.* Scripta Materialia, 2003. 49: p. 773.

[55] Tabrizi, N., M. Ullmann, V. Vons, U. Lafont, and A. Schmidt-Ott, *Generation of nanoparticles by spark discharge.* Journal of Nanoparticle Research, 2008.

[56] Zhu, Y., H. Wang, and P.P. Ong, *Preparation and thermal stability of silicon nanoparticles.* Applied Surface Science, 2001. 171: p. 44.

[57] Wu, M.H., R. Mu, A. Ueda, and D.O. Henderson, *Micro Raman Spectroscopy of Silicon Nano-crystals produced by Pico-second Pulsed Laser Ablation.* Material Research Society Symposium Proceedings, 2003. 738.

[58] Wu, M.H., R. Mu, A. Ueda, D.O. Henderson, and B. Vlahovic, *Production of silicon quantum dots for photovoltaic applications by picosecond pulsed laser ablation.* Materials Science and Engineering B, 2005. 116(3): p. 273-277.

[59] Makino, T., M. Inada, K. Yoshida, I. Umezu, and A. Sugimura, *Structural and optical properties of silicon nanoparticles prepared by pulsed laser ablation in hydrogen background gas.* Applied Physics A: Materials Science and Processing, 2004. 79(4): p. 1391-1393.

[60] Leconte, Y., P. Marie, X. Portier, M. Lejeune, and R. Rizk, *Combined growth of Si nanoparticles and crystallized silicon layers at 200deg C by reactive magnetron sputtering.* Materials Science and Engineering, 2003. B101: p. 194.

[61] Nayfeh, M.H., J. Therrien, and Z.H. Mani, *Silicon nanoparticle and method for producing the same*. 2001, United States Patent Application.

[62] von Behren, J., T. van Buuren, M. Zacharias, E.H. Chimowitz, and P.M. Fauchet, *Quantum confinement in nanoscale silicon: The correlation of size with bandgap and luminescence.* Solid State Communications, 1998. 105(5): p. 317-322.

[63] Tanaka, A., R. Saito, T. Kamikake, M. Imamura, and H. Yasuda, *Optical and photoelectron spectroscopic studies of alkyl-passivated silicon nanoparticles.* The European Physical Journal D - Atomic, Molecular, Optical and Plasma Physics, 2007. 43(1): p. 229-232.

[64] Pierson, H.O., *Handbook of Chemical Vapor Deposition*. 1999: William Andrew Publishing.

[65] Roca i Cabarrocas, P., *Plasma enhanced chemical vapor deposition of amorphous, polymorphous and microcrystalline silicon films.* Journal of Non-Crystalline Solids, 2000. 266-269(Part 1): p. 31-37.

[66] Roca i Cabarrocas, P., S. Hamma, S.N. Sharma, G. Viera, E. Bertran, and J. Costa, *Nanoparticle formation in low-pressure silane plasmas: bridging the gap between a-Si:H and mc-Si films.* Journal of Non-Crystalline Solids, 1998: p. 871.

[67] Schropp, R.E.I., *Advances in solar cells made with hot wire chemical vapor deposition (HWCVD): superior films and devices at low equipment cost.* Thin Solid Films, 2002. 403-404: p. 17-25.

[68] Schropp, R.E.I., B. Stannowski, A.M. Brockhoff, P.A.T.T. Van Veenendaal, and J.B. Rath, *Hot wire CVD heterogeneous and polychrystalline silicon semiconductor thin films for applications in thin film transistors and solar cells.* Mater.Phys.Mech, 2000: p. 73.

[69] Saleh, R., N.H. Nickel, and K.V. Maydell, *Laser crystallization of compensated hydrogenated amorphous silicon thin films.* Journal of Non-Crystalline Solids, 2006. 352(9-20): p. 1003-1007.

[70] Matsumura, H., H. Umemoto, and A. Masuda, *Cat-CVD (hot-wire CVD): how different from PECVD in preparing amorphous silicon.* Journal of Non-Crystalline Solids, 2004. 338-340: p. 19-26.

[71] Lau, K.K.S., H.G. Pryce Lewis, S.J. Limb, M.C. Kwan, and K.K. Gleason, *Hot-wire chemical vapor deposition (HWCVD) of fluorocarbon and organosilicon thin films.* Thin Solid Films, 2001. 395(1-2): p. 288-291.

[72] Lau, K.K.S., Y. Mao, H.G. Pryce Lewis, S.K. Murthy, B.D. Olsen, L.S. Loo, and K.K. Gleason, *Polymeric nanocoatings by hot-wire chemical vapor deposition (HWCVD).* Thin Solid Films, 2006. 501(1-2): p. 211-215.

[73] Hwang, N.M., W.S. Cheong, D.Y. Yoon, and D.-Y. Kim, *Growth of silicon nanowires by chemical vapor deposition: approach by charged cluster model.* Journal of Crystal Growth, 2000. 218: p. 33.

[74] Bunshah, R.F., *Handbook of Deposition Technologies for Films and Coatings: Science, Technology and Applications.* 1994: Noyes Publications.

[75] Niu, J.J., J.N. Wang, and Y.X. Chen, *Boron-doped silicon nano-wires.* Materials Science and Engineering: B, 2007. 139(1): p. 95-98.

[76] Ledoux, G., D. Amans, J. Gong, F. Huisken, F. Cichos, and J. Martin, *Nanostructured films composed of silicon nanocrystals.* Materials Science and Engineering, 2002. 19: p. 215.

[77] Martin, J., F. Cichos, and C. Von Borczyskowski, *Spectroscopy of single silicon nanoparticles.* Journal of Luminescence, 2004. 108: p. 347.

[78] Giorgi, R., S. Turth, G. Zappa, E. Borsella, S. Botti, M.C. Cesile, and S. Martelli, *Microstructural properties of laser synthesized Si/C/N nanoparticles.* Applied Surface Science, 1996. 93: p. 101.

[79] Trave, E., V. Bello, G. Mattei, M. Mattiazzi, E. Borsella, M. Carpanese, F. Fabbri, M. Falconieri, R. D'Amato, and N. Herlin-Boime, *Surface control of optical properties in silicon nanocrystals produced by laser pyrolysis.* Applied Surface Science, 2006. 252(13): p. 4467-4471.

[80] Najera, J.J., J.O. Caceres, J.C. Ferrero, and S.I. Lane, *Production of silicon containing particles by laser induced reaction of silane with methane, ethane and acetylene.* Journal of the European Ceramic Society, 2002. 22: p. 2371.

[81] Meier, C., A. Gondorf, S. Lüttjohann, and A. Lorke, *Silicon nanoparticles: Absorption, emission, and the nature of the electronic bandgap.* Journal of Applied Physics, 2007. 101: p. 103-112.

[82] Meier, C., S. Luttjohanna, V.G. Kravetsa, A. Nienhaus, H. Lorkea, H. Wiggers, C.-K. Choo, T. Sakamoto, M. Tohara, K. Tanaka, R. Nakata, and N. Okuyama, *Raman properties of silicon nanoparticles preparation and evaluation of nitrogen-terminated silicon nanoparticles: laser annealing effect.* Physica E, 2006. 32: p. 155.

[83] Knipping, J., H. Wiggers, B. Rellinghaus, P. Roth, D. Konjhodzic, and C. Meier, *Synthesis of High Purity Silicon Nanoparticles in a Low Pressure Microwave Reactor.* Journal of Nanoscience and Nanotechnology, 2004. 4(8): p. 1039.

[84] Gutsch, A., M. Krämer, G. Michael, H. Mühlenweg, M. Pridöhl, and G. Zimmermann, *Gas-Phase Production of Nanoparticles.* KONA, 2002. 20.

[85] Hofmeister, H., P. Kodderitzsch, and J. Dutta, *Structure of nanometersized silicon particles prepared by various gas phase processes.* Journal of Non-Crystalline Solids, 1998. 232-234: p. 182-187.

[86] Singhal, G., A. Wang, N. Glumac, B.H. Kear, and R.D. Hunt, *On nanoparticle aggregation during vapor phase synthesis.* Nanostructured Materials, 1999. 11 No. 4: p. 545.

[87] Martins, R., I. Ferreira, B. Fernandes, and E. Fortunato, *Performances of a-Si:H films produced by hot wire plasma assisted technique.* Vacuum, 1999. 52(1-2): p. 203-207.

[88] Ferreira, I., A. Cabrita, F. Braz Fernandes, E. Fortunato, and R. Martins, *Morphology and structure of nanocrystalline p-doped silicon films produced by hot wire technique.* Vacuum, 2002. 64(3-4): p. 237-243.

[89] Rees, W.S., *CVD of Nonmetals*. 1996: VCH Verlagsgesellschaft mbH.

[90] Jones, A.C. and M.L. Hitchman, *Chemical Vapour Deposition: Precursors, Processes and Applications.* 2009: RSC Publishing.

[91] Baletto, F. and R. Ferrando, *Structural properties of nanoclusters: Energetic, thermodynamic, and kinetic effects.* Reviews of Modern Physics, 2005. 77(1): p. 371-423.

[92] Sublemontier, O., F. Lacour, Y. Leconte, N. Herlin-Boime, and C. Reynaud, *CO2 laser-driven pyrolysis synthesis of silicon nanocrystals and applications.* Journal of Alloys and Compounds, 2008. In Press, Corrected Proof.

[93] Vach, H., Q. Brulin, N. Chaabane, T. Novikova, P. Roca i Cabarrocas, B. Kalache, K. Hassouni, S. Botti, and L. Reining, *Growth dynamics of hydrogenated silicon nanoparticles under realistic conditions of a plasma reactor.* Computational Materials Science, 2006. 35: p. 216.

[94] Chaabane, N., A. Kharchenko, H. Vach, and P.R. Cabarrocas, *Optimization of plasma parameters for the production of silicon nano-crystals.* New Journal of Physics, 2003: p. 37.

[95] Hofmeister, H., J. Dutta, and H. Hofmann, *Atomic structure of amorphous nanosized silicon powders upon thermal treatment.* Physical Review B, 1996. 54 Number 4.

[96] Dutta, J., H. Hofmann, C. Hollenstein, and H. Hofmeister, *Nanoparticles and Nanostructured Films. Ch8: Plasma-Produced Silicon Nanoparticle Growth and Crystallisation Process.* , ed. J.H. Fendler. 1998: Wiley-VCH.

[97] Lechner, R., A.R. Stegner, R.N. Pereira, R. Dietmueller, M.S. Brandt, A. Ebbers, M. Trocha, H. Wiggers, and M. Stutzmann, *Electronic properties of doped silicon nanocrystal films.* Journal of Applied Physics, 2008. 104(5): p. 053701-7.

[98] Saleh, R., N.H. Nickel, and K.V. Maydell, *Influence of laser annealing on hydrogen bonding in compensated polycrystalline silicon thin films.* Thin Solid Films, 2005. 487(1-2): p. 89-92.

[99] Filonovich, S.A., M. Ribeiro, A.G. Rolo, and P. Alpuim, *Phosphorous and boron doping of nc-Si:H thin films deposited on plastic substrates at 150 °C by Hot-Wire Chemical Vapor Deposition.* Thin Solid Films, 2008. 516(5): p. 576-579.

[100] Wiesmann, H., A.K. Gosh, T. McMahon, and M. Strongin, Journal of Applied Physics, 1979. 50(5): p. 3752.

[101] Mahan, A.H., *Hot wire chemical vapor deposition of Si containing materials for solar cells.* Solar Energy Materials and Solar Cells, 2003. 78(1-4): p. 299-327.

[102] Matsumura, M. and M. Tachibana, Applied Physics Letters, 1985. 47: p. 833.

[103] Matsumura, M., Japan Journal of Applied Physics, 1986. 25: p. 949.

[104] Doyle, J., R. Robertson, G.H. Lin, M.Z. He, and A. Gallagher, *Journal of Applied Physics.* 1988. 64: p. 3215.

[105] Mahan, A.H., J. Carapella, B.P. Nelson, R.S. Crandall, and I. Balberg, Journal of Applied Physics, 1991. 69: p. 6728.

[106] Wang, Q., *Combinatorial approach to studying tungsten filament ageing in fabricating hydrogenated amorphous silicon using the hot-wire chemical vapour deposition technique.* Meas. Sci. Technol., 2005. 16: p. 162.

[107] Doyle, J., R. Robertson, G.H. Lin, M.Z. He, and A. Gallagher, *Production of high-quality amorphous silicon films by evaporative silane surface decompositions.* Journal of Applied Physics, 1988. 64: p. 3215.

[108] Nakamura, S. and M. Koshi, *Elementary processes in silicon hot wire CVD.* Thin Solid Films, 2006. 501: p. 26.

[109] Matsumura, H. and K. Ohdaira, *New application of Cat-CVD technology and recent status of industrial implementation.* Thin Solid Films, 2009. 517(12): p. 3420-3423.

[110] Nakamura, S., A. Matsugi, A. Susa, and M. Koshi, *UV-visible absorption spectra of silicon CVD intermediates.* Thin Solid Films, 2008. 516(5): p. 517-520.

[111] Holt, J.K., M. Swiatek, D.G. Goodwin, R.P. Muller, W.A. Goddard, and H.A. Atwater, *Gas phase and surface kinetic processes in polycrystalline silicon hot-wire chemical vapour deposition.* Thin Solid Films, 2001. 395: p. 29.

[112] Kremer, D.M., R.W. Davisb, E.F. Mooreb, and S.H. Ehrman, *A numerical investigation of the effects of gas-phase particle formation on silicon film deposition from silane.* Journal of Crystal Growth, 2003. 247: p. 333.

[113] Duan, H.L., G.A. Zaharias, and S.F. Bent, *The effect of filament temperature on the gaseous radicals in the hot wire decomposition of silane.* Thin Solid Films, 2001. 395(1-2): p. 36-41.

[114] Moutinho, H.R., C.S. Jiang, Y. Xu, and B. To, *Mechanisms of Growth of Nanocrystalline Silicon Deposited by Hot-Wire Chemical Vapor Deposition.* NREL/CP-520-37345 Document, 2005.

[115] Peiro´, D., J. Bertomeu, C. Voz, M. Fonrodona, D. Soler, and J. Andreu, *Structure of microcrystalline silicon films deposited at very low temperatures by hot-wire CVD.* Materials Science and Engineering, 2000. B69–70: p. 536.

[116] Härting, M., D.T. Britton, R. Bucher, E. Minani, A. Hempel, M. Hempel, T.P. Ntsoane, C. Arendse, and D. Knoesen, *Influence of growth temperature on the microcrystallinity*

and native defect structure of hydrogenated amorphous silicon. Journal of Non-Crystalline Solids, 2002. 299–302: p. 103.

[117] Ring, D. and S.L. Miller, *The spark discharge synthesis of amino acids from various hydrocarbons.* Origins of Life and Evolution of Biospheres, 1984. 15(1): p. 7-15.

[118] Hill, R.D., *An efficient lightning energy source on the early earth.* Origins of Life and Evolution of Biospheres, 1992. 22(5): p. 277-285.

[119] Hnatiuc, B., E. Hnatiuc, S. Pellerin, and J. Chapelle, *Experimental analysis of a double-spark ignition system.* Czechoslovak Journal of Physics, 2006. 56(8): p. 851-867.

[120] Reinmann, R. and M. Akram, *Temporal investigation of a fast spark discharge in chemical inert gases.* Journal of Physics D: Applied Physics, 1997. 30: p. 1125-1134.

[121] Ashurly, Z.I., V.V. Gal, and V.P. Malin, *Temperature field in a pulsed discharge.* Journal of Engineering Physics and Thermophysics, 1971. 20(1): p. 45-49.

[122] Ono, R., M. Nifuku, S. Fujiwara, and S. Horiguchi, *Gas temperature of capacitance spark discharge in air.* Journal of Applied Physics, 2005. 97.

[123] Ono, R., M. Nifuku, S. Fujiwara, S. Horiguchi, and T. Oda, *Minimum ignition energy of hydrogen-air mixture: Effects of humidity and spark duration.* Journal of Electrostatics, 2007. 65(2): p. 87-93.

[124] Sauers, I., *By-product formation in spark breakdown of SF6/O2 mixtures.* Plasma Chemistry and Plasma Processing, 1988. 8(2): p. 247-262.

[125] Hoffman, D.M., J.H. Thomas, and B. Singh, *Handbook of Vacuum Science and Technology.* 1997: Elsevier Science & Technology Books.

[126] Atwater, H.A., *Low-Temperature, High-Throughput Process for Thin, Large-Grained Poly Si.* Final Technical Report, 2003. NREL/SR-520-34816.

[127] Zeiler, E., S. Schwarz, S.M. Rosiwal, and R.F. Singer, *Structural changes of tungsten heating filaments during CVD of diamond.* Materials Science and Engineering A, 2002. 335(1-2): p. 236-245.

[128] Honda, K., K. Ohdaira, and H. Matsumura, *A novel method for suppressing silicidation of tungsten catalyzer during silane decomposition in Cat-CVD.* Journal of Non-Crystalline Solids, 2008. 354(19-25): p. 2117-2120.

[129] van der Werf, C.H.M., P.A.T.T. van Veenendaal, M.K. van Veen, A.J. Hardeman, M.Y.S. Rusche, J.K. Rath, and R.E.I. Schropp, *The influence of the filament temperature on the structure of hot-wire deposited silicon.* Thin Solid Films, 2003. 430(1-2): p. 46-49.

[130] Schwab, A.J., *High Voltage Measurement Techniques.* 1972: M.I.T. Press.

[131] Kuffel, E. and W.S. Zaengl, *High Voltage Engineering Fundamentals.* 1984: Pergamon Press.

[132] Bossel, C., J. Dutta, R. Houriet, J. Hilborn, and H. Hofmann, *Processing of nano-scaled silicon powders to prepare slip cast structural ceramics.* Materials Science and Engineering A, 1995. 204(1-2): p. 107-112.

[133] Masuda, H., K. Higashitani, and H. Yoshida, *Powder Technology Handbook*. Third ed. 2006: Taylor & Francis.

[134] Williams, D.B. and C.B. Carter, *Transmission Electron Microscopy*. 1996: Plenum Publishing Corporation.

[135] Ghosh, J., S. Mazumdar, M. Das, S. Ghatak, and A.K. Basu, *Microstructural characterization of amorphous and nanocrystalline boron nitride prepared by high-energy ball milling.* Materials Research Bulletin, 2008. 43(4): p. 1023-1031.

[136] Brundle, C.R., C.A. Evans, and S. Wilson, *Encyclopedia of Materials Characterization*. Materials Characterization Series. 1992: Wiley-VCH.

[137] Goodhew, P.J., J. Humphreys, and R. Beanland, *Electron Microscopy and Analysis*. Third ed. 2001: Taylor & Francis.

[138] Champness, P.E., G. Cliff, and G.W. Lorimer, *Quantitative analytical electron microscopy of metals and minerals.* Ultramicroscopy, 1982. 8(1-2): p. 121-131.

[139] Ford, A.C., T. Tepper, and C.A. Ross, *Reactive pulsed laser deposition of silica and doped silica thin films.* Thin Solid Films, 2003. 437(1-2): p. 211-216.

[140] Alford, T., L.C. Feldman, and J.W. Mayer, *Fundamentals of Nanoscale Film Analysis*. 2007: Springer Science+Business Media, Inc.

[141] Berning, P. and R.E. Benenson, *Backscattering analysis for oxygen profiling using 16O(,)16O 3.05 MeV resonance parameters.* Nuclear Instruments and Methods in Physics Research, Section B: Beam Interactions with Materials and Atoms, 1989. B36(3): p. 335-339.

[142] Blanpain, B., P. Revesz, L.R. Doolittle, K.H. Purser, and J.W. Mayer, *Use of the 3.05 MeV oxygen resonance for 4He backscattering near-surface analysis of oxygen-containing high Z compounds.* Nuclear Instruments and Methods in Physics Research, Section B: Beam Interactions with Materials and Atoms, 1988. B34(4): p. 459-464.

[143] De, U., K.C. Verma, P. Karmakar, A. Sarkar, S. Dey, and S. Verma. *Resonance scattering and RBS from non-stoichiometric oxides*. 2003. India, India: Elsevier.

[144] Zhu, X.P., T. Yukawa, M. Hirai, H. Suematsu, W. Jiang, K. Yatsui, H. Nishiyama, and Y. Inoue, *X-ray photoelectron spectroscopy characterization of oxidated Si particles formed by pulsed ion-beam ablation.* Applied Surface Science, 2006. 252(16): p. 5776-5782.

[145] Castle, J.E., H. Chapman-Kpodo, A. Proctor, and A.M. Salvi, *Curve-fitting in XPS using extrinsic and intrinsic background structure.* Journal of Electron Spectroscopy and Related Phenomena, 2000. 106(1): p. 65-80.

[146] Castle, J.E. and A.M. Salvi, *Chemical state information from the near-peak region of the X-ray photoelectron background.* Journal of Electron Spectroscopy and Related Phenomena, 2001. 114-116: p. 1103-1113.

[147] Végh, J., *The Shirley background revised.* Journal of Electron Spectroscopy and Related Phenomena, 2006. 151(3): p. 159-164.

[148] Salvi, A.M. and J.E. Castle, *The intrinsic asymmetry component of the "total background" in XP spectra.* Journal of Electron Spectroscopy and Related Phenomena, 1998. 94(1-2): p. 73-87.

[149] White, W.B., *Raman Spectroscopy*, in *Encyclopedia of Materials Characterization*, C.R. Brundle, C.A. Evans, and S. Wilson, Editors. 1992, Wiley-VCH.

[150] Faraci, G., S. Gibilisco, P. Russo, A.R. Pennisi, G. Compagnini, S. Battiato, R. Puglisi, and S. La Rosa, *Si/SiO2 core shell clusters probed by Raman spectroscopy.* The European Physical Journal B - Condensed Matter and Complex Systems, 2005. 46(4): p. 457-461.

[151] Mishra, P. and K.P. Jain, *Raman, photoluminescence and optical absorption studies on nanocrystalline silicon.* Materials Science and Engineering B, 2002. 95(3): p. 202-213.

[152] Liu, F.M., B. Ren, J.H. Wu, J.W. Yan, X.F. Xue, B.W. Mao, and Z.Q. Tian, *Enhanced-Raman scattering from silicon nanoparticle substrates.* Chemical Physics Letters, 2003. 2: p. 502.

[153] Saleh, R. and N.H. Nickel, *Raman spectroscopy of B-doped microcrystalline silicon films.* Thin Solid Films, 2003. 427(1-2): p. 266-269.

[154] Rinnert, H., M. Vergnat, and G. Marchal, *Structure and optical properties of amorphous SiOx thin films prepared by co-evaporation of Si and SiO.* Materials Science and Engineering B, 2000. 69-70: p. 484-488.

[155] Chen, X.Y., Y.F. Lu, Y.H. Wu, B.J. Cho, L.J. Tang, D. Lu, and J.R. Dong, *Correlation between optical properties and Si nanocrystal formation of Si-rich Si oxide films prepared by plasma-enhanced chemical vapor deposition.* Applied Surface Science, 2006. 253(5): p. 2718-2726.

[156] Gullanar, M.H., Y.H. Zhang, H. Chen, W.S. Wei, G.Y. Xu, T.M. Wang, R.Q. Cui, and W.Z. Shen, *Effect of phosphorus doping on the structural properties in nc-Si:H thin films.* Journal of Crystal Growth, 2003. 256(3-4): p. 254-260.

[157] Jana, T. and S. Ray, *Microcrystalline silicon phase in silicon oxide thin films developed by photo-CVD technique.* Thin Solid Films, 2000. 376(1-2): p. 241-248.

[158] Zeng, X.B., X.B. Liao, B. Wang, S.T. Dai, Y.Y. Xu, X.B. Xiang, Z.H. Hu, H.W. Diao, and G.L. Kong, *Optical properties of boron-doped Si nanowires.* Journal of Crystal Growth, 2004. 265(1-2): p. 94-98.

[159] Campbell, I.H. and P.M. Fauchet, *The effects of microcrystal size and shape on the one phonon Raman spectra of crystalline semiconductors.* Solid State Communications, 1986. 58: p. 739-741.

[160] Chen, C.Y., S. Kimura, S. Sen, S. Nozaki, H. Ono, K. Uchida, and H. Morisaki. *Position and Size-Controlled Photosynthesis of Silicon Nanocrystals in SiO_2 Films.* in *Emerging Technologies - Nanoelectronics, 2006 IEEE Conference on.* 2006.

[161] Nayfeh, M.H., E. Rogoshina, and L. Mitas, *CH 10: Silicon Nanoparticles: Next Generation of Ultrasensitive Fluorescent Markers.* Synthesis, Functionalization and Surface Treatment of NANOPARTICLES., ed. M.-I. Baraton. 2003: American Scientific Publishers.

[162] Nayfeh, M.H. and L. Mitas, *Nanosilicon Ch1: Silicon Nanoparticles: New Photonic and Electronic Materials at the Transition Between Solid and Molecule.* , ed. V. Kumar. 2007: Elsivier Ltd.

[163] Kirk, C.T., *Quantitative analysis of the effect of disorder-induced mode coupling on infrared adsorption in silica.* Phys. Rev. B, 1988. 38: p. 1255-1273.

[164] Braun, H., K.J. Euler, and P. Herger, *Electronic conductivity of lead dioxide powder: separation of core and surface resistance of the particles.* Journal of Applied Electrochemistry, 1980. 10(4): p. 441-448.

[165] Sánchez-González, J., A. Macías-García, M.F. Alexandre-Franco, and V. Gómez-Serrano, *Electrical conductivity of carbon blacks under compression.* Carbon, 2005. 43(4): p. 741-747.

[166] Mamunya, Y.P., H. Zois, L. Apekis, and E.V. Lebedev, *Influence of pressure on the electrical conductivity of metal powders used as fillers in polymer composites.* Powder Technology, 2004. 140(1-2): p. 49-55.

[167] Celzard, A., J.F. Marêché, F. Payot, and G. Furdin, *Electrical conductivity of carbonaceous powders.* Carbon, 2002. 40(15): p. 2801-2815.

[168] Onaka, S., *Geometrical analysis of near polyhedral shapes with round edges in small crystalline particles or precipitates.* Journal of Materials Science, 2008. 43(8): p. 2680-2685.

[169] Ando, M., H. Miyamoto, H. Naito, and Y. Kanemitsu, *Photoelectric properties of printed thin films of silicon nanocrystals dispersed in polymer binder.* Journal of Non-Crystalline Solids, 2002. 299-302(Part 2): p. 1084-1089.

[170] Ferreira, I., A. Cabrita, F. Braz Fernandes, E. Fortunato, and R. Martins, *Role of the gas pressure and hydrogen dilution on the properties of large area nanocrystalline p-type silicon films produced by hot wire technique.* Materials Science and Engineering: C, 2001. 15(1-2): p. 141-144.

[171] Britton, D.T., A. Hempel, M. Härting, G. Kögel, P. Sperr, W. Triftshäuser, C. Arendse, and D. Knoesen, *Annealing and recrystallisation of hydrogenated amorphous silicon.* Phys. Rev. B: Condens. Matter Mater. Phys., 2001. B64.

[172] Patterson, A.L., *The Scherrer Formula for X-Ray Particle Size Determination.* Physical Review, 1939. 56(10): p. 978.

[173] Niwano, M., H. Katakura, Y. Takeda, Y. Takakuwa, N. Miyamoto, A. Hiraiwa, and K. Yagi, *Photoemission study of the SiO[sub 2]/Si interface structure of thin oxide films on Si(100), (111), and (110) surfaces.* Journal of Vacuum Science and Technology A: Vacuum, Surfaces, and Films, 1991. 9(2): p. 195-200.

[174] Härting, M., G. Goro Gonfa, E.A. Odo, M.R. Scriba, M.J. Van Staden, and D.T. Britton, *Sub-oxide passivation of silicon nanoparticles for use in printed electronics.* (Journal article in process), 2010.

[175] Hirose, K., H. Nohira, K. Azuma, and T. Hattori, *Photoelectron spectroscopy studies of SiO2/Si interfaces.* Progress in Surface Science, 2007. 82(1): p. 3-54.

[176] Hao, X.J., E.C. Cho, C. Flynn, Y.S. Shen, S.C. Park, G. Conibeer, and M.A. Green, *Synthesis and characterization of boron-doped Si quantum dots for all-Si quantum dot tandem solar cells.* Solar Energy Materials and Solar Cells, 2009. 93(2): p. 273-279.

[177] Sano, Y., W.B. Ying, Y. Kamiura, and Y. Mizokawa, *Annealing induced phosphorus protrusion into thin-oxide films from heavily phosphorus-doped silicon (100).* Thin Solid Films, 2008. 516(8): p. 1788-1795.

[178] Ying, W.B., Y. Mizokawa, K. Tanahashi, Y. Kamiura, M. Iida, K. Kawamoto, and W.Y. Yang, *Evaluation of the initial oxidation of heavily phosphorus doped silicon surfaces using angle-dependent X-ray photoelectron spectroscopy.* Thin Solid Films, 1999. 343-344: p. 393-396.

[179] Mizokawa, Y., W.B. Ying, Y.B. Yu, Y. Kamiura, M. Iida, and K. Kawamoto, *Phosphorus redistribution in the surface region of heavily phosphorus doped silicon.* Applied Surface Science, 1996. 100-101: p. 561-565.

[180] Kovalev, A.I., D.L. Wainstein, D.I. Tetelbaum, W. Hornig, and Y.N. Kucherehko, *Investigation of the electronic structure of the phosphorus-doped Si and SiO_2:Si quantum dots by XPS and HREELS methods.* Surface and Interface Analysis, 2004. 36(8): p. 959-962.

[181] Yoon, S.F. and R. Ji, *Application of electron cyclotron resonance chemical vapour deposition in the preparation of hydrogenated SiC films: a comparison of phosphorus and boron doping.* Journal of Alloys and Compounds, 1997. 261(1-2): p. 281-288.

[182] Hao, X.J., E.C. Cho, G. Scardera, E. Bellet-Amalric, D. Bellet, Y.S. Shen, S. Huang, Y.D. Huang, G. Conibeer, and M.A. Green, *Effects of phosphorus doping on structural and optical properties of silicon nanocrystals in a SiO2 matrix.* Thin Solid Films, 2009. 517(19): p. 5646-5652.

[183] Mishra, P. and K.P. Jain, *First- and second-order Raman scattering in nanocrystalline silicon.* Physical Review B, 2001. 64(7): p. 073304.

[184] Liang, Y., C.R. Miranda, and S. Scandolo, *Infrared and Raman spectra of silica polymorphs from an ab initio parametrized polarizable force field.* The Journal of Chemical Physics, 2006. 125(19): p. 194524-9.

[185] Meier, C., S. Lüttjohann, V.G. Kravets, H. Nienhaus, A. Lorke, and H. Wiggers, *Raman properties of silicon nanoparticles.* Physica E: Low-dimensional Systems and Nanostructures, 2006. 32(1-2): p. 155-158.

[186] Brühne, K., M.B. Schubert, C. Kohler, and J.H. Werner, *Nanocrystalline silicon from hot-wire deposition - a photovoltaic material?* Thin Solid Films, 2001. 395: p. 163.

[187] Mariotto, G., F. Ziglio, and F.L. Freire, *Light-emitting porous silicon: a structural investigation by high spatial resolution Raman spectroscopy.* Journal of Non-Crystalline Solids, 1995. 192-193: p. 253-257.

[188] Ovsyannikov, S.V., V.V. Shchennikov Jr, V.V. Shchennikov, Y.S. Ponosov, I.V. Antonova, and S.V. Smirnov, *Raman characterization of hydrogen ion implanted silicon: "High-dose effect"?* Physica B: Condensed Matter, 2008. 403(19-20): p. 3424-3428.

[189] Wei, W., G. Xu, J. Wang, and T. Wang, *Raman spectra of intrinsic and doped hydrogenated nanocrystalline silicon films.* Vacuum, 2007. 81(5): p. 656-662.

[190] Giustino, F. and A. Pasquarello, *Infrared properties of ultrathin oxides on Si(1 0 0).* Microelectronic Engineering, 2005. 80: p. 420-423.

[191] Dutta, J., I.M. Reaney, C. Bossel, R. Houriet, and H. Hofmann, *Crystallization of amorphous nano-sized silicon powders.* Nanostructured Materials, 1995. 6(1-4): p. 493-496.

[192] Koropecki, R.R., R.D. Arce, and J.A. Schmidt, *Infrared studies combined with hydrogen effusion experiments on nanostructured porous silicon.* Journal of Non-Crystalline Solids, 2004. 338-340: p. 159-162.

[193] San Andrés, E., A. del Prado, I. Mártil, G. González-Díaz, W. Bohne, J. Röhrich, B. Selle, I. Sieber, and M. Fernández, *Oxygen to silicon ratio determination of SiOxHy thin films.* Thin Solid Films, 2005. 492(1-2): p. 232-235.

[194] Hinds, B.J., F. Wang, D.M. Wolfe, C.L. Hinkle, and G. Lucovsky, *Investigation of postoxidation thermal treatments of Si/SiO2 interface in relationship to the kinetics of amorphous Si suboxide decomposition.* J.Vac.Sci.Technol., 1998. 16: p. 2171.

[195] Giustino, F. and A. Pasquarello, *Infrared Spectra at Surfaces and Interfaces from First Principles: Evolution of the Spectra across the Si(100)-SiO_2 Interface.* Physical Review Letters, 2005. 95(18): p. 187402.

[196] Liu, Q. and S.M. Kauzlarich, *A new synthetic route for the synthesis of hydrogen terminated silicon nanoparticles.* Materials Science and Engineering, 2002. 96: p. 72.

[197] Hirose, F., *Incorporation mechanism of dopant phosphorus in the Si growth using Si2H6 and PH3.* Journal of Crystal Growth, 2000. 212(1-2): p. 103-108.

[198] Cabrera, N. and N.F. Mott, *Theory of the Oxidisation of Metals.* Pep. Prog. Phys., 1948. 12(163).

[199] Montes, J.M., J.A. Rodriguez, and E.J. Herrera, *Thermal and electrical conductivities of sintered powder compacts.* Powder Metallurgy, 2003. 46(3): p. 251-256.

[200] Raether, F. and M. Iuga, *Effect of particle shape and arrangement on thermoelastic properties of porous ceramics.* Journal of the European Ceramic Society, 2006. 26(13): p. 2653-2667.

[201] Gerberich, W.W., W.M. Mook, C.R. Perrey, C.B. Carter, M.I. Baskes, R. Mukherjee, A. Gidwani, J. Heberlein, P.H. McMurry, and S.L. Girshick, *Superhard silicon nanospheres.* Journal of the Mechanics and Physics of Solids, 2003. 51(6): p. 979-992.

[202] Gerberich, W.W., W.M. Mook, M.J. Cordill, C.B. Carter, C.R. Perrey, J.V. Heberlein, and S.L. Girshick, *Reverse plasticity in single crystal silicon nanospheres.* International Journal of Plasticity, 2005. 21(12): p. 2391-2405.

[203] Perrey, C.R. and C.B. Carter, *Insights into nanoparticle formation mechanisms.* Journal of Materials Science, 2006. 41(9): p. 2711-2722.

[204] Borsella, E., M. Falconieri, S. Botti, S. Martelli, F. Bignoli, L. Costa, S. Grandi, L. Sangaletti, B. Allieri, and L. Depero, *Optical and morphological characterization of Si nanocrystals/silica composites prepared by sol-gel processing.* Materials Science and Engineering B, 2001. 79(1): p. 55-62.

[205] Giesen, B., H. Wiggers, A. Kowalik, and P. Roth*, *Formation of Si-nanoparticles in a microwave reactor: Comparison between experiments and modelling.* Journal of Nanoparticle Research, 2005. 7(1): p. 29-41.

[206] Miura, H., H. Ohta, N. Okamoto, and T. Kaga, *Crystallization-induced stress in silicon thin films.* Applied Physics Letters, 1992. 60(22): p. 2746-2748.

[207] Wang, Z.L., *Transmission Electron Microscopy and Spectroscopy of Nanoparticles.*, in *Characterization of Nanophase Materials.*, Z.L. Wang, Editor. 2001, Wiley WCH Verlag GmbH.

[208] Barnard, A.S. and P. Zapol, *A model for the phase stability of arbitrary nanoparticles as a function of size and shape.* The Journal of Chemical Physics, 2004. 121(9): p. 4276-4283.

[209] Onaka, S., *A simple equation giving shapes between a circle and a regular N -sided polygon.* Philosophical Magazine Letters, 2005. 85(7): p. 359-365.

[210] Kimoto, K., *Morphology and crystal structure of fine particles produced by a gas evaporation technique.* Thin Solid Films, 1976. 32(2): p. 363-365.

[211] Wang, Z.L. and J.S. Yin, *Self-assembly of shape-controlled nanocrystals and their in-situ thermodynamic properties.* Materials Science and Engineering A, 2000. 286(1): p. 39-47.

[212] Mackenzie, J.K., A.J.W. Moore, and J.F. Nicholas, *Bonds broken at atomically flat crystal surfaces--I: Face-centred and body-centred cubic crystals.* Journal of Physics and Chemistry of Solids, 1962. 23(3): p. 185-196.

[213] Wang, Z.L., M.B. Mohamed, S. Link, and M.A. El-Sayed, *Crystallographic facets and shapes of gold nanorods of different aspect ratios.* Surface Science, 1999. 440(1-2): p. L809-L814.

Appendix A: Diagram of the complete HWTCP/SP system

(Designed and constructed for this research)

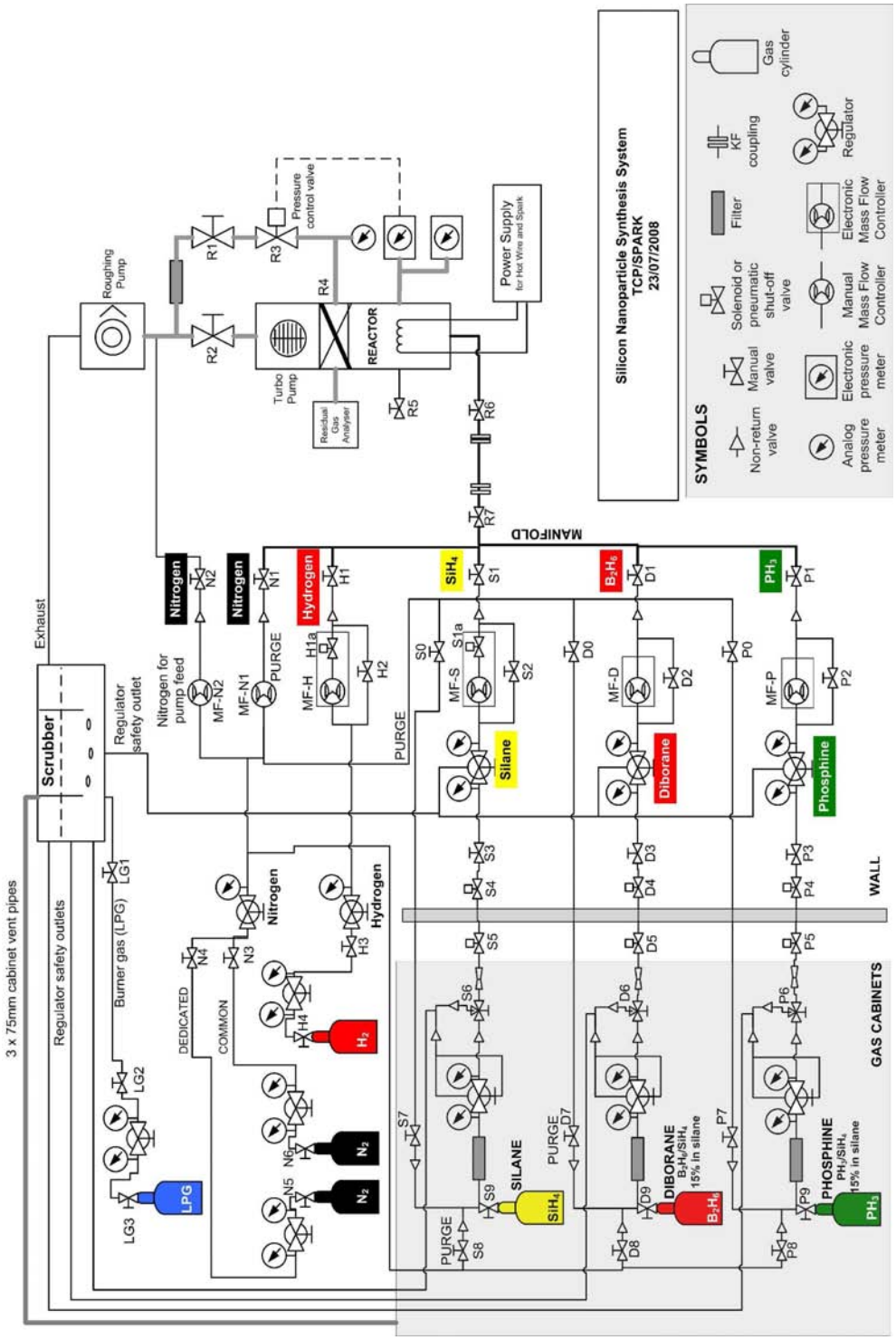

Appendix B: Link between nanoparticle shape and surface energy

The shape of a nanoparticle is primarily determined by two factors. The first is its crystal structure, which in silicon, is the face centred cubic (fcc) Bravais lattice and secondly by the total surface energy of the particle [168, 209-211]. The surface energy of the crystal planes of a nanoparticle may be determined by the atomistic approach known as the broken bond model, where the interaction between atoms on the surface area *A* of different lattice planes is considered for the calculation of the surface energy *γ*.

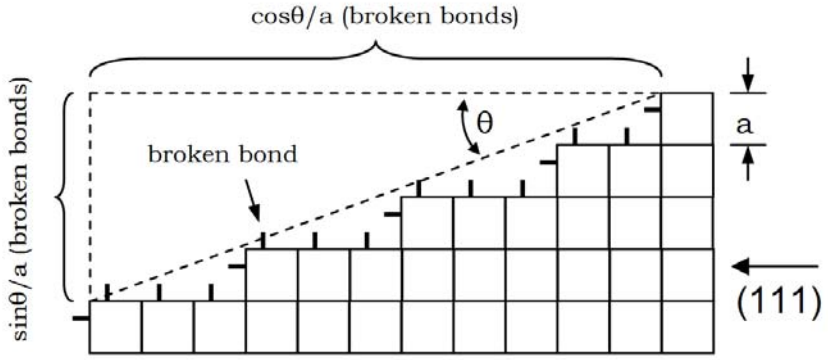

Figure 7.9 Schematic to explain the broken-bond model for the determination of surface energy of a nanoparticle. The nearest atom neighbour distances a, is shown.

The surface energy of any plane is thus:

$$E_{Surface} = \frac{(\cos|\theta| + \sin|\theta|)\varepsilon_b}{2a^2}, \qquad (7.3)$$

where a is the distance to the nearest bond and ε is the energy per bond.
For all planes the energy, as calculated, is lowest for the closest packed (111) plane and furthermore $\gamma_{(111)} < \gamma_{(100)} < \gamma_{(110)}$ [91].

Assuming favourable synthesis conditions, the broken bond model predicts nanoparticles to assume a shape which minimises the total surface energy:

$$\sum_{i=1}^{N} A_i \gamma_i = \min. \qquad (7.4)$$

However, the total surface energy of the nanoparticle is the sum of all surface areas,

$$\sum_{i=1}^{N} A_i\gamma_i = A_1\gamma_1 + A_2\gamma_2 + A_3\gamma_3 + ... \qquad (7.5)$$

In favourable conditions of pressure and temperature the particle will grow such that the minimum surface energy is maintained

$$dE = 0 = \sum_{i=1}^{N} \gamma_i dA. \qquad (7.6)$$

Using the nearest neighbour broken bond model [212], the surface energy of nanoparticles may be calculated and presented graphically [168], by defining two parameters; η is the degree of polyhedrality and α indicates the relative importance of the $\{111\}$ planes contribution to the surface energy of the particle, compared to that of a sphere with the same volume. Two graphs are of interest, figure 7.10 (a) shows the surface to volume ratio and figure 7.10 (b) the normalised surface energy for particles with equal volume.

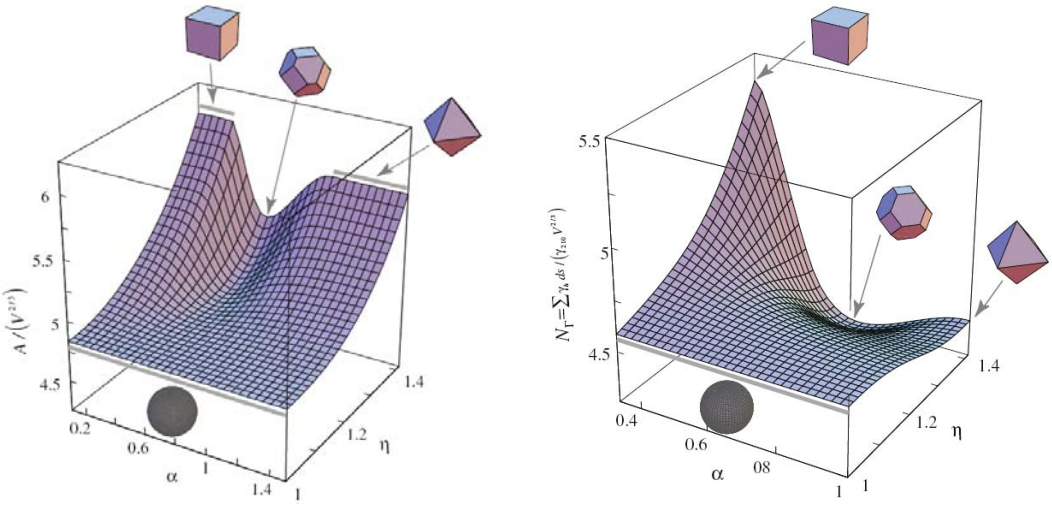

(a) (b)

Figure 7.10 Plots of (a) the surface to volume ratio ($A/V^{2/3}$) as well as (b) the normalised surface energy of particle shapes between a sphere and a cube, for the same volume. (from [168])

As shown in Figure 7.10 (a) by the dimensionless value of the normalised surface area $A/V^{2/3}$, for a constant volume V, the sphere has the best volume to surface ratio. However, as observed in figure 7.10 (b) by the dimensionless value of the normalised surface energy N_{Γ}, the shape with the lowest surface energy is not the sphere, but the truncated octahedron.

Thus , when a nanocrystal forms in materials with a fcc structure, under favourable conditions, as shown in figure 7.11, the low index planes $\{100\}$ an $\{110\}$ will grow first, resulting in polyhedral nanoparticles [168, 209-211].

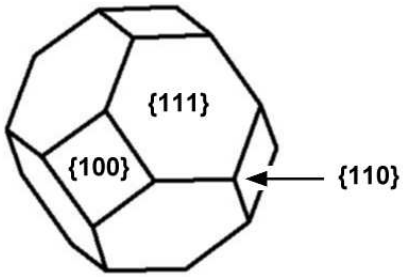

Figure 7.11 Truncated octahedral with the $\{100\}$ and $\{111\}$ planes shown.

Due to the higher surface energy of the $\{110\}$ planes, silicon nanoparticles with $\{110\}$ facets are relatively unstable and thus not often produced [213].

Appendix C: Photographs of the gas handling system

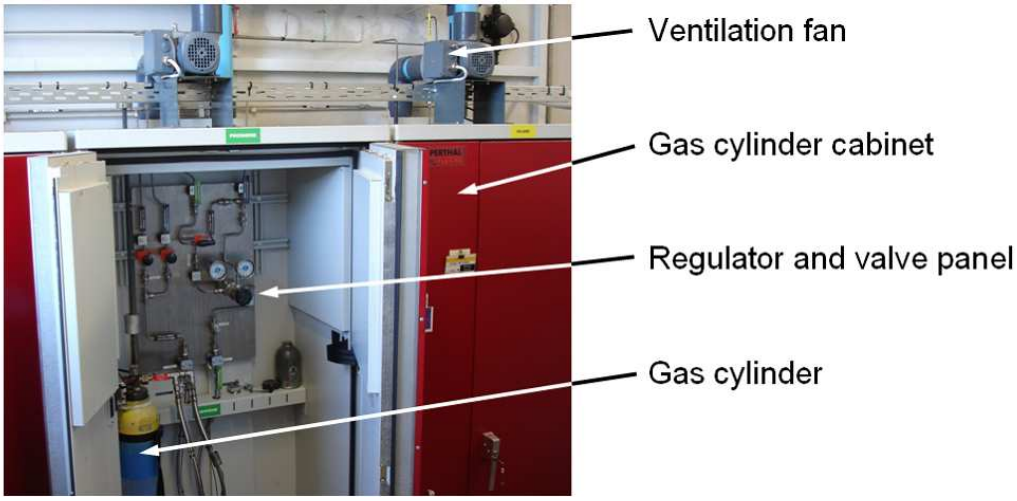

Figure C1 One of three fire proof gas cabinets used to safely store the silane, diborane and phosphine cylinders.

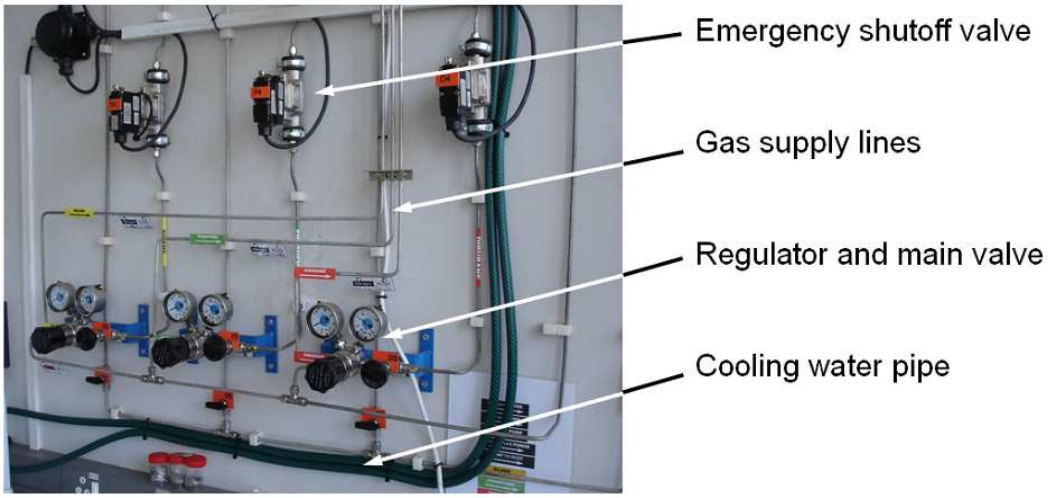

Figure C2 Gas supply system with regulators and emergency shutoff valves.